LOW GRADE WASTE HEAT RECOVERY ENHANCEMENT METHODS USING THERMOELECTRIC GENERATORS

Thesis submitted in partial fulfillment for the

Award of Degree

Doctor of Philosophy

By

Kartik Srivastava

DEPARTMENT OF MECHANICAL ENGINEERING INDIAN INSTITUTE OF TECHNOLOGY (BANARAS HINDU UNIVERSITY)
VARANASI - 221005

Roll No. 21131009

2025

CERTIFICATE

It is certified that the work contained in the thesis titled "**Low grade waste heat recovery enhancement methods using thermoelectric generators**" by **Kartik Srivastava** has been carried out under my supervision and that this work is not submitted elsewhere for any degree.

It is further certified that the student has satisfactorily fulfilled all the requirements of the Comprehensive examination, Candidacy, and SOTA for the award of the Ph.D. degree.

Dr. Rashmi Rekha Sahoo

(Supervisor)

Department of Mechanical Engineering

IIT(BHU) Varanasi

Associate Professor
Deptt. of Mechanical Engg
Indian Institute of Technology (BH
Varanasi-221005

DECLARATION BY THE CANDIDATE

I, **Kartik Srivastava,** certify that the work embodied in this thesis is my bonafide work carried out by me under the supervision of **Dr. Rashmi Rekha Sahoo** for a period of 3 years and 9 months from July 2021 to March 2025 at IIT(BHU) Varanasi. The material contained in this thesis has not been submitted for the award of any other degree. I declare that I have faithfully acknowledged and given credit to the research workers wherever their works have been cited in my work in this thesis. I further declare that I have not willfully copied any others' work, paragraphs, text, data, results, etc., reported in journals, books, magazines, reports, dissertations, theses, etc., or available on websites, and have not included them in this thesis and have not cited them as my work.

Kartik

Date: 23/04/2025 **(Kartik Srivastava)**

Place: IIT (BHU), Varanasi Candidate

CERTIFICATE BY THE SUPERVISORS

This is to certify that the above statement made by the candidate is correct to the best of my knowledge.

Dr. Rashmi Rekha Sahoo

(Supervisor)

Associate Professor
Deptt. of Mechanical Engg
Indian Institute of Technology (BHU)
Varanasi-221005

Pradyumna Ghosh. 1/9/25

Head of the Department

प्रद्युम्न घोष / HEAD
यांत्रिकी अभियान्त्रिकी विभाग / Deptt. of Mechanical Engg.
भारतीय प्रौद्योगिकी संस्थान / Indian Institute of Technology
(का.हि.वि.वि. / B.H.U.)
वाराणसी - 221005 / Varanasi - 221005

COPYRIGHT TRANSFER CERTIFICATE

Title of the Thesis: **Low grade waste heat recovery enhancement methods using thermoelectric generators**

Candidate's Name: **Kartik Srivastava**

Copyright Transfer

The undersigned hereby assigns to the Indian Institute of Technology (Banaras Hindu University) Varanasi, all rights under copyright that may exist in and for the above thesis submitted for the award of the Ph.D. degree.

Kartik

Date: 23/04/2025 **(Kartik Srivastava)**

Place: IIT (BHU), Varanasi

Note: However, the author may reproduce or authorize others to reproduce material extracted verbatim from the thesis or a derivative of the thesis for the author's personal use, provided that the source and the University's copyright notice are indicated.

ACKNOWLEDGEMENTS

I take this opportunity to express my deep sense of gratitude to my supervisor, **Dr. Rashmi Rekha Sahoo,** for her continuous guidance and whole-hearted cooperation in carrying out this work. Her meticulous and valuable review and constructive criticism of the manuscript have greatly improved the quality of the work. Ma'am, your faith in me and the desire to live up to your expectations have constantly pushed me to work harder.

My grateful appreciation also goes to **Prof. Pradyumna Ghosh** and **Prof. Sandip Ghosh** for serving on my research progress evaluation committee (RPEC). Thank you all for sparing your valuable time and assisting me throughout my research and the completion of this thesis. I wish to extend my sincere thanks to **Prof. Sandeep Kumar**, Head of the Department of Mechanical Engineering, for providing me with the necessary resources to enable me to complete this research work. During my stay at IIT (BHU) Varanasi, I have met many people who have made this period of my life memorable and very pleasant. Among them, I would like to sincerely acknowledge the assistance and motivation provided by Prof. S.K. Shukla, Prof. J. Sarkar, Prof. A. Sarkar, and Dr. S. S. Mondal. I want to thank my colleagues at IIT (BHU) Varanasi, especially Mr. Utkarsh Srivastava, Mr. Sunil Kumar Gaur, and Mr. Nilesh Krishnadhari Singh, for encouraging me to finish this work. The experimental part of this thesis has been carried out at the Department of Mechanical Engineering, IIT (BHU) Varanasi. Several people have assisted and supported me in designing and developing the test rig. I would like to extend my sincere thanks to Mr. Surender Yadav and Shivlal for giving valuable ideas while performing experiments and providing the measurement tools and instruments whenever needed for the research work without any hesitation.

I extend my deepest gratitude to my beloved parents for their unwavering support throughout my research journey. Their steadfast encouragement and understanding allowed me to remain completely focused on my work, free from any distractions. I am immensely grateful for their financial assistance whenever needed and for their constant motivation, which strengthened my resolve.

I wish to pay a special tribute to my parents, whose unwavering love and profound sacrifices have been the foundation of my journey. To my late mother, whose boundless love remains my eternal source of strength and guiding inspiration. And to my late father, for his unwavering faith in my potential, his steadfast support, and the countless sacrifices that enabled me to dedicate myself to this work. I am eternally grateful to you both; your belief in me is forever cherished in my heart.

Above all, I offer my profound gratitude to the Almighty God, whose blessings have granted me the strength, perseverance, and determination to stay committed to the path of success.

Date: 23/04/2025

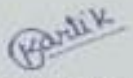

Place: IIT (BHU), Varanasi **(Kartik Srivastava)**

Dedicated
to
the loving memory
of
Maa & Papa

This page is left intentionally blank

Table of Contents

This page is left intentionally blank

List of Figures

This page is left intentionally blank

List of Tables

List of Symbols

Nomenclature

A	Area (m^2)
A, B	Viscosity enhancement coefficients
A_a	Outer surface area of the absorber (m^2)
A_e	Effective heat absorption area of the absorber (m^2)
Ar	Cross-sectional area of the computational domain (m^2)
A_t	Cross area of the tube (m^2)
Be	Bejan number
C	Conductivity enhancement coefficient
C_p	Specific heat capacity (J/kgK)
D	Distance between consecutive vortex generators (m)
D/H	Distance to height ratio
D_h	Hydraulic diameter (m)
ΔP	Pressure drop (Pa)
ΔT	Temperature difference (K)
D_h	Hydraulic diameter (m)
d_{SC}	Inner absorber tube's outer diameter (m)
d_{tube}	Outer diameter of the inner absorber tube (m)
Ex	Exergy rate (W)
f	Friction factor
F'	Collector efficiency factor
F_R	Heat removal factor
G	Incident solar radiation (W/m^2)

h	Heat transfer coefficient (W/m^2K)
H_c	Channel height (m)
$h_{f,I}$	Heat transfer coefficient at the fluid-tube wall interface (W/m^2K)
i	Control unit number
I	Current (A)
I_{rr}	Irreversibility rate (W)
k	Thermal conductivity (W/mK)
K	TEG power factor (W/K^2)
k_{Al}	Thermal conductivity of aluminum (W/mK)
k_{pn}	TEG thermal conductivity (W/mK)
L	Length (m)
L_{SC}	Inner absorber tube's effective length (m)
$\dot{m}$	Mass flow rate (kg/s)
n	Number of channels
N	TEG computational unit number
Nu	Nusselt number
$Power$	TEG power (W)
Pr	Prandtl number
$\dot{Q}$	Heat rate (W)
q_{flux}	Heat flux (W/m^2)
R	Thermal resistance ($m^2.K/W$)
R^2	Coefficient of determination
Re	Reynolds number
Req	Equivalent electrical resistance (Ω)

R_{pn}	TEG electrical resistance (Ω)
S/N	Signal-to-noise ratio
$\dot{S}_{gen}$	Entropy generation rate (W/K)
t	Heat sink base thickness (m)
t_p	Heat exchanger plate thickness (m)
T	Temperature (K)
U_f	Uncertainty
U_m	Mean velocity (m/s)
$\dot{V}$	Volume flow rate (m^3/s)
V	Voltage (V)
W	Width (m)
w_c	Channel width (m)
w_w	Wall width (m)
x	x-direction
x^*	Dimensionless thermal entry length
y	y-direction
z	z-direction
ZT	Figure of merit

Greek letters

α	Channel aspect ratio
α_a	Absorbing coating's absorptivity capacity
α_{pn}	Seebeck coefficient (V/K)
β	Width ratio of the fin to channel
η_{conv}	TEG conversion efficiency

η_{fin}	Fin efficiency
γ	Aspect ratio
μ	Dynamic viscosity (kg/ms)
φ	Volume fraction
ρ	Density (kg/m^3)
ρ_{pn}	TEG resistivity (m/S)
τ	Outer glass's light transmittance
Γ	Diffusion coefficient

Subscripts

0	Reference case
amb	Ambient
avg	Average
bf	Base fluid
c	Cold
ch	Channel
cap	Capacitive
co	Coolant
cond	Conductive
conv	Convective
ex	Exhaust
h	hot
hnf	Hybrid nanofluid
hs	Heat sink
in	Inlet

m	Intermediate
nf	Nanofluid
out	Outlet
w	Wall of the heat sink

Abbreviation

ANN	Artificial neural network
ANOVA	Analysis of variance
CFD	Computational fluid dynamics
DMSO	Dimethyl sulfoxide
DVG	Delta vortex generator
EG	Ethylene glycol
EUSWH	Evacuated u-tube solar water heater
FVG	Fishtail vortex generator
GHG	Greenhouse gas
HTC	Heat transfer coefficient
HTF	Heat transfer fluid
HX	Heat exchanger
LHSCS	Latent heat storage and cooling system
LVG	Longitudinal vortex generator

MVG	Envelope vortex generator
MVS TEG	Multistage variable shape TEG
MWCNT	Multi-wall carbon nano tube
ORC	Organic Rankine cycle
RTG	Radioisotope thermoelectric generator
RWVG	Rectangular winglet vortex generator
STEG	Solar thermoelectric generator
TEF	Thermal enhancement factor
TEG	Thermoelectric generator
TES	Thermal energy storage
VG	Vortex generator
WHR	Waste heat recovery

Abstract

Thermoelectric generators (TEGs) play a vital role in Waste Heat Recovery (WHR) by directly converting thermal energy into electrical energy through the Seebeck effect. When a temperature gradient is established across the thermoelectric material, charge carriers (electrons or holes) diffuse from the hot side to the cold side, generating an electric voltage. This solid-state energy conversion technology has advantages such as no moving parts, silent operation, and high durability, making it ideal for applications in automotive exhaust systems, industrial processes, and remote power generation. Despite their relatively low efficiency compared to other waste heat recovery technologies, TEGs offer unique benefits in scenarios where conventional methods are impractical. The performance of a TEG is significantly influenced by the temperature difference (ΔT) across its hot and cold sides. A higher temperature difference enhances the thermoelectric voltage and power output due to an increased Seebeck coefficient and thermal gradient. However, excessive temperature gradients can also introduce thermal stresses, leading to material degradation over time. The Seebeck coefficient generally depends on the material's properties and average temperature rather than the temperature difference itself. For most thermoelectric materials, the Seebeck coefficient decreases with increasing average temperature due to increased thermal carrier excitations, which reduce the charge carrier asymmetry. However, in some materials, it may initially increase with temperature before declining. The temperature difference across a thermoelectric generator affects the output voltage and power but doesn’t directly increase the Seebeck coefficient, as the coefficient is primarily a material-specific property tied to its electronic structure. Furthermore, the temperature distribution on the hot and cold sides plays a crucial role in maintaining uniform heat flux. Non-uniform heating can create hotspots, reducing the efficiency and longevity of the thermoelectric material. Effective heat spreading and

cooling mechanisms, such as heat sinks or phase-change materials, can help in maintaining a stable temperature distribution, thereby improving TEG performance. The configuration of a TEG, including its material composition, number of stages, and leg geometry, significantly affects its efficiency. The choice of thermoelectric material determines the conversion efficiency, as materials with high Figure-of-merit (ZT) values exhibit superior performance and organic materials improve the system sustainability. Multi-stage TEGs can be employed to optimize performance across a wide temperature range by using different materials in a cascaded manner. This approach ensures that each stage operates efficiently within its optimal temperature window. The geometry of the thermoelectric legs also plays a crucial role in determining heat transfer characteristics and electrical resistance. Optimizing the leg length and cross-sectional area can enhance the power density and efficiency of the module. Therefore, a balance must be achieved to maximize performance.

The current study discusses three ways to enhance the TEG performance, viz., hot side performance enhancement, TEG device improvement, and cold side performance enhancement. Enhancing heat transfer on the hot side of a TEG can be achieved by incorporating a vortex generator, which disrupts boundary layers and induces turbulence for improved convection. Optimizing TEG performance involves exploring high-ZT sustainable materials, multi-stage configurations, and refined leg geometries. Additionally, replacing conventional coolants with hybrid nanofluids on the cold side enhances thermal conductivity and cooling efficiency, boosting overall power output. These methods, along with optimization techniques and the development of a hybrid system, were examined for their thermohydraulic and electrical performance.

For TEG hot side performance enhancement, an experimental study has been carried out to investigate the influence of novel vortex generators (delta (DVG), envelope

(MVG), and fishtail (FVG)) on the performance of a heat exchanger integrated with a thermoelectric generator (TEG). The effects of the distance-to-height ratio (D/H) and the inclination angle (θ) of the vortex generator configurations on key thermohydraulic parameters— heat transfer coefficient (HTC), pressure drop, and thermal enhancement factor (TEF)—along with their impact on TEG performance metrics, namely power output, have been systematically analyzed. 1-D thermal resistance model analyses heat transport. Vortex generators create longitudinal vortices that enhance fluid mixing. This improves heat transfer by disrupting the boundary layer and bringing hotter fluid closer to the cooler surface. The maximum increment in heat transfer coefficients was 45.16%, 51.85%, and 56.18% for MVG, DVG, and FVG, respectively at D/H=2 and θ=60°. The highest pressure drops obtained are 3.46Pa, 3.72Pa, and 3.27Pa for MVG, DVG, and FVG, respectively at D/H=2 and θ=90°. The TEG output improved due to higher surface temperature in channels equipped with VGs than the smooth channel, owing to better heat transfer. The highest average TEG power obtained is 1.62W.

The focus is then drawn towards modeling a modified TEG based on stages, new sustainable thermoelectric material, and TEG leg geometry. A theoretical study has been carried out that analyses a multistage variable-shaped thermoelectric generator (MVS TEG) for a combination of dissimilar materials. Effect on voltage, power, conversion efficiency, normalized constraints (voltage, power, and conversion efficiency), and second law efficiency with a row number, exhaust inlet temperature, and coolant flow rate were investigated. Results revealed the row number as the most critical input parameter followed by exhaust inlet temperature and coolant flow rate. Also, the work gives optimum values of rows for voltage and power as N_x=19 for MVS TEG-1, MVS TEG-3, and MVS TEG-4 while N_x=18 for MVS TEG-2. The exhaust inlet temperature variation increases the voltage and power output by 54 to 59% and by 53 to 58%

respectively. The coolant flow variation has a greater impact on the conversion efficiency and the average improvement in the efficiency is about 9.23% in the present study. The second law efficiency decreases with the increase in all the input parameters.

For TEG cold side performance enhancement analysis, the effect of dissimilar-shaped nanoparticles (i.e., graphene-platelet shape, Al_2O_3-blade shape, MWCNT-cylindrical shape, and Fe_3O_4-brick shape), by 50:50 v/v., hybrid nanofluids in a mini channel heatsink (MCHS) with varying volume flow rate and vol. fraction (0.1% - 1%) have been discussed. Comparative thermal performance parameters (COP and figure of merit) and exergetic analysis (inlet and outlet exergy) have been investigated along with the heat transfer rates. The study is carried out with water as the reference fluid. The cylindrical-brick (MWCNT-Fe_3O_4) blend performs the best in terms of thermal properties, with 79.27% enhancement with volume flow rate variation and 1.03% enhancement with the volume concentration in the average heat transfer coefficient. The highest TEG power and conversion efficiency are 6.085W and 5.47% respectively. Cylindrical-brick (MWCNT-Fe_3O_4) hybrid nanofluid gives the best TEG performance.

A numerical study consisting of different geometries of vortex generators (VGs) under different ambient conditions has been studied to find the thermohydraulic effectiveness of the VGs in a rectangular channel and a comparative analysis has been carried out. The shapes of VG examined are delta (D), envelope (M), and fishtail (F). The ambient heat transfer coefficients (HTCs) applied are 5, 15, and 25W/m^2K. Various thermal and fluid flow parameters have been taken into consideration. Taguchi design-of-experiments is used to carry out the combinations of runs required for the analysis. The analysis of variance (ANOVA) and S/N ratios further helps in determining the optimum or the best factors for the outcome. Quantitatively, the heat transfer coefficient value at the outlet increases by 2.797, 2.777, and 2.834 times for DVG, MVG, and FVG

respectively as compared to the inlet for h=25W/m^{2}K. Similarly, for h=15W/m^{2}K, h raises by 2.801, 2.783, and 2.838 times at the outlet when compared to the parameter value at the inlet. For h=5W/m^{2}K, these values are 2.785, 2.766, and 2.566 for DVG, MVG, and FVG respectively. The pressure drops by 84.94%, 92.42%, 91.39%, and 89.44% for the smooth-, DVG-, MVG-, and FVG-incorporated channels. Furthermore, the highest value of signal-to-noise ratio is exhibited by the factors A3 (fishtail VG) and B1 (h=5W/m^{2}K) out of the 9 runs. The machine learning ANN model gives the coefficient of determination value (R^2) of 1, 0.99994, and 0.99962 indicating high proficiency of the neural network.

Additionally, an innovative hybrid system comprising an Evacuated U-tube Solar Water Heater (EUSWH) integrated with a TEG has been investigated. To enhance thermal and electrical performance, fishtail vortex generators (FVGs) are strategically implemented on the hot side of the TEG module. The study examines the influence of key operating parameters, including incident solar radiation intensity, water mass flow rate, inlet EUSWH temperature, and the incorporation of vortex generators, on various performance metrics of the EUSWH, TEG, and the overall hybrid system. The analysis reveals that the EUSWH achieves peak performance at the maximum solar irradiance (G). However, increasing the mass flow rate results in a reduction in the outlet water temperature ($T_{out,EUSWH}$), while enhancing the thermal energy output (Q_{EUSWH}) and thermal efficiency (η_{EUSWH}). Conversely, a rise in the inlet EUSWH temperature ($T_{in,EUSWH}$) increases $T_{out,EUSWH}$ but decreases Q_{EUSWH} and η_{EUSWH}. At G=1000W/m^2, η_{EUSWH} increases by 2.63% and 2.62% at mass flow rates of 0.01 and 0.02kg/s, respectively when the $T_{in,EUSWH}$ varies from 303-313K. However, it decreases by 0.45% and 0.46% at $T_{in,EUSWH}$ of 303 and 313K, respectively when mass flow rates are varied from 0.01-0.02kg/s. The hybrid system efficiency (η_{HS}) is enhanced with the application of FVGs on the hot side of the TEG. The hybrid system efficiency increases by 9.12%, and 9.38% for 0.01 and

0.02kg/s mass flow rate, respectively, due to FVGs application. At $T_{in,EUSWH}$=313K, η_{HS} increases by 15.71% and 25.32% for 0.01 and 0.02kg/s.

Chapter 1
Introduction

Background and Motivation

Waste heat recovery (WHR) is the process of capturing and reusing excess thermal energy that is typically lost to the environment during industrial processes, power generation, and other thermal applications. Instead of allowing this heat to dissipate, waste heat recovery systems convert it into useful energy, such as electricity or additional thermal power, improving overall efficiency and sustainability. The development of waste heat recovery systems is driven by the need for energy efficiency, cost reduction, and environmental sustainability. A significant portion of energy in industries and power plants is lost as heat, contributing to wasted resources and increased greenhouse gas emissions. By recovering and utilizing this heat, industries reduce fuel consumption, lower operational costs, and minimize their carbon footprint. Additionally, waste heat recovery plays a crucial role in enhancing energy security, reducing dependence on fossil fuels, and promoting sustainable energy solutions (Johnson et al., 2008). Low-grade waste heat recovery refers to the process of capturing and utilizing waste heat with temperatures typically below 250°C. This type of heat is commonly found in industrial processes, power plants, automotive exhaust, and residential heating systems. Unlike high-temperature waste heat, which can be directly reused for power generation, low-grade waste heat is more challenging to recover due to its lower energy density and reduced thermal potential.

A typical waste heat recovery system operates through several key steps to efficiently capture, convert, and utilize excess thermal energy. Firstly, the system extracts waste heat from high-temperature sources such as exhaust gases, hot surfaces, or process

fluids. This is achieved using specialized thermal recovery devices, including heat exchangers, recuperators, regenerators, or thermoelectric generators (TEGs) (Jaafreh et al., 2022). Heat exchangers facilitate efficient heat extraction by allowing thermal energy transfer between the waste heat source and a secondary working fluid, while TEGs directly convert thermal gradients into electricity using the Seebeck effect. Once captured, the thermal energy must be efficiently transferred to a working fluid, which can be air, water, steam, or advanced heat transfer fluids like molten salts or phase-change materials. The heat transfer mechanisms involved include conduction (direct solid-to-solid transfer), convection (fluid-based transport), and radiation (electromagnetic heat transfer). The choice of working fluid and transfer mechanism is crucial, as it affects the system's thermal efficiency, pressure drop, and heat exchanger design. Then, the recovered thermal energy is then converted into a usable form, depending on the application. For electricity generation, thermoelectric modules can convert heat into electrical power, while mechanical systems such as Organic Rankine Cycle (ORC) or Stirling engines utilize thermodynamic cycles to produce mechanical work, which is further converted into electricity through generators. Alternatively, direct heat reuse is employed in industrial processes for preheating raw materials, improving combustion efficiency, or driving absorption refrigeration systems for cooling applications.

Consequently, the converted energy is either stored for future use or directly applied in various energy-demanding applications. Thermal energy storage (TES) systems, including sensible heat storage (using materials like water or rock beds), latent heat storage (phase-change materials), and thermochemical storage, enable heat retention for later use. If direct utilization is preferred, the recovered energy can be integrated into industrial heating systems, district heating networks, or hybrid renewable energy setups to enhance overall system performance. Finally, to maximize efficiency and adaptability,

modern waste heat recovery systems incorporate optimization techniques and advanced control algorithms. Predictive models, including machine learning-based optimization, dynamically adjust operational parameters such as flow rates, temperature gradients, and load demands to enhance energy conversion efficiency. Automated feedback mechanisms ensure minimal thermal losses and improved system reliability, while computational fluid dynamics (CFD) simulations aid in designing more efficient heat exchangers and thermal transport pathways. By integrating these sequential steps, which have been illustrated in Fig. 1.1, waste heat recovery systems effectively enhance energy efficiency, reduce environmental impact, and contribute to sustainable industrial and power generation practices.

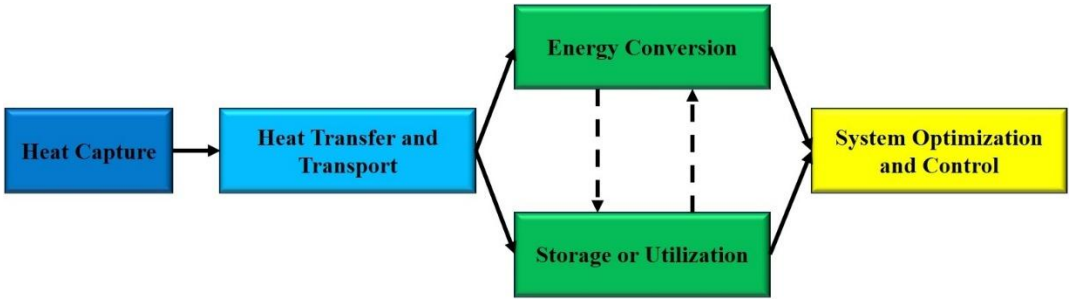

Fig. 1.1 Typical Waste Heat Recovery Processes

1.1 Advantages of Waste Heat Recovery Systems

Waste heat recovery (WHR) systems offer several benefits across industrial, commercial, and energy sectors by improving efficiency, reducing costs, and promoting sustainability. The key advantages include:

- Enhanced Energy Efficiency: WHR systems utilize otherwise wasted thermal energy, improving overall system efficiency by converting excess heat into useful power or thermal energy. This reduces fuel consumption in industrial processes and power generation.

- Reduced Operational Costs: By recovering and reusing heat, industries can lower energy bills and decrease dependence on primary energy sources. This leads to significant cost savings, particularly in energy-intensive sectors like manufacturing, metal processing, and chemical industries.
- Lower Environmental Impact: WHR systems contribute to sustainability by reducing greenhouse gas (GHG) emissions and overall carbon footprint. By improving fuel utilization, they help industries meet environmental regulations and emission reduction targets.
- Increased Power Generation Potential: Technologies such as thermoelectric generators (TEGs), Organic Rankine Cycles (ORC), and Kalina cycles convert waste heat into electricity, enhancing power generation capacity without additional fuel consumption (Armstead et al., 2013).
- Process and Equipment Longevity: Heat recovery reduces thermal stress on industrial equipment by maintaining optimal operating temperatures. This minimizes wear and tear, leading to extended equipment lifespan and reduced maintenance costs.
- Energy Security and Resource Conservation: WHR reduces reliance on fossil fuels and enhances energy security by optimizing available energy resources. This is particularly crucial in regions with high energy demand and limited natural resources.
- Hybrid Renewable Energy Integration: WHR can complement renewable energy sources like solar and biomass by stabilizing energy supply fluctuations. Waste heat from solar thermal or biogas plants can be recovered and utilized, improving overall system reliability.

- Technological Advancements and Innovation: The adoption of WHR systems drives research and development in advanced materials, nanofluids, heat exchangers, and machine learning-based optimization, paving the way for next-generation energy-efficient technologies.

By implementing waste heat recovery systems, industries, and power plants can significantly enhance energy utilization, reduce costs, and contribute to a more sustainable and environmentally friendly energy landscape.

1.2 Thermoelectric generator as a Waste Heat recovery method

The concept of thermoelectric power generation dates back to the early 19th century when Thomas Johann Seebeck discovered the thermoelectric effect in 1821. He observed that a voltage is generated in a closed circuit composed of two different conductive materials when subjected to a temperature gradient. This phenomenon, later termed the Seebeck effect, laid the foundation for thermoelectric technology. Over the years, researchers developed thermoelectric materials and improved efficiency, leading to applications in power generation and cooling (Degousée et al., 2021, Yin et al., 2022). During the mid-20th century, thermoelectric generators (TEGs) gained prominence, especially in space exploration, where radioisotope thermoelectric generators (RTGs) were used to power deep-space missions. TEGs have shown potential to be utilized in automotive, industrial waste heat recovery, and renewable energy applications. The Seebeck effect is the fundamental principle behind thermoelectric generators. It occurs when two dissimilar conductive or semiconductive materials form a closed circuit, and a temperature difference is applied at the junctions. This temperature gradient causes charge carriers (electrons or holes) to migrate from the hot side to the cold side, creating an electric potential (voltage). The magnitude of the voltage depends on the materials'

Seebeck coefficient and the temperature difference. The generated voltage can be harnessed for power generation, making the Seebeck effect a critical mechanism in thermoelectric energy conversion (Yin et al., 2022). A typical TEG consists of the following essential components:

- Thermoelectric Materials (P-Type and N-Type Semiconductors)– The core of a TEG consists of alternating p-type and n-type semiconductor legs, usually made from materials like bismuth telluride (Bi_2Te_3) or advanced nanostructured thermoelectric. These materials enable efficient charge carrier movement under a thermal gradient.
- Metallic Interconnects and Electrodes– Conductive metal strips connect the semiconductor legs electrically in series and thermally in parallel. This configuration ensures that the electrical voltage builds up while minimizing thermal losses.
- Ceramic Substrate Layers– A thermoelectric module is sandwiched between two ceramic plates, usually made of alumina (Al_2O_3) or other high-temperature-resistant materials. These plates provide mechanical strength, electrical insulation, and efficient heat transfer.
- Heat Source and Heat Sink– To generate power, a TEG module requires a hot side (attached to the heat source) and a cold side (attached to a heat sink or cooling mechanism). The larger the temperature difference, the higher the efficiency and power output.

By combining these components, thermoelectric generators efficiently convert waste heat into electrical energy, making them valuable for power generation in various applications.

1.3 Applications of TEG

Thermoelectric generators (TEGs) find diverse applications across multiple industries due to their ability to directly convert heat into electricity with high reliability and minimal maintenance. In waste heat recovery, TEGs are integrated into industrial processes, automotive exhaust systems, and power plants to harness otherwise lost thermal energy, improving overall energy efficiency. In space exploration (Peng et al., 2022), radioisotope thermoelectric generators (RTGs) power deep-space missions by converting heat from radioactive decay into electricity, ensuring the long-term operation of spacecraft. The automotive industry utilizes TEGs for vehicle energy recovery, converting exhaust heat into electrical power to improve fuel efficiency and reduce emissions (Kumar et al., 2021). In renewable energy systems, TEGs complement solar thermal (Manghwar et al., 2024, Sharma et al., 2022) and geothermal energy (Xie et al., 2023) by capturing excess heat and enhancing overall power output. Moreover, in wearable and biomedical applications (Miao et al., 2024), TEGs harvest body heat to power low-energy medical devices such as pacemakers and biosensors, offering self-sustaining energy solutions. Additionally, TEGs are employed in remote and off-grid power generation, providing a reliable source of electricity in harsh environments where conventional power sources are impractical. The ability of TEGs to operate without moving parts, coupled with advancements in thermoelectric materials and nanotechnology, continues to expand their applicability across emerging energy and technological sectors.

1.4 Objectives

The objectives of the present research are given as follows:

- ***To enhance heat extraction from exhaust gases by proposing a novel heat exchanger equipped with vortex generators (delta, envelope, and fishtail shape). This work seeks to determine the optimal geometrical arrangement (distance-to-height ratio and angle of inclination) that maximizes thermohydraulic performance.***
- ***To maximize the power output and conversion efficiency of the thermoelectric generator (TEG) by exploring its performance with varying specifications (TEG stages, leg geometry, and new materials). The goal is to quantify the influence of critical design parameters (number of rows of TEG legs, exhaust inlet temperature, and coolant flow rate) on TEG performance under different operating conditions.***
- ***To improve heat rejection on the TEG's cold side by investigating the use of hybrid nanofluids as coolants. This involves identifying the nanoparticle properties (shape aspects and volume fraction of the nanoparticles) and flow conditions (coolant flow rates) that optimize thermohydraulic and exergetic performance.***
- ***To systematically identify the most influential design parameters and create an accurate performance model using the Taguchi method and an Artificial Neural Network (ANN). This work seeks to obtain the optimal vortex generator shape and a high-fidelity predictive model.***
- ***To develop a more efficient and sustainable hybrid system by integrating the TEG with the application of a novel vortex generator (fishtail) with a solar water heater. The analysis seeks to evaluate the overall performance and energy synergy of the resulting hybrid system.***

1.5 Contribution of the study

This study makes a significant contribution to the advancement of thermoelectric generator (TEG) performance by systematically evaluating and integrating cutting-edge techniques for heat transfer enhancement, device optimization, and predictive modeling. By investigating hot-side heat transfer augmentation, particularly through the application of vortex generators, this research enhances thermal energy absorption, thereby improving the temperature gradient essential for efficient thermoelectric conversion. Furthermore, by exploring TEG device optimization, including novel thermoelectric materials, multi-stage configurations, and leg geometry modifications, this study provides valuable insights into balancing thermal and electrical transport properties to achieve higher energy conversion efficiency. Additionally, the incorporation of cold-side cooling enhancements, specifically through shape-dependent nanofluid and hybrid nanofluid performance analysis, demonstrates how effective thermal dissipation strategies can mitigate temperature buildup and maximize power output. The study also delves into Taguchi optimization methodologies, leveraging artificial neural networks and predictive modeling to fine-tune system parameters for superior efficiency. Lastly, the exploration of solar-assisted TEG hybrid systems highlights the potential of integrating renewable energy sources to boost TEG performance in sustainable applications. By addressing key performance limitations and proposing innovative strategies, this study serves as a foundation for future advancements in thermoelectric technology, fostering its integration into next-generation energy solutions.

1.6 Thesis structure and methodology

The present study is structured into eight comprehensive chapters, each addressing critical aspects of waste heat recovery (WHR) through thermoelectric

generators (TEGs). **Chapter 1** establishes the significance of waste heat recovery and the role of thermoelectric generators (TEGs) in energy harvesting. It highlights real-world applications of TEGs across various industries, sets the motivation for the study, and outlines the research objectives and thesis structure. **Chapter 2** presents a structured literature review focusing on five core areas: hot-side heat transfer enhancement, TEG performance optimization, cold-side cooling strategies, advanced optimization techniques, and solar-assisted TEG systems. It discusses vortex generators for heat transfer improvement, high-ZT thermoelectric materials, nanofluid-based cooling techniques, AI-driven performance modeling, and hybrid renewable energy integration. **Chapter 3** investigates the hot-side heat transfer enhancement using novel vortex generators (delta, envelope, and fishtail) in a heat exchanger coupled with a TEG. An experimental study examines the effects of vortex shape, spacing, and inclination on heat transfer coefficient, pressure drop, and overall thermal performance, aiming to identify an optimal design for improved TEG efficiency. **Chapter 4** develops a two-stage TEG with variable leg geometry and dissimilar thermoelectric materials to enhance performance. The study explores the impact of row configuration, exhaust inlet temperature, and coolant flow rate on power output and efficiency, identifying an optimal design for maximizing energy conversion. This study specifically focused on identifying the optimal combination of input factors to maximize the TEG's power output and conversion efficiency, with subsequent economic and environmental considerations planned for future research. **Chapter 5** examines the influence of hybrid nanofluids containing differently shaped nanoparticles, such as graphene, Al_2O_3, MWCNT, and Fe_3O_4, on the thermal performance of a mini channel heat sink used for TEG cooling. The study evaluates the heat transfer coefficient, Nusselt number, exergy, and Figure of merit to determine the best nanofluid composition for effective heat dissipation and enhanced

TEG power generation. **Chapter 6** analyzes the thermohydraulic performance of various vortex generator geometries in a rectangular channel under different ambient conditions for TEG. It evaluates delta, envelope, and fishtail-shaped vortex generators using Taguchi design of experiments (DOE), ANOVA, and signal-to-noise ratio analysis. Additionally, an artificial neural network (ANN) model is developed to predict performance trends and optimize heat exchanger efficiency. **Chapter 7** investigates a hybrid energy system combining an Evacuated U-tube Solar Water Heater (EUSWH) with a TEG, incorporating fishtail vortex generators for enhanced heat transfer. The study systematically evaluates the effects of solar radiation, water flow rate, and inlet temperature on the thermal and electrical performance of the integrated system, aiming to optimize renewable energy utilization. Finally, **Chapter 8** summarizes the key findings from all studies, highlighting critical parameters influencing TEG performance. It identifies the optimal design configurations and operational conditions for maximizing efficiency and outlines potential future research directions in thermoelectric energy harvesting.

Thus, this thesis aims to improve thermoelectric generator (TEG) performance by examining its three main parts: the hot-side heater, the TEG module, and the cold-side cooler. The research uses new experimental and computer models to achieve this. The study then expands to optimize the entire system and test a practical application in a hybrid solar setup. Although these topics are diverse, they all share the same goal: to find better ways to generate power with TEGs. For example, Chapter 3 tests different vortex generators to improve the hot side of the TEG, Chapter 4 develops a modified and improved TEG, Chapter 5 explores TEG cold side performance enhancement, Chapter 6 optimizes vortex generators from Chapter 3, and Chapter 7 uses the best one from that study in a hybrid system combining a TEG with a solar water heater.

This page is left intentionally blank

Chapter 2

Literature review

Overview: The literature review has been systematically categorized into five key areas: TEG hot-side heat transfer enhancement, TEG device performance improvement, TEG cold-side heat dissipation strategies, optimization methodologies, and solar-assisted TEG waste heat recovery systems. The first section explores advanced heat transfer augmentation techniques, particularly the role of vortex generators in improving thermal energy absorption and enhancing TEG performance. The second section delves into critical design parameters that influence TEG efficiency, including novel thermoelectric materials, multi-stage configurations for better temperature gradient management, and optimized leg geometries to balance electrical and thermal transport properties. The third section focuses on shape-dependent performance analysis of nanofluids and hybrid nanofluids, emphasizing their effectiveness in improving thermal management and cooling efficiency on the cold side of the TEG. The fourth section discusses optimization approaches and predictive modeling techniques, particularly the integration of artificial neural networks for performance enhancement and parameter tuning in TEG systems. Finally, the last section examines solar-assisted TEG hybrid systems, highlighting their synergistic benefits and performance improvements in renewable energy applications. Through this structured review, a comprehensive understanding of the latest advancements and innovative strategies for optimizing TEG-based waste heat recovery systems is established.

The efficiency and performance of a TEG are primarily governed by the temperature difference between the hot and cold sides, as well as the TEG configuration, including the choice of materials, the number of stages, and leg geometry. To enhance

heat transfer on the hot side, vortex generators have emerged as a simple yet effective solution for improving TEG performance. Additionally, advancements in TEG materials, multi-stage configurations, and various leg geometries have demonstrated significant improvements in power output. On the cooling side, the application of hybrid nanofluids has shown remarkable enhancement in thermal management, thereby boosting the electrical performance of TEGs. Consequently, the literature review for TEG performance enhancement has been structured accordingly, as illustrated in Fig. 2.1.

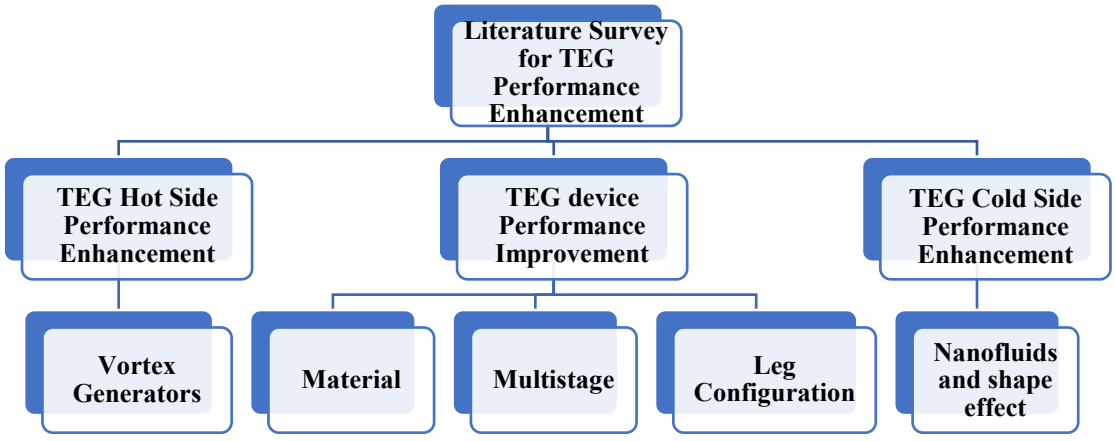

Fig. 2.1 TEG Performance Enhancement Literature Classification

2.1 TEG hot side performance enhancement

Enhancing heat transfer on the hot side of a thermoelectric generator (TEG) is crucial for maximizing its efficiency by maintaining a high-temperature gradient across the thermoelectric module. Effective heat transfer increases heat flux, reduces thermal resistance, and prevents excessive temperature drop, ensuring optimal energy conversion. Techniques such as extended surfaces, and turbulence promoters (vortex generators) improve convective heat transfer. These methods enhance fluid mixing, disrupt thermal boundary layers, and facilitate efficient heat delivery, ultimately leading to higher power

output, improved system longevity, and a more compact, lightweight design. Heat transfer enhancement relies on key physical phenomena such as boundary layer disruption, increased turbulence, vortex formation, enhanced mixing, and increased surface area for heat exchange. Vortex generators (VGs) achieve this by introducing streamwise or transverse vortices into the flow, which promotes better mixing of hot and cold fluid layers, reducing thermal resistance and enhancing convective heat transfer. These vortices disrupt the thermal boundary layer, increasing fluid velocity gradients and improving heat transfer rates. Additionally, VGs induce localized flow acceleration and recirculation, leading to higher convective heat flux. By optimizing VG shape, size, and arrangement, heat transfer performance can be significantly improved while maintaining manageable pressure drop levels. Table 2.1 comprehensively illustrates the impact of vortex generator installation on heat transfer enhancement and fluid flow dynamics within heat exchangers.

Table 2.1: Vortex generator configurations for heat transfer enhancement

Authors	Vortex generators	Remarks
Caliskan (2014)	Punched triangular and punched rectangular VG in a rectangular channel	Maximum increment in average Nusselt number for punched triangular and punched rectangular were 55% and 51.3% respectively in comparison to the smooth channel for an attack angle of 45° (Reynolds number variation 3288 to 37,817).

Ebrahimi et al. (2015)	Rectangular VG in a rectangular channel microchannel	Nusselt number and friction factor increased by 2-25% and 4-30% respectively when Reynolds number was varied from 100 to 1100.
Ebrahimi et al. (2015)	Rectangular VG in microchannel	The enlargement of the recirculation zone behind the VGs, enhanced fluid mixing, and decreased thermal boundary layer thickness resulted in enhanced heat transfer performance at a high Reynolds number. Reynolds number was varied from 100 to 1100.
Wang et al. (2016)	Rectangular fins, cylindrical grooves, and deflectors in exhaust heat exchanger	The cylindrical grooves improved the heat transfer and reduced the back pressure. Furthermore, a portion of the heat exchanger uncovered with thermoelectric modules at the downstream section could make the upstream section hotter and make full use of each TEG.
Ahmed et al. (2017)	Triangular VG in a triangular duct	The maximum pressure drop increased was less than 10% while

		the heat transfer improved by 45.7% for 3 vol.% of Al_2O_3 at Re=16000.
Samadifar et al. (2018)	Simple rectangular, rectangular trapezoidal, angular rectangular, wishbone, intended, and waved VGs in a plate-fin heat exchanger	A simple rectangular vortex generator exhibited the highest gain in heat transfer performance of 7% and an angle of installation of 45° was found to be the most effective (Re=200).
Jiansheng et al. (2019)	Miniature cuboid VG in a rectangular channel	The synthesis performance of heat transfer and flow was enhanced by 8.15% relative to the smooth channel. Reynolds no. used was 3745.
Zhang et al. (2020)	Rectangular and V-shaped VG in a circular tube	The tube equipped with P-RWVGs exhibits an enhancement in heat transfer rate ranging from 54% to 118% and an increase in flow resistance between 152% and 568% compared to a smooth tube. Similarly, for the tube with V-RWVGs (V-shaped rectangular winglet vortex generator), the heat transfer rate improves by 60% to 118%, while the flow resistance

		rises by 141% to 644%. The experiments were conducted in the Reynolds number range of approximately 6000–20000.
Tian et al. (2020)	Triangular VG in a circular tube	For a thermally efficient heat exchanger, the location of the VGs concerning the center line walls plays an important role. The Reynolds number was considered to be between 4000 and 12000.
Carpio et al. (2021)	Delta VG in a compact heat exchanger	The minimum and maximum increase in Nusselt number due to vortex generators were observed to be 19% and 102% at Reynolds numbers 400 and 2000, respectively.
Demirag et al. (2022)	Conic VG in a rectangular channel	The Nusselt number improved by 58.75% in comparison to the smooth channel and an 8.42% increment in the thermal enhancement factor was observed for the lowest Reynolds number value (Re = 5000–20,000).
Das et al. (2023)	Butterfly-wing VG in a rectangular microchannel	The Nusselt number increased by 92%, 26%, 12%, 2.9%, and 2%

		when Reynolds number (142-544), upper width (0.24-0.36mm), wing height (0.2-0.35mm) lower width (0.12-0.24mm) and length of the vortex generators (1-3mm) were varied.
Wu et al. (2024)	V-winglet in a circular tube	Nusselt number increased in the range of 130.56-156.43% when the pitch (25-75mm) of the vortex generators was varied. The highest performance enhancement factor of 2.83 was obtained at a pitch of 25mm with 8 winglets (Re=7000-17000).

Thus, from the above literature, we observed how vortex generator configurations (shapes of VGs, distance between consecutive VGs, angle of inclination) help in the heat transfer enhancement in different applications. Karana and Sahoo (2021), investigated an exhaust heat exchanger experimentally to improve the output of a TEG-based WHR system by dividing the heat exchanger into computational domains (Niu et al., 2014) and employing the 1-D thermal resistance method in conjunction with relevant heat transfer correlations (Bergman et al., 2011). The uncertainties associated with the experiment were effectively calculated for all the parameters (Kline & Mcclintock, 1953). The maximum thermohydraulic efficiency factor achieved was 1.93. Furthermore, the study predicted a reduction in the twisted tape-equipped heat exchanger size for the same TEG

power output as the smooth heat exchanger. Furthermore, Ma et al. (2015) assessed the feasibility of employing longitudinal vortex generators (LVGs) to enhance heat transfer in thermoelectric generators (TEGs). A coupled fluid-thermal-electric model was developed using COMSOL Multiphysics to analyze the influence of LVG height, LVG attack angle, and hot-side inlet gas temperature on TEG performance. The results indicated that the optimal performance was achieved when the LVGs extended across the full height of the channel at the highest examined temperature (550K). Under these conditions, heat input, net power output, and thermal conversion efficiency improved by 29%–38%, 90%–104%, and 31%–36%, respectively, compared to a smooth flow channel. Also, in a study, the influence of longitudinal vortex generators (LVGs) on the performance of a thermoelectric power generator (TEG) integrated with a plate-fin heat exchanger was investigated (Ma et al., 2017). The results revealed that the presence of LVGs induced complex three-dimensional vortices in the cross-section downstream of the LVGs, thereby enhancing heat transfer and electrical performance compared to a TEG without LVGs. Under baseline operating conditions, the heat input and open-circuit voltage of the TEG with LVGs were increased by 41–75% in comparison to a TEG with a smooth channel. In a study (Pal et al., 2012), simulations were performed on a heat exchanger with winglet vortex generators. They revealed a major heat transfer increase because the winglets created strong swirling vortices. This mixing effect thinned the thermal layer, enabling potential miniaturization of future heat exchangers. However, the aforementioned studies have not investigated the effect of vortex generator shape, distance-to-height ratio, and inclination angle on TEG performance.

2.2 TEG device performance improvement

The performance of a thermoelectric generator (TEG) is significantly influenced by the selection of p-type and n-type materials, the number of stages, and the geometry

of the TEG legs. The choice of thermoelectric materials determines the Seebeck coefficient, electrical conductivity, and thermal conductivity, all of which directly impact the Figure of merit (ZT) and overall efficiency. High-performance materials with optimized transport properties enhance power output and conversion efficiency. Additionally, the number of stages in a TEG module affects its ability to handle large temperature gradients, with multi-stage configurations enabling higher thermal-to-electric conversion efficiency by optimizing temperature distribution across each stage. Furthermore, TEG leg geometry, including length, cross-sectional area, and aspect ratio, influences heat conduction, electrical resistance, and mechanical stability. Optimizing leg dimensions ensures minimal parasitic losses and maximized energy conversion. By strategically selecting high ZT materials, employing multi-stage architectures, and refining leg geometry, TEG performance can be significantly improved, leading to enhanced power generation and efficiency. Several literatures are available that give a deep insight into the above-mentioned practices to improve the TEG performance for waste heat recovery.

2.2.1 TEG materials

The development of new thermoelectric materials is crucial for enhancing the efficiency, scalability, and practical applicability of thermoelectric generators (TEGs). The performance of a TEG is primarily determined by the dimensionless Figure of merit (ZT), which depends on the Seebeck coefficient, electrical conductivity, and thermal conductivity of the material. Conventional thermoelectric materials, such as bismuth telluride (Bi_2Te_3), have reached performance limits in many applications, necessitating the exploration of alternative materials with superior thermoelectric properties. New materials can offer improved efficiency, reduced material costs, and better thermal and mechanical stability under varying operating conditions. Additionally, the search for

environmentally friendly, abundant, and non-toxic materials is essential for large-scale deployment in waste heat recovery, energy harvesting, and industrial applications. Organic thermoelectric materials are gaining attention over conventional thermoelectric materials due to their low thermal conductivity, flexibility, lightweight nature, and cost-effective fabrication (Massetti et al., 2021). They are composed of earth-abundant, non-toxic elements, making them more sustainable and scalable. Additionally, their electronic properties can be tuned through molecular engineering, enabling tailored performance for specific applications. While challenges such as lower electrical conductivity and thermal stability remain significant hurdles for wider adoption, concerted advancements in nanomaterial design, composite engineering, and the development of sophisticated hybrid systems are steadily enhancing their viability for next-generation flexible electronics and energy harvesting applications. These advancements are enhancing their performance and durability, making them increasingly viable for next-generation applications in wearable technology and efficient energy harvesting from ambient sources. Achieving a ZT value greater than 1 is challenging because the material's electrical conductivity, thermal conductivity, and Seebeck coefficient are interdependent. Optimizing one often negatively impacts another. Low ZT (<1) results in poor energy conversion efficiency, generating insufficient electrical power or providing weak cooling, which severely limits practical applications for waste heat recovery. Substantial progress in thermoelectrics has been driven by a worldwide research effort focused on synthesizing high-performance materials, with notable breakthroughs in thin-film architectures (Venkatasubramanian et al., 2001), quantum-confined structures (Harman et al., 2002), and advanced semiconductors (Majumdar, 2004). Table 2.2 discusses some of the different thermoelectric materials being developed in recent times.

Table 2.2: Summary of different TEG materials

Author	TEG Material	Remarks
Sun et al. (2012)	poly[Kx(Ni-ett)] (Full name- poly(Nickel-1,1,2,2-ethylene tetrathiolate))	The n-type material exhibited a power factor of 147μW/mK^2 and a ZT value of 0.31 at 440K.
Kim et al. (2013)	PEDOT:PSS treated with Ethylene glycol (EG)/ Dimethyl sulfoxide (DMSO)	The Seebeck coefficient, electrical conductivity, and thermal conductivity obtained for the p-type material at room temperature were 73μV/K, 880S/cm, and 0.33W/mK respectively.
Zhao et al. (2014)	BiCuSeO oxyselenides	The Seebeck coefficient and electrical conductivity of the p-type material were 349μV/K and 1.12S/cm respectively.
Menon et al. (2015)	poly[Kx(Ni-ett)] (Full name- poly(Nickel-1,1,2,2-ethylene tetrathiolate))	A high-power density of 1–3mW/cm^2 was obtained after the material synthesis.
Sun et al. (2016)	Electrochemically treated poly[Kx(Ni-ett)]	The Seebeck coefficient, electrical conductivity, and thermal conductivity obtained for the n-type material were -150μV/K, 310S/cm, and 0.84W/mK respectively at 400K.

Chen et al. (2017)	Ni/PVDF (Ni nanowires within poly(vinylidene fluoride))	The Ni/PVDF nano-composites demonstrated unusual decoupling of electrical conductivity and the Seebeck coefficient concerning Ni content. With 80 wt% Ni at 380K, they achieve a peak power factor of 220μW/mK and a ZT value of 0.15.
Wang et al. (2018)	PEDOT/Bi_2Te_3	The p-type material exhibited a power factor of 1350μW/mK^2 and a ZT value of 0.58 at room temperature.
Karana and Sahoo (2019)	$Ag_{0.8}Pb_9Sn_9Sb_{0.6}Te_{20}$ and $Ag_{0.8}Pb_{19+x}SnSbTe_{20}$	Doping has a strong impact on TEG performance.
Chen et al. (2020)	$Bi_{0.4}Sb_{1.6}Te_3$	Optimized TEG gives 21.95% higher power than equally segmented TEG.
Chen et al. (2021)	$Ag_2Se_{1-x}Te_x$ (x = 0.1, 0.2, 0.3, 0.4, and 0.5)	Ultralow lattice thermal conductivity in the range of 0.21−0.31W/mK at 300K.
Jiang et al. (2022)	PEDOT:PSS	The highest power factor of 86.3μW/mK^2 measured at 313K was obtained. It also exhibits excellent environmental stability

		with less than 10% variation in resistance for 28 days at room temperature.
Liu et al. (2023)	PEDOT:PSS flexible thin films	The power factor of PEDOT:PSS films was improved by using a water-based solution. A high power factor of 64.4μW/mK^2 is achieved in PEDOT:PSS films at 360K.
Xia et al. (2024)	PEDOT:PSS/SWCNTs	Ultrahigh power factors of >500 and 185μW/mK^2 in p- and n-type hybrid films respectively.

2.2.2 TEG multi-staging

The number of stages in a thermoelectric generator (TEG) plays a crucial role in managing large temperature differentials effectively. In a multi-stage configuration, thermoelectric elements are arranged in a series of cascaded layers, where each stage operates within an optimized temperature range. This staged approach reduces thermal losses, enhances energy conversion efficiency, and prevents excessive thermal stress on individual thermoelectric materials. By strategically distributing the temperature gradient across multiple stages, multi-stage TEGs can achieve improved thermal-to-electric conversion efficiency compared to single-stage systems, making them particularly beneficial for applications involving high-temperature heat sources. Table 2.3 comprises multiple pieces of literature showcasing the benefits of increasing stages in a TEG module.

Table 2.3: TEG multi-staging

Author	TEG leg geometry	Remarks
Arora et al. (2015)	Single and two-stage	Multi-objective optimization depicts improvement in TEG performance by multi-staging.
Arora et al. (2016)	Two-stage	The efficiency performance of TEG improved by 16.6% for two-stage configurations.
Ahmadi Atouei et al. (2017)	Two-stages	The proposed TEG system gives 27% higher electrical potential than a single-stage system.
Ahmadi Atouei et al. (2017)	Multi-stage	Maximum power density rises by 79.08%, and maximum conversion efficiency increases by 96.47% when TEG is multi-staged.
Cheng et al. (2018)	Multi-stage	The maximum percentage increment in conversion efficiency and power densities were 96.47% and 79.07% respectively.
Sun et al. (2019)	Two-stages	Two-stage TEG system results in power and efficiency values of 1.96W and 10.14% respectively.

Zhao et al. (2020)	Two-stages	Maximum power density and efficiency upsurges by 4.33% and 64.25% respectively with two-stage TEG.
Yin et al. (2021)	Multi-stage	Compared to the single-stage TEG, a remarkable increase of 36.40% for output power and 34.47% for conversion efficiency is achieved respectively in the multi-stage.
Maduabuchi et al. (2022)	Single and multi-stage	The proposed TEG with tapered legs (trapezoidal and X-legs) improves the exergetic efficiency.
Qi et al. (2023)	Two-stage	Two stages give the maximum power and efficiency of 9.872W and 4.9% respectively.
Yang et al. (2024)	Two-stage	Maximum single and two-stage TEG conversion efficiencies are 1.9% and 2.6% respectively.

2.2.3 TEG leg geometry

The geometry of TEG legs, including their length, and cross-sectional area plays a critical role in determining the device's thermal and electrical performance. The leg dimensions directly influence heat conduction, electrical resistance, and mechanical integrity. Longer legs increase thermal resistance, reducing heat leakage but also raising

electrical resistance, which can lower power output. Conversely, a larger cross-sectional area decreases electrical resistance, improving electrical conductivity but also increasing heat conduction, which may reduce the temperature gradient necessary for efficient energy conversion. Therefore, careful optimization of leg geometry is essential to minimize losses, maintain structural stability, and enhance overall energy conversion efficiency. Different literature exhibiting the impact of TEG leg geometry has been compiled in Table 2.4.

Table 2.4: TEG leg geometries

Author	Stages	Remarks
Erturun et al. (2015)	Rectangular and cylindrical 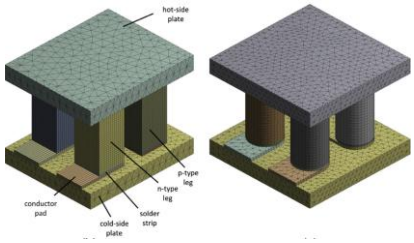	Power output and conversion efficiency increase with increasing leg width and decreasing leg length.
Arora et al. (2016)	Rectangular 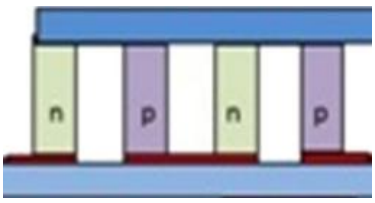	The optimized series and parallel configurations gave output powers of 3.42W and 3.85W respectively.
Lamba et al. (2017)	Flat and trapezoidal 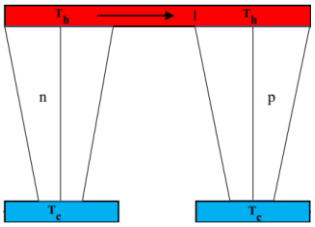	Trapezoidal geometry improves the energy and exergy efficiency of the device.
Zhang et al. (2018)	Annular leg	The maximum output power per unit mass was attained only

	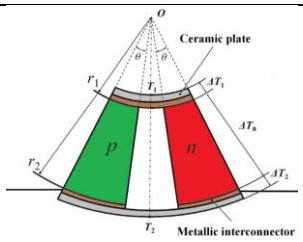	when the cross-section area of the thermoelectric leg was constant for the ideal annular TEG.
Karana and Sahoo (2019)	Asymmetrical and segmented leg 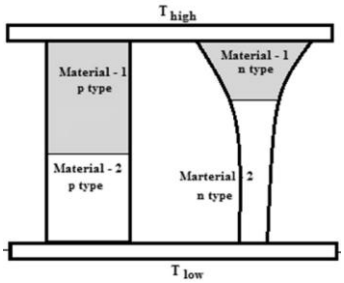	The output current and overall efficiency of the segmented TEG increases approximately by 33.3% and 5% when the temperature ratio is varied from 0.45 to 0.55.
Lee et al. (2020)	Square, cylindrical, and trapezoidal 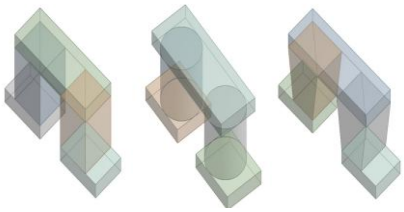	Trapezoidal geometry emerged as the best leg geometry with output power and conversion efficiency of 0.73W and 13.2% respectively.
Maduabuchi et al. (2021)	X-leg 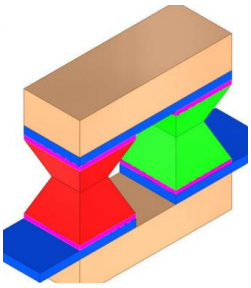	It was highly recommended that X-legs should be adopted whether in single or double-stage Solar-TEG configurations.
Ramos-Castañeda et al. (2021)	Rectangular and trapezoidal 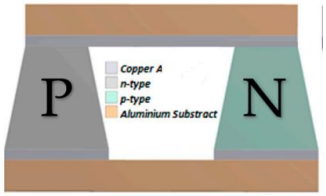	The maximum efficiency between the five geometry types was 5.53%, with a substrate of 110 × 100mm^2.

Ge et al. (2022)	Internal arc 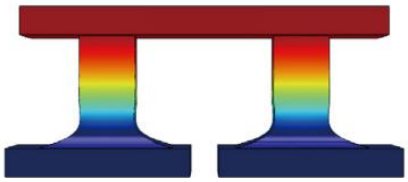	The internal arc X exhibited a maximum conversion efficiency of 3.28%.
Khalil et al. (2023)	Rectangular, pin, and cone 	Rectangular leg produced the highest power and conversion efficiency of 0.3019W and 12.47% for leg height of 1 and 4.5mm respectively.
Aljaghtham (2024)	Nine geometries (Rectangular, cylindrical, etc.) 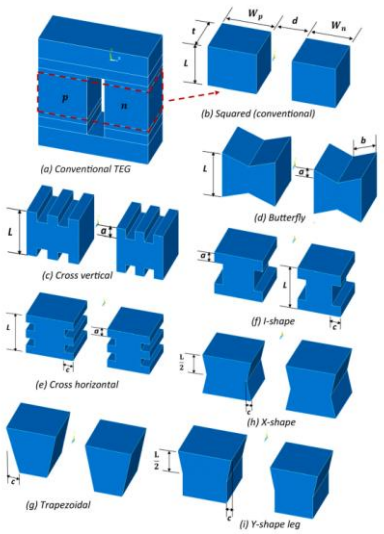	The cross-vertical and butterfly-shaped leg exhibited 31% higher energy efficiency than the conventional leg.

Thus, the above literature comprehensively explores the role of TEG material, leg geometry, and stages. It becomes important to take such measures to improve TEG performance and make it compatible with wider temperature applications. Sun et al. (2014), studied two-stage serial and parallel thermoelectric generator models using temperature-dependent bismuth telluride and skutterudite materials with an internal

combustion engine's exhaust as the heat source. Results show heat source temperature is crucial for design choice, with two-stage systems outperforming single-stage ones in power, efficiency, and exergy efficiency at higher temperatures. Sahoo and Karana (2020), analyzed a novel tapering segmented pin design for thermoelectric generators using modified bismuth and lead telluride materials, highlighting that higher load resistance ratios improve efficiency, with exergy efficiency strongly influenced by the shape factor. Furthermore, carbon-based semiconductors have garnered significant interest as promising thermoelectric materials for low-temperature energy harvesting due to the plentiful availability of their constituent elements, simplicity in fabrication processes, and naturally low thermal conductivity. For instance, PEDOT:PSS/SWCNTs films were explored by Xia et al. (2024), and obtained very high power factor of over 500 and 185μW/mK^2 and normalized power density of 2.5μW/cm^{2}K^2. Rathi et al. (2024), observed a notable improvement in the thermoelectric performance of PEDOT by developing an innovative ternary composite film incorporating Bi_2Te_3. The composite films exhibited increased Seebeck coefficient, electrical conductivity, and power factor compared to pure PEDOT:PSS films, with Bi_2Te_3 contributing higher Seebeck coefficients due to its intrinsic thermoelectric characteristics. Furthermore, pieces of literature (Liu et al., 2017, Sun et al., 2016) suggested that poly[Kx(Ni-ett)] is a novel thermoelectric material as it is lightweight, mechanically flexible, and derived from abundant resources, can be fabricated using cost-effective solution-based methods, making them more suitable than their inorganic counterparts for powering portable and wearable electronics. Because of the above-mentioned advantages based on properties and applications, the novel organic thermoelectric materials (PEDOT:PSS, PEDOT:PSS/ Bi_2Te_3, and poly[Kx(Ni-ett)]) with trapezoidal leg geometry for two stages have been found reasonable for TEG applications.

2.3 TEG Cold side heat transfer enhancement

2.3.1 Shape-based performance of nanofluids and hybrid nanofluids

Efficient cooling on the cold side of a TEG is essential to maintain a high-temperature difference (ΔT), which directly influences power generation efficiency and system longevity. Hybrid nanofluids, composed of multiple nanoparticles dispersed in a base fluid, enhance cooling by improving thermal conductivity and convective heat transfer, ensuring better heat dissipation. The shape of nanoparticles plays a crucial role in heat transfer and fluid flow, with elongated and high-aspect-ratio particles (e.g., cylindrical, platelets, cubic) offering superior thermal transport but potentially increasing viscosity and flow resistance. Optimizing nanoparticle shape and composition in hybrid nanofluids enables enhanced cooling performance, leading to improved TEG efficiency and energy conversion. Table 2.5 covers the studies dedicated to ascertaining the impact of nanoparticle shape on the coolant performance.

Table 2.5: Nanoparticles and their shape effects

Authors	Nanoparticles	Remarks
Elias et al. (2014)	Boehmite alumina (γ-AlOOH) Shapes: cylindrical, bricks, blades, and platelets	Maximum overall heat transfer coefficient is observed for cylindrical shaped nanoparticles at 1% vol. fraction.
Ellahi et al. (2015)	Cu Shapes: cylindrical, bricks, and platelets	Nusselt number increased by 17.53%, 11.55%, and 21.39% for cylindrical, brick, and platelet shape-based nanofluid for φ=0.08 than the base fluid.

Reddy et al. (2016)	Al_2O_3, TiO_2 Shape: Spherical	The temperature profile enriches due to an increase in the thermal boundary layer with the introduction of nanoparticles.
Khan et al. (2017)	Cu Shapes: platelet, cylindrical, and brick	The platelet-shape-based nanofluid performs better thermally followed by cylindrical and brick-shaped nanoparticles.
Liu et al. (2018)	Al_2O_3 Shapes: Sphere, platelet, blade cylinder, brick	For the nanofluid containing platelet-shaped particles with a 2% volume fraction, the Nusselt number increases up to 38.9% compared with base fluid followed by nanofluids containing nanoparticles with cylinder, blade, sphere, and brick shapes.
Kumar et al. (2019)	Al_2O_3, CuO Shapes: spherical, cylindrical, brick, platelets, and blades	The thermal conductivity is observed to be higher in spherical and cylindrical nanoparticle shapes and then followed by bricks, blades, and platelet shape nanoparticles. The dynamic viscosity of platelets shapes hybrid nanofluid is found to be maximum and followed by

		cylindrical, blades, bricks, and spherical shapes.
Benkhedda et al. (2020)	TiO_2, Ag Shapes: spherical, cylindrical, platelets and blades	Hybrid nanofluid with a blade-blade shape combination exhibited the highest Nusselt number of 42.3 at φ=0.06 and Re=1275.
Kumar et al. (2021)	Al_2O_3, CNT, graphene Shapes: spherical, cylindrical, and platelet	Hybrid nanofluid with spherical and platelet shape particles has 2.94% higher effectiveness compared to spherical and cylindrical shape nanoparticle-based hybrid nanofluid.
Ramzan et al. (2022)	Graphene (cylindrical), Ag (platelet), and CuO (spherical)	The heat dissipation capacity of graphene-Ag/H_2O is higher compared to that of graphene-CuO/H_2O. Additionally, in solar thermal energy systems, the Graphene-Ag/H_2O hybrid nanofluid containing cylindrical and platelet-shaped particles demonstrates superior performance compared to a combination of cylindrical and spherical particles.
Chu et al. (2023)	Au, Ag Shapes: blade, platelet, cylindrical, and brick	The velocity rate for brick-shaped nanoparticles is higher than the

		cylinder, platelet, and blade-shaped nanoparticles.
Yahyaee (2024)	Al_2O_3 Shapes: spheres, bricks, blades, cylinders, and platelets	The highest increment in thermal conductivity is for blade-shaped nanofluid (1.38%) while the maximum increment in kinematic viscosity was observed in platelet-shaped nanofluid (10.85%).

2.3.2 Mini channel heat sinks for nanofluids and hybrid nanofluids

Numerous researchers have explored diverse heat sink configurations to enhance the cooling efficiency of various heat-dissipating devices (Tuckerman and Pease, 1981). Advanced studies have focused on optimizing heat sink design (Shamsuddin et al., 2021), conducting comprehensive thermal (Yang et al., 2017) and hydraulic modeling (Bejan, 2013), performing energy and exergy analyses (Mahmoud et al., 2021), and evaluating key performance parameters (Liu et al., 2020), all while integrating practical considerations to ensure real-world applicability. For instance, Kumar and Sarkar (2019), investigated the heat transfer and pressure drop characteristics of a mini channel heat sink, experimentally and numerically, using hybrid nanofluids (volume concentration-0.1%). The heat sink comprised nine parallel rectangular mini channels, each with a depth of 3mm and a width of 1mm. The study observed a maximum enhancement in the convective heat transfer coefficient of 8.5% in numerical simulations and 12.8% in experimental tests when utilizing the Al_2O_3 (10:0) hybrid nanofluid. Bahiraei et al. (2019), evaluated the thermohydraulic performance of a hybrid nanofluid containing graphene–silver nanoparticles in a microchannel heat sink with ribs and secondary channels. The findings

revealed that integrating nanofluids, ribs, and secondary channels significantly enhanced heat sink efficiency.

Moreover, the convective heat transfer coefficient increased with higher nanoparticle concentration and Reynolds number, achieving a 17% improvement when the concentration rose from 0 to 0.1% at Re=100. In another study, the thermal efficiency of an aluminum mini channel heat sink with a rectangular cross-section was examined experimentally (Ataei et al., 2020). Distilled water, TiO_2–water nanofluid, Al_2O_3–water nanofluid, and a hybrid Al_2O_3/TiO_2–water nanofluid, each with a volume concentration of 0.5%, served as cooling fluids. A constant heat flux boundary condition was applied and sustained by a 36W heater positioned at the base of the heat sink. The convective heat transfer coefficient improved by up to 16.97% in comparison to pure water. Additionally, the wall temperature dropped by as much as 5°C when employing the Al_2O_3/TiO_2–water hybrid nanofluid instead of pure water. Also, the impact of article mixture ratios in hybrid nanofluids on mini channel heat sink performance was experimentally examined (Kumar and Sarkar, 2020). Water-based hybrid nanofluids were formulated with a total volume concentration of 0.01% using Al_2O_3 and MWCNT nanoparticles in different proportions (10:0, 8:2, 6:4, 4:6, 2:8, and 0:10). The highest improvements in heat transfer coefficient and pressure drop, recorded at 44.1% and 68.1%, respectively, were observed for the MWCNT nanofluid.

Hybrid nanofluids enhance TEG performance by significantly improving heat transfer at the hot side. Their superior thermal conductivity extracts more waste heat, creating a steeper temperature gradient across the TEG modules. This directly increases the voltage and power output according to the Seebeck effect. For instance, Selimefendigil et al. (2021) simulated a TEG cooled by nanofluids. The Ag/MgO-water hybrid nanofluid achieved the highest power output, up to 9.3% at Re=500. Performance

improved with Reynolds number and nanoparticle concentration. CNT-water was more effective at higher flow rates (Re=1500), yielding a 6.6% power increase. A review research (Garud et al., 2021) summarized using nanofluid-cooled TEGs for PV thermal management. The TEG harvests PV waste heat for extra power, while nanofluids enhance cooling. This integrated PV/T-TEG system synergistically improves overall electrical efficiency and performance, serving as a reference for future renewable energy innovations. Lastly, a study (Khatirzad & Sheikholeslami, 2025) found that combining pin/plate fins with MWCNT/SiC-water nanofluid cooling optimizes TEG performance. This configuration increased power output by 6.9% over standard plate fins and by 2.6% over water cooling alone, highlighting the critical role of advanced thermal management in enhancing energy harvesting. Although the use of hybrid nanofluids for improved TEG cooling has been studied, the performance enhancement attributable specifically to nanoparticle shape on the cold side represents a significant research gap.

Thus, for hot and cold sides of the TEG, vortex generators and hybrid nanofluids significantly enhance TEG performance by synergistically managing heat transfer on both sides of the module. On the hot side, vortex generators intensify convective heat transfer by disrupting thermal boundary layers and promoting turbulence, thereby increasing thermal energy input. Conversely, on the cold side, hybrid nanofluids, with their superior thermal conductivity, drastically improve waste heat extraction, which is critical for maintaining a high temperature gradient. Cited studies confirm their individual and combined efficacy in boosting heat transfer coefficients and, specifically, TEG power output. Furthermore, within the discussion on cold-side enhancement, additional research has been referenced to explicitly illustrate the established connection between the application of nanofluids and measurable performance gains in TEG systems.

2.4 Optimization methodology

Optimization techniques help in solving engineering problems by systematically finding the best possible solutions while considering constraints, efficiency, and performance metrics. These methods, such as genetic algorithms, gradient-based approaches, and machine learning-driven optimization, enhance design, resource utilization, and decision-making across various engineering applications. Various optimization techniques have been employed for studies related to vortex generator-based heat transfer enhancements in the past. Das and Hiremath (2023) numerically investigated a novel butterfly-wing vortex generator (VG) inside a microchannel. They utilized the Taguchi design of experiments to analyze thermohydraulic performance and entropy generation, employing an L_{27} orthogonal array with five factors and three levels. Signal-to-noise (S/N) ratio analysis and the TOPSIS decision-making method were applied to identify the optimal parameters from the Pareto front. The best input conditions were found to be w=0.48mm, b=0.12mm, l=1mm, h=0.38mm, and a Reynolds number of 544, yielding output responses of Pf =1.35 and $N_{s,a}$=0.67. Similarly, Feng et al. (2023) conducted computational studies on innovative VG designs, including longitudinal VGs, dimples/protrusions, and grooves, to enhance the airside performance of H-type finned tube heat exchangers. Using the Taguchi method, they examined the influence of geometric parameters on heat transfer, flow resistance, and overall thermal-hydraulic efficiency. At Reynolds numbers ranging from 4,650 to 28,300, the best design showed an improvement of 0.9–23.8%, 24.5–57.1%, and 8.3–37.5% over LVGs, dimples/protrusions, and grooves, respectively. A numerical study (Zeng et al., 2010) analyzed the effects of attack angle, VG length and height, fin material, fin thickness, fin pitch, and tube pitch on the performance of a vortex-generator fin-and-tube heat exchanger. The Taguchi method was used for optimization, revealing that six key factors

significantly influenced the JF factor. Two optimal conditions (A1B3C3D2E1F2G1H3 and A2B2C2D3E1F2G1H3) were identified, and their reproducibility was confirmed through analytical results. Additionally, a performance enhancement of 4.5–26.6% was observed compared to reference cases. Several other studies (Zhang et al., 2019, Xie et al., 2022, Li et al., 2023, Liang et al., 2023) have also focused on optimizing vortex generators to improve heat transfer efficiency. Hence, the optimization of different VG shapes in heat exchangers under different ambient conditions should be explored.

2.5 Solar-assisted TEG hybrid WHR systems

TEGs have also been integrated with solar-driven devices. Gharzi et al. (2023) proposed a parabolic trough collector-TEG (PTC-TEG) hybrid system, using pressurized heat transfer fluid (HTF) and TEG modules, achieving a 15.75% efficiency enhancement, combining improved thermal performance and additional electrical generation from absorbed solar radiation. A bidirectional solar thermoelectric generator (STEG) coupled with a latent heat storage and cooling system (LHSCS), proposed by Montero et al Montero et al. (2023) enables 24-hour power generation by storing waste heat during the day and using it at night. Experimental results showed 5% efficiency, 5735Wh annual electricity generation, and competitive costs compared to PV systems, offering a sustainable solution. Alobaid et al. (2023) evaluated frustum leg thermoelectric generators (FLTEGs) against trapezoidal and rectangular-leg designs using validated ANSYS simulations and neural networks. FLTEGs showed 5.7% higher power, 5.6% greater efficiency, and 2.7% reduced thermal stress under 100 Suns. Neural networks predicted performance 702 times faster, minimizing stress to 0.67GPa in optimized designs. Thus, researchers have studied SWH-TEG coupled systems (He et al. 2012, Zhang et al., 2013, Manivannan et al., 2022) in various aspects over the years. An efficient solar water heater (Zhang et al., 2024) and TEG (Shen et al., 2016) hybrid system with

proper validation (Khalil and Hassan, 2020) must be designed for further performance analysis. Although TEGs have been successfully integrated into solar water heating systems for improved efficiency and waste heat recovery, no study has yet developed a hybrid system equipped with an optimized vortex generator for the TEG's hot side.

2.6 Highlights

The literature survey has provided comprehensive insights into advanced methodologies for efficient waste heat recovery using thermoelectric generators (TEGs). Researchers have explored various strategies through both experimental and analytical approaches, thoroughly examining all critical aspects of TEG systems, including the hot side, the thermoelectric module itself, and the cold side. On the hot side, the incorporation of vortex generators has been shown to enhance convective heat transfer, thereby improving thermal energy input to the TEG. A detailed analysis of the TEG module has highlighted the significance of key design parameters, such as novel thermoelectric materials with improved Figure of merit (ZT), multi-stage configurations for optimized temperature gradients, and leg geometry modifications to balance electrical conductivity and thermal resistance. Additionally, on the cold side, the thermohydraulic performance of hybrid nanofluids has been investigated, revealing the influence of nanoparticle shape on heat transfer enhancement and fluid flow characteristics. These advancements collectively contribute to the development of a highly efficient, compact, and optimized TEG-based waste heat recovery system, paving the way for enhanced energy harvesting and sustainability in thermal management applications. Moreover, optimizing TEG parameters and integrating TEG with solar appliances pave the way for advanced research and technological advancements.

The core novelty of this work lies in the comprehensive and integrated investigation of multiple advanced strategies for TEG performance enhancement, which includes the study of novel vortex generators for hot-side heat transfer, a multi-stage TEG architecture, and a cold-side analysis using hybrid nanofluids with nanoparticle shape effects. While these components are studied individually, their novel integration within a single research framework, culminating in a hybrid solar-TEG system with temperature-dependent properties, provides unique and practical design guidance that extends beyond the current state of the art.

2.7 Research gaps and scope

Despite extensive research efforts, significant advancements are still required to make this technology commercially viable. The literature review clearly identifies key knowledge gaps, such as the lack of detailed studies on vortex generator configurations (including novel shapes, spacing, and angles) and their impact on TEG performance. It also highlights the absence of research combining advanced TEG materials, leg geometries, and multi-staging for synergistic improvements. Additionally, while hybrid nanofluids enhance cold-side cooling, their nanoparticle shape-dependent effects remain unexplored in TEG applications. The review further notes the lack of studies integrating Taguchi DOE for optimization with ANN-based predictive modeling, as well as the untapped potential of EUSWH-TEG systems with fishtail vortex generators. These gaps will guide future research. Identified research gaps highlight the need for a comprehensive analysis of TEG-based waste heat recovery (WHR) systems. This thesis aims to bridge these gaps by focusing on performance enhancement through advancements in TEG device architecture, thermal management on both hot and cold sides, and the development of a TEG-based hybrid system for simultaneous power generation and water heating. Key performance parameters, including power output,

conversion efficiency, heat transfer coefficient, Nusselt number, and pressure drop, are systematically evaluated using numerical and experimental approaches. The critical research gaps identified are as follows:

- For the hot side of the TEG, few vortex generator shapes have been analyzed in the literature. However, a detailed comparative analysis of vortex generator configurations (novel shapes, distance-to-height ratios, and angles of inclination of the VGs) along with its impact on TEG performance has not been found.
- Many scopes utilizing the application of novel TEG materials, different TEG leg geometry, and TEG multi-staging exist individually. However, utilizing the synergetic effect of all the aforementioned beneficial TEG aspects has not been previously done.
- Hybrid nanofluids improve the heat transfer rate on the cold side of the TEG and the shape of the nanoparticles play an important role in dictating the thermophysical properties of the nanofluid. However, this characteristic has not been employed to improve TEG performance on the cold side of the TEG.
- Open literature is not available where finding optimized TEG configuration using robust Taguchi DOE and further developing a prediction model utilizing Artificial Neural Network (ANN) has been performed.
- An Evacuated U-tube Solar Water Heater (EUSWH)-based TEG waste heat recovery system utilizing novel fishtail VG has not been explored in the literature available.

Chapter 3

TEG Hot Side Performance Enhancement using Vortex Generators

Overview: This chapter experimentally investigates advanced hot-side heat transfer enhancement for thermoelectric generators (TEGs). The heat exchanger's rectangular section is divided into computational domains analyzed with a 1-D thermal resistance model. After achieving stable conditions, energy conservation calculations are derived for each domain. The study analyzes how vortex generator geometry, distance-to-height ratio, and inclination angle affect thermohydraulic performance, including the heat transfer coefficient, pressure drop, and thermal enhancement factor. Using hot air, a comparative analysis identifies the optimal vortex generator configuration to maximize thermal efficiency and TEG power output.

3.1 Setup description

The configuration illustrated in Fig. 3.1 encompasses fundamental elements, such as a heat exchanger, a blower, a heater, and a data acquisition system for temperature measurement. The air is blown using a Cheston 500W blower and the HX receives hot air after being heated with a 2kW heater. The flow and air temperature are regulated to mimic the flow of an exhaust gas. Temperature measurements are conducted using a PT100 thermocouple. Fig. 3.2(a) illustrates placements of thermocouples (for internal and surface temperature measurements), tapping for pressure difference measurement, along with the HX inlet and outlet. Fig. 3.2(b) shows the computational model and elucidates the determination of the local heat transfer coefficient. In the thesis, the term control volume refers to the discrete computational domains used in the numerical model to discretize the rectangular flow channel along the direction of the hot air flow (the x-axis).

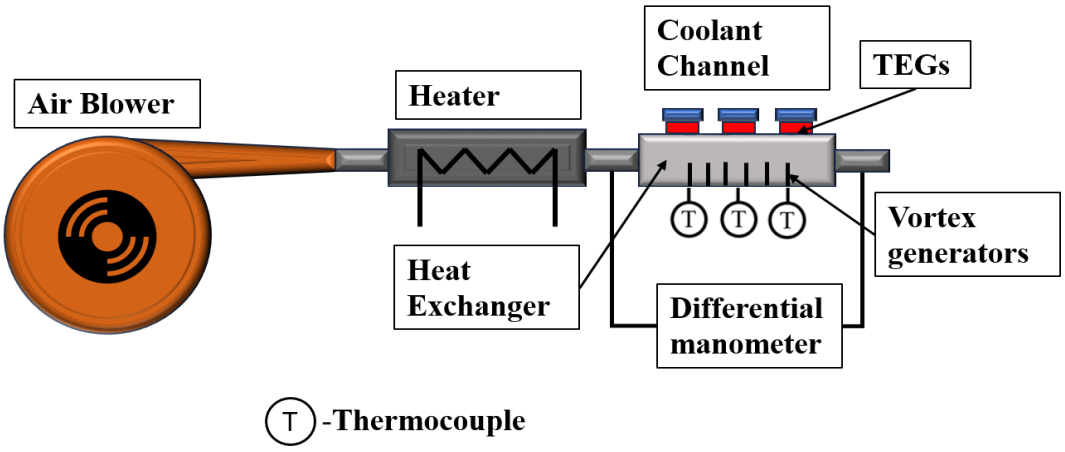

Fig. 3.1 Schematic diagram of the experimental setup

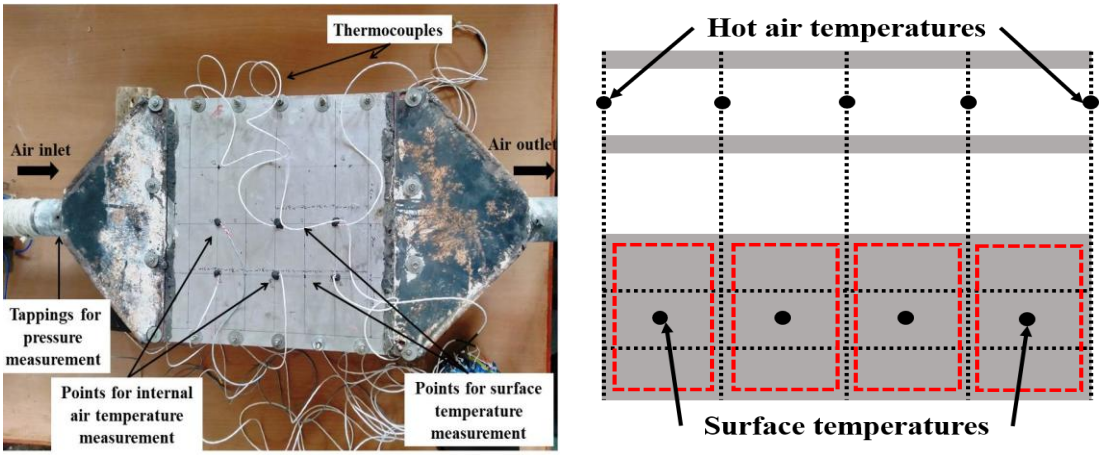

(a) **(b)**

Fig. 3.2 (a) Heat exchanger and placement of thermocouple (b) Division of the heat exchanger into Computational domains

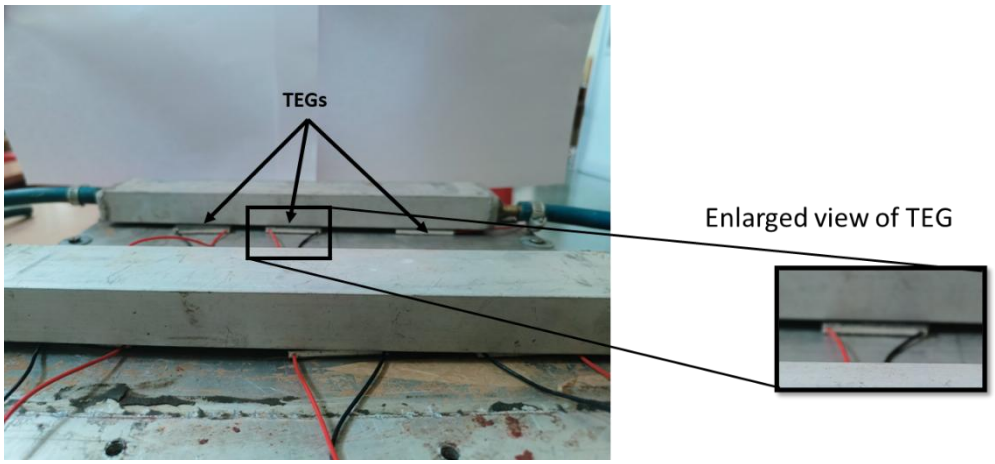

Fig. 3.2 (c) Thermoelectric Generator placement over the heat exchanger

These domains are dimensionless, discrete segments used for numerical analysis and are not thermodynamic control volumes in the classical sense. Additionally, Fig. 3.2(c). depicts TEG configuration.

The heat exchanger consists of three main sections: a diverging section, a rectangular channel, and a converging section. The rectangular section is of particular interest as it serves as the mounting surface for the thermoelectric generators, enabling power generation. The size of the heat exchanger plays a crucial role in waste heat recovery, as an excessively short length would limit the power output of the thermoelectric generators, whereas an overly long heat exchanger would lead to a significant increase in exhaust pumping power. The present uses hot air as the source of waste heat. The hot air properties resemble closely exhaust from an automobile. In the present study, the dimensions of the rectangular section are determined based on the recommendations provided by He et al. (2015), ensuring an optimal balance between power generation and system efficiency. The dimensions of the rectangular part of HX are 25mm (inclusive of plate thickness) in height and 290mm in width. To mitigate pressure-drop effects, the HX's length was constrained to a maximum of 300mm, given its direct correlation to pressure drop. After establishing the proportions of the HX, the selection of construction material became imperative. Aluminum was preferred for its commendable attributes of high thermal conductivity and corrosion resistance as the heat exchanger material. In this study, a modest thermoelectric generator design was employed. The TEG has a dimension of 40mm x 40mm x 3.6mm, it weighed 30gm. The operating temperature of the TEG is from 0°C to 120°C. the open circuit voltage rated by the manufacturer was 4.8V. The experimental setup emulates air as the heated gas enters the heat exchanger, engaging in heat exchange with the thermoelectric generators. The TEG consists of hot and cold sides; the former captivates thermal energy from the outer

face of the HX and transfers it to the thermoelectric generator, which generates electricity. The power generated is directly influenced by the thermal characteristics of HX. Thus, the HX is characterized by a diverging sector, a crucial rectangular canal that accommodates the thermoelectric generators for electricity generation, and a converging sector. The heat dissipated by the heated gas undergoes an equal transfer to both the top and bottom walls of the HX. It is corroborated by the closely matching temperatures (within ±0.2°C) observed on both the lower and upper surfaces of the HX.

3.1.1 Arrangement of VGs

The experimental investigation involves the utilization of three distinct types of vortex generators, namely the envelope (M), delta (D), and fishtail (F), as illustrated in Figs. 3.3(a-c). In the context of the experiment, the HX incorporates an array-style arrangement of vortex generators on its bottom surface, featuring 5 arrays, as depicted in Figs. 3.4(a) and (b). The quantification of VGs in each post is facilitated by the distance-to-height ratio, specified as the separation between consecutive vortex generators within the same column.

The VGs are examined for distance-to-height ratios: 2, 3, and 4. Four angles of inclination, namely 30°, 45°, 60°, and 90°, measured horizontally, are systematically investigated for each specified distance-to-height ratio, as delineated in Fig. 3.5, along with the display of the angle of inclination definition. The envelope and fishtail designs were chosen due to their potential to generate strong and organized vortices,. The delta shape, commonly used in aerospace and heat exchanger applications, was chosen due to its ability to generate longitudinal vortices that enhance thermal performance. In the pursuit of identifying optimal configurations and vortex generator settings, a comprehensive analysis comprising 37 distinct experiments was conducted.

- 1 for heat exchanger without VGs
- 3 for shapes (delta, envelope, and fishtail)
- 3 for D/H ratios (2, 3, and 4)
- 4 of inclination angles (30°, 45°, 60°, and 90°)

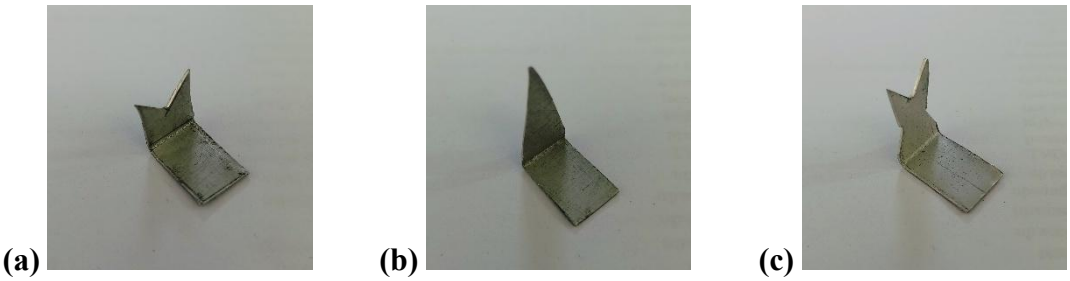

Fig. 3.3 (a) Envelope, (b) Delta, and (c) Fishtail vortex generators

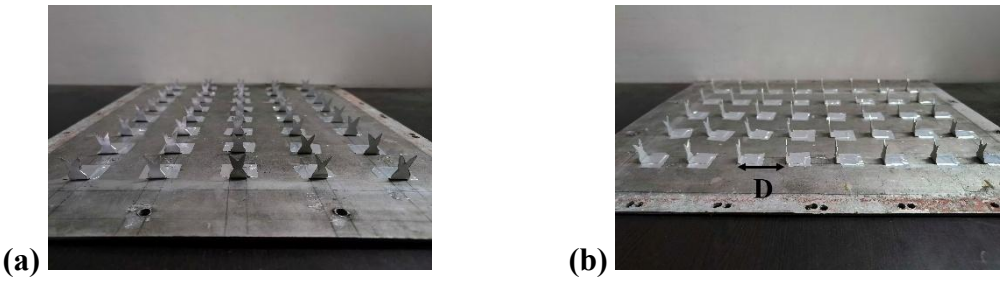

Fig. 3.4 (a) Front view and (b) Side view of VGs arrangement

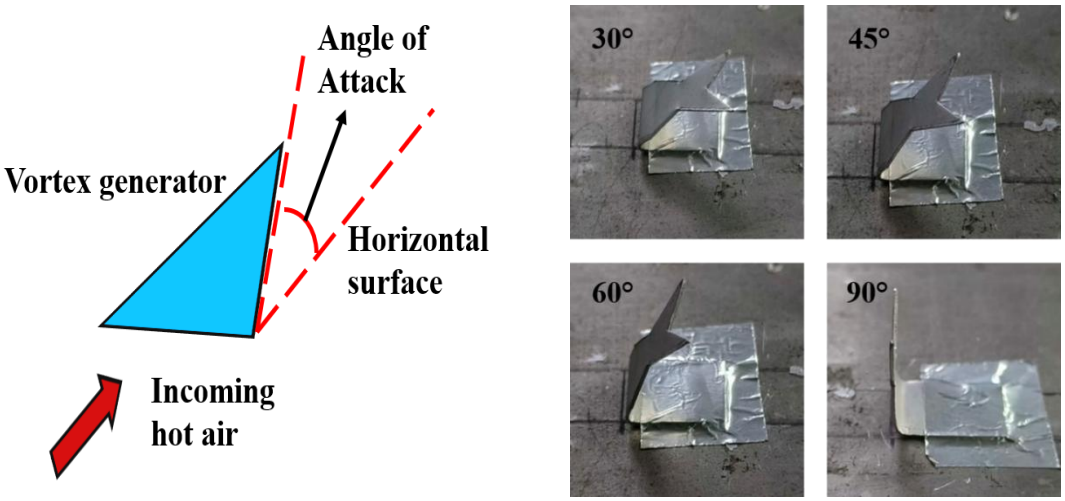

Fig. 3.5 Angle of inclination representation and the angles used in the present study

3.1.2 Mathematical Modeling

The analysis assumes a continuous and incompressible flow with constant thermophysical characteristics of air. The application of Navier-Stokes equations, Fourier's law, and no-slip wall condition are integral to the modeling process. A 1-D thermal resistance model is utilized to evaluate heat transport within the system. The heat exchanger (HX) is divided by flow-direction control units, facilitating the examination of individual interactions that govern bulk phenomena upon the entry of hot gas into the system. Heat transfer through convection occurs as the hot gas releases heat in each control unit, as represented by Eq. (3.1). Thermoelectric generators (TEGs) subsequently conduct and absorb this heat. Upon reaching a stable condition, the energy conservation calculations can be derived for each control system, delineating the heat dissipation within the control unit originating from the hot gas (Q).

$$\dot{Q} = \dot{m}_e * C_{p,e} * (T_{e,1} - T_{e,2}) \tag{3.1}$$

Herein, $C_{p,e,}$ and m_e denote the specific heat capacity and mass flow rate of the hot gas, respectively. The lower surface of the heat exchanger (HX), maintains temperatures within ±0.2°C uniformity. The temperature of the hot gas at a specific site is denoted as $T_{e,i}$. A hole drilled into the plate facilitates the placement of a thermocouple in the trail of the hot gas, allowing for the measurement of the temperature of the i^{th} section. The average control unit temperature can be computed utilizing Eq. (3.2).

$$T_{avg\ 1,2} = \frac{T_{e,1} + T_{e,2}}{2} \tag{3.2}$$

$\dot{Q}$ amount of heat is convected across the heat exchanger. The outside face temperature ($T_{out1,2}$) is measured experimentally, while the inner face temperature ($T_{in1,2}$) remains unknown. At a steady state, convection equals conduction heat transmission (Eq. 3.3). Mathematically,

$$h_{e,1}Ar\left(T_{avg1,2} - T_{in1,2}\right) = \frac{T_{in1,2} - T_{out1,2}}{R_{cond}} \tag{3.3}$$

Where $h_{e,1}$ is the internal convective HTC, and R_{cond} is heat-exchanger wall conduction resistance which is calculated using Eq. 3.4

$$R_{cond} = \frac{t_p}{k_{Al}\, Ar} \tag{3.4}$$

In the context of the Eq. 3.4 provided, Ar, k_{Al}, and t_p denote the cross-sectional area of the unit, the thermal conductivity of aluminum, and plate thickness, respectively. Eqs. (3.1-3.4) collectively determine the convective heat transfer coefficient ($h_{e,i}$) for each control volume. Consequently, the approximation of the typical internal HTC ($h_{avg,e}$) for the heat exchanger is derived as depicted in Eq. (3.5).

$$h_{avg,e} = \frac{\sum h_{e,i}}{i} \tag{3.5}$$

Here, the variable "i" represents the control unit number. The initial phase of experimentation involves subjecting the heat exchanger's flat internal topology to testing. As delineated in Figs. 4(a) and 4(b), F and D shape VGs are strategically positioned within heat exchangers to conduct a series of iterative trials. Parameters such as distance-to-height ratio and angle of inclination are systematically investigated. The assessment of the heat exchanger's performance is conducted under specific conditions: an airflow rate of 0.0116kg/s, and an ambient temperature of 31°C.

The study employs a 1-D thermal resistance model at steady state to analyze heat transfer on the hot side of the thermoelectric generator (TEG). This model is chosen due to its simplicity, computational efficiency, and effectiveness in capturing the key heat transfer mechanisms involved. The thermal resistance approach allows for a clear representation of heat flow through different layers, including convective heat transfer from hot air to the heat exchanger’s inner walls, conductive heat transfer through the

exchanger material, and further convection to the TEG surface. By using a steady-state assumption, the model simplifies complex transient effects, making it suitable for evaluating the overall thermal performance under stable operating conditions. This method provides an efficient way to quantify heat transfer rates and temperature gradients, which are critical for optimizing the heat exchanger design and improving TEG efficiency. The key assumptions in this work—like steady-state operation and constant material properties—were chosen for this reason. For instance, assuming a steady state means we analyzed the system when it was running steadily, not while it was starting up or changing speed. The experimental setup was run long enough so that the changes in the parameters being measured were negligible with time. This is a common approach that lets us clearly compare the performance of different designs. Similarly, assuming that properties like conductivity don't change with temperature greatly reduces calculation time while still providing accurate comparative results. This assumption is also considered as the properties do not vary drastically within the working range of the studies.

The power output of TEG can be determined using the correlation expressed as Eq. (3.6):

$$Power = K(\Delta T)^2 \tag{3.6}$$

Here, K = 0.002W/K^2 is a constant specified by the manufacturer, with the atmospheric temperature prevailing on the cold side. In heat transfer applications, friction factor holds significance, unswervingly influencing pressure drop. Eq. 3.7 determines the friction factor for a channel with an even cross-section:

$$f = \frac{(\Delta P/L)D_h}{(\rho V^2/2)} \tag{3.7}$$

Where ΔP, L, and D_h denote the pressure drop, channel length, and hydraulic diameter respectively. The thermal-hydraulic performance is expressed by TEF, as calculated by the relation in Eq. (3.8) (Karana and Sahoo, 2020):

$$TEF = \frac{\frac{Nu}{Nu_o}}{\left(\frac{f}{f_o}\right)^{1/3}} \tag{3.8}$$

The uncertainty (Kline and Mcclintock, 1953) in the determined constraints is computed utilizing the relation specified by the source referenced as:

$$U_F = \sqrt{\left(\frac{\partial F}{\partial x_i}U_1\right)^2 + \left(\frac{\partial F}{\partial x_i}U_2\right)^2 + \left(\frac{\partial F}{\partial x_i}U_3\right)^2 + \left(\frac{\partial F}{\partial x_i}U_4\right)^2 + \cdots} \tag{3.10}$$

Table 3.1 presents the maximum indecision associated with the measured parameters.

Table 3.1: Uncertainty of parameters used in the study

Parameter	Maximum Uncertainty
Dimension measurement	±1mm
Temperature	$\pm 0.1^0$C
Velocity	±0.1m/s
Heat transfer coefficient	2.96%
Heat transfer rate	2.19%
Pressure drop	±1mm

The relative errors in different parameter utilized in the study are as follows:

$$\frac{\partial Ar}{\Delta Ar} = \pm 0.01$$

$$\frac{\partial T}{T} = \pm 0.01$$

$$\frac{\partial v}{v} = \pm 0.01$$

$$\frac{\partial \dot{m}}{\dot{m}} = \pm 0.05$$

$$\frac{\partial \Delta P}{\Delta P} = \pm 0.01$$

$$\frac{\partial TEF}{TEF} = \pm 0.1$$

$$\frac{\partial Power}{Power} = \pm 0.01$$

3.2 Results and Discussion

3.2.1 Effect of vortex generators on the heat transfer coefficients

Figs. 3.6 (a-d) show heat transfer coefficient variation for different configurations along the length of the HX. The enhancement in the heat transfer coefficient with the incorporation of vortex generators in the heat exchanger is primarily attributed to the induced secondary flow structures that promote fluid mixing. Vortex generators disrupt the boundary layer, generating longitudinal vortices that increase turbulence intensity and enhance convective heat transfer. These vortices transport higher-momentum fluid from the core region toward the heat exchanger walls, thereby increasing the local heat transfer coefficient. Additionally, the breakdown of the thermal boundary layer due to vortex shedding facilitates better energy exchange between the hot air stream and the heat exchanger surface. Furthermore, it has been reported previously that vortex generator inserts are capable of production of local heat transfer enhancement (Deshmukh et al., 2016). Previous study (Pal et al., 2012) have also reported a significant enhancement in heat transfer because of the strong swirling motion originating from the streamwise longitudinal vortices behind the pair of delta winglets.

The observation that a distance-to-height (D/H) ratio of 2 results in the highest heat transfer coefficient across all vortex generator configurations is linked to the optimal interaction of vortices along the channel. At this spacing, the vortices retain their strength and effectively merge, sustaining a high level of turbulence and enhancing thermal mixing. When the D/H ratio increases beyond this value, the vortices tend to dissipate before interacting effectively with the subsequent vortex structures, leading to reduced enhancement. Conversely, at lower D/H ratios, excessive vortex interactions may induce flow recirculation and pressure losses, diminishing the convective heat transfer efficiency.

The superior performance of the fishtail vortex generator (FVG) compared to the M-envelope and delta vortex generators can be attributed to its distinctive aerodynamic shape, which generates stronger and more stable vortex structures. The fishtail configuration likely promotes the formation of larger coherent vortices that persist over a longer streamwise distance, thereby ensuring sustained enhancement in convective heat transfer. Moreover, the shape may also contribute to a more uniform velocity profile, reducing flow separation and minimizing pressure losses while maximizing heat transfer augmentation.

The inclination angle of 60° yielding the highest heat transfer coefficient can be explained through the balance between vortex strength and aerodynamic resistance. At lower inclination angles (e.g., 30 and 45°), the vortex generators induce weaker vortices due to a reduced flow disturbance, limiting their effectiveness in enhancing thermal transport. Conversely, at a high inclination of 90°, the vortex generators create significant flow resistance and excessive separation, leading to high-pressure drop penalties and flow stagnation, which counteract the heat transfer benefits. The 60° inclination provides an optimal orientation where the induced vortices are both strong and stable, maximizing turbulent energy transport while maintaining a favorable pressure drop-to-heat transfer

trade-off. This inclination ensures effective boundary layer disruption without introducing excessive drag, leading to the highest observed heat transfer coefficient.

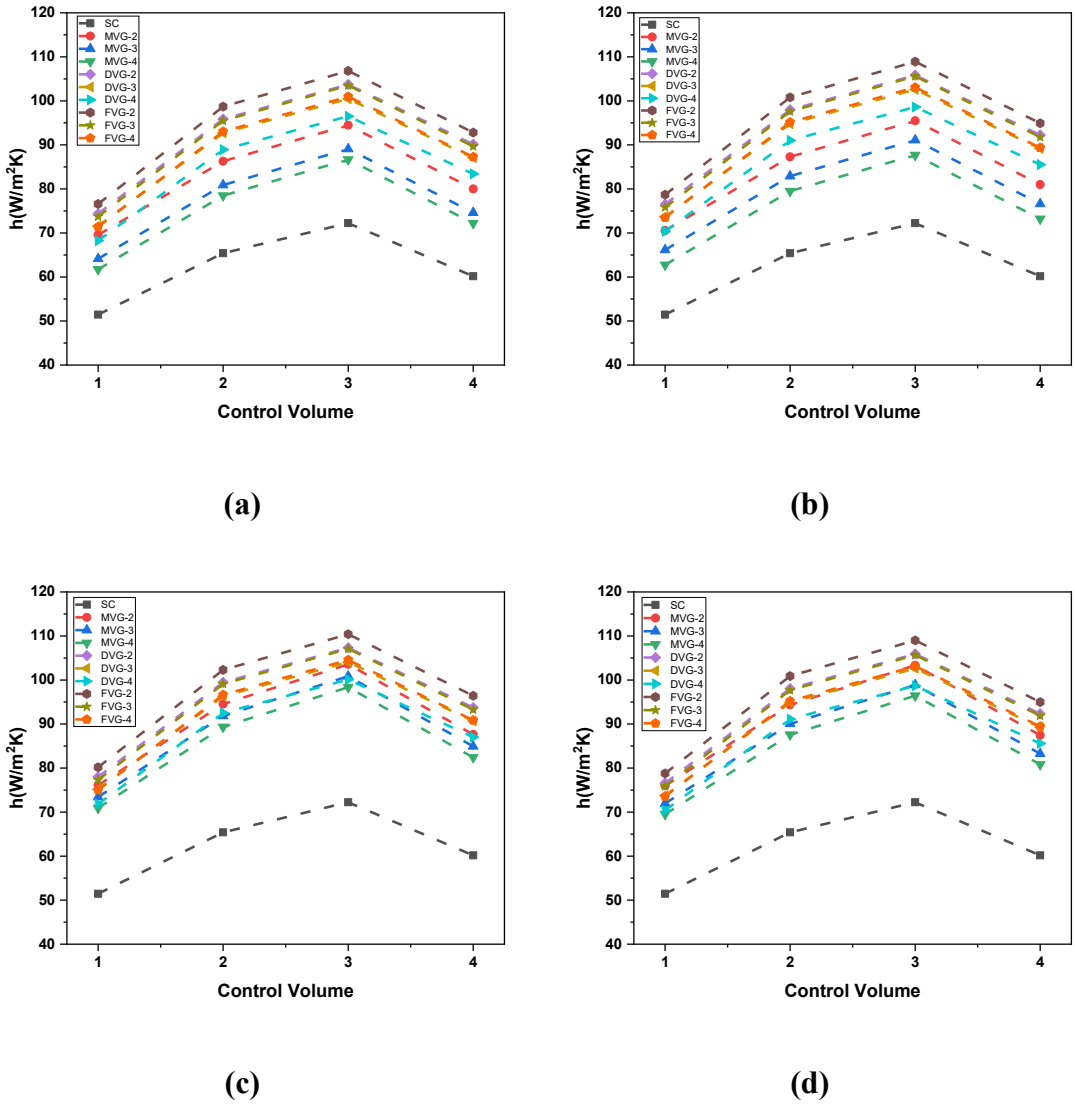

Fig. 3.6 Heat transfer coefficient with control volume for different VG shapes and D/H ratios at angles of inclination of (a) 30°, (b) 45°, (c) 60°, and (d) 90°

Further analysis depicts that the initial increase in the heat transfer coefficient with control volume number is attributed to the progressive development and intensification of secondary flow structures induced by the vortex generators. As the hot air flows downstream, these vortices fully form, efficiently disrupting the thermal boundary layer and generating significant turbulence. This enhances fluid mixing, transporting high-

momentum fluid from the core toward the walls and substantially boosting convective heat transfer. The subsequent decrease beyond the third control volume occurs due to vortex decay and dissipation downstream. Consequently, this leads to increased thermal resistance and a decline in the local heat transfer coefficient along the remaining length of the heat exchanger.

3.2.2 Effect of vortex generators on the pressure drops

Figs. 3.7 (a-d) show the pressure drops for different configurations along the length of the HX. The pressure drop in the heat exchanger is observed to be higher at lower D/H ratios due to the increased number of vortex generators within the flow domain. A lower D/H ratio implies that the spacing between consecutive vortex generators is reduced, leading to a greater number of flow obstructions along the channel. This intensified obstruction enhances flow resistance, causing a higher pressure loss. Additionally, the increased frequency of vortex shedding and secondary flow interactions leads to elevated turbulence levels and greater energy dissipation, further contributing to the rise in pressure drop. Moreover, excessive vortex interactions in tightly spaced configurations can induce flow recirculation zones, increasing overall flow resistance and pressure losses. The fishtail vortex generator exhibits the lowest pressure drop among the tested configurations due to its aerodynamic shape, which facilitates smoother airflow deflection with minimal abrupt separations. Unlike M-envelope and delta vortex generators, the fishtail design likely generates weaker trailing vortices, leading to a more streamlined flow pattern. This reduces flow separation and pressure drag, resulting in lower energy dissipation. Furthermore, the fishtail configuration may encourage a more gradual redistribution of flow momentum, preventing excessive turbulence generation while still promoting effective heat transfer enhancement.

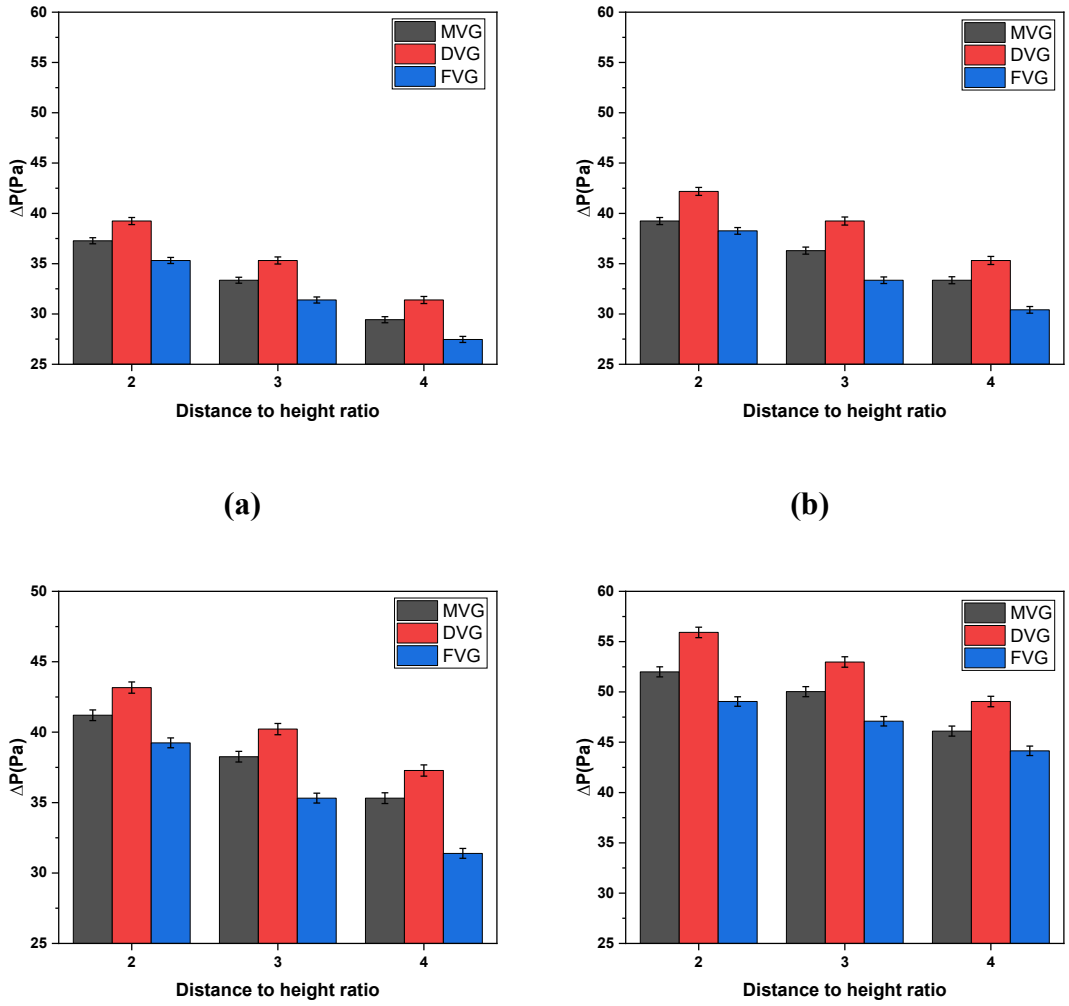

Fig. 3.7 Pressure drops for different VG shapes and D/H ratios at angle of inclination of (a) 30°, (b) 45°, (c) 60°, and (d) 90°

The highest pressure drop is observed when the vortex generators are inclined at 90°, which is attributed to the substantial obstruction posed by the incoming hot air stream. At this inclination, the vortex generators act as perpendicular barriers to the flow, causing significant flow separation and wake formation. This increased blockage effect leads to stronger vortex shedding, high turbulence intensity, and pronounced flow stagnation, all of which contribute to a considerable rise in pressure drop. Additionally, the abrupt deflection of the airflow at a steep inclination results in greater momentum losses and increased form drag, further elevating the pressure loss in the system.

3.2.3 Effect of vortex generators on thermal enhancement factors

Figs. 3.8 (a-d) show TEF for different configurations along the length of the HX. The increase in the thermal enhancement factor (TEF) with the D/H ratio can be attributed to the more favorable balance between heat transfer enhancement and pressure drop penalty at the larger spacing between vortex generators. As the D/H ratio increases, the interaction between consecutive vortices is optimized, reducing excessive flow disturbances and minimizing unnecessary energy dissipation. While the heat transfer coefficient may exhibit a gradual decline at higher D/H values due to weaker vortex interactions, the corresponding reduction in pressure drop leads to a lower friction factor. Since TEF is defined as a ratio that penalizes excessive pressure drop, the reduction in flow resistance at larger D/H ratios results in a net increase in TEF, making the enhancement technique more efficient.

The fishtail vortex generator (FVG) exhibiting the highest TEF value is primarily due to its superior aerodynamic design, which achieves a higher heat transfer enhancement with minimal flow resistance. The fishtail shape likely promotes the generation of stable, coherent vortices that persist over a longer streamwise distance, ensuring sustained convective heat transfer augmentation. Simultaneously, its streamlined configuration minimizes abrupt flow separations and recirculation zones, leading to a lower friction factor compared to M-envelope and delta-shaped vortex generators. This optimal balance between thermal augmentation and pressure drop reduction makes the FVG the most efficient configuration, as reflected in its highest TEF value.

The lowest TEF value at an inclination angle of 90° can be attributed to the excessive obstruction caused by the vortex generators, leading to a disproportionately high-pressure drop relative to the achieved heat transfer enhancement. At this inclination,

the vortex generators act as nearly perpendicular barriers to the incoming hot air stream, significantly disrupting the flow dynamics. While the presence of strong vortices at this angle enhances localized convective heat transfer, the induced pressure drop becomes excessively high due to increased frictional and form drag. The large-scale recirculation zones and intensified turbulence further contribute to energy dissipation, which negatively impacts the overall thermohydraulic performance.

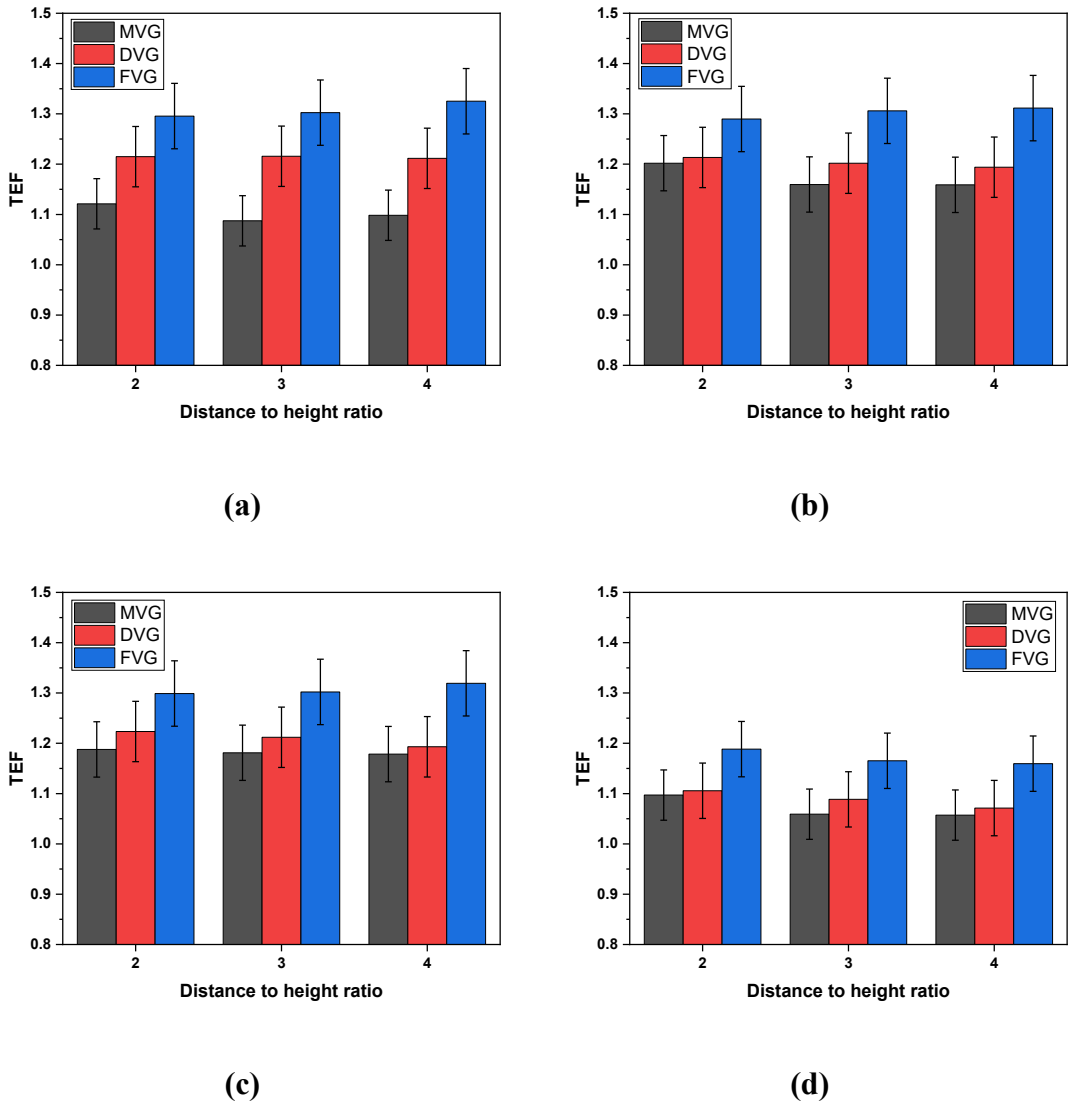

Fig. 3.8 Thermal enhancement factors for different VG shapes and D/H ratios at angle of inclination of (a) 30°, (b) 45°, (c) 60°, and (d) 90°

Consequently, despite a possible improvement in the heat transfer coefficient, the substantial increase in flow resistance leads to a sharp decline in the thermoelectric performance factor (TEF). Since TEF is a measure that integrates both heat transfer augmentation and pressure drop penalties, the severe aerodynamic resistance at 90° results in an unfavorable trade-off. The excessive pressure drop diminishes the net energy gain, making this configuration the least efficient in terms of overall performance. The quantitative evaluation of these effects, including variations in TEF, friction factor, and heat transfer coefficient, is systematically presented in Table 3.2 for comprehensive analysis.

Table 3.2: Percentage variation of different thermohydraulic parameters for different Vortex generator configurations with smooth channel as the reference

θ	D/H ratio	Average HTC			ΔP			TEF		
		MVG	DVG	FVG	MVG	DVG	FVG	MVG	DVG	FVG
30°	2	32.5	46.0	50.4	65.2	73.9	56.5	12.1	21.4	29.5
	3	23.8	41.1	45.3	47.8	56.5	39.1	8.7	21.5	30.2
	4	20	35.2	41.4	30.4	39.1	21.7	9.8	21.1	32.5
45°	2	44.5	49.4	53.7	73.9	86.9	69.5	20.1	21.3	28.9
	3	35.8	44.5	48.7	60.8	73.9	47.8	15.9	20.1	30.5
	4	32	38.6	44.8	47.8	56.5	34.7	15.8	19.4	31.1
60°	2	45.1	51.8	56.1	82.6	91.3	73.9	18.7	22.3	29.8
	3	40.8	46.9	51.1	69.5	78.2	56.5	18.1	21.1	30.2
	4	36.8	41.0	47.2	56.6	65.2	39.1	17.8	19.3	31.9
90°	2	44.8	49.5	53.9	130.4	147.8	117.3	9.7	10.5	18.8
	3	38.0	44.6	48.8	121.7	134.7	108.6	5.9	8.8	16.5
	4	34.1	38.7	44.9	104.3	117.3	95.6	5.7	7.1	15.9

3.2.4 Effect of vortex generators on TEG power output

Figs. 3.9 (a-d) show the average TEG power output for different configurations along the length of the HX. The observed decrease in TEG power output with increasing D/H ratio can be attributed to the corresponding reduction in the heat transfer coefficient. At lower D/H ratios, the closely spaced vortex generators induce stronger vortical structures, enhancing fluid mixing and increasing convective heat transfer rates at the hot-side surface of the heat exchanger. This leads to a higher outer surface temperature, thereby maximizing the temperature gradient across the thermoelectric generator. However, as the D/H ratio increases, the spacing between vortex generators grows larger, weakening vortex interactions and reducing convective augmentation. Consequently, the heat exchanger surface temperature declines, thereby diminishing the temperature difference available for thermoelectric power generation, leading to a drop in TEG power output.

The highest TEG power output observed for the heat exchanger equipped with fishtail vortex generators (FVG) can be explained by the superior thermal performance of this configuration. The fishtail shape promotes strong and persistent vortices, ensuring an effective enhancement of heat transfer while simultaneously maintaining a relatively lower pressure drop. This results in a higher surface temperature of the heat exchanger, leading to an increased temperature differential across the thermoelectric generator. Since TEG output is directly proportional to the temperature difference between its hot and cold sides, the improved convective heat transfer efficiency of FVG-equipped heat exchangers translates into superior TEG power generation compared to M-envelope and delta-shaped vortex generators.

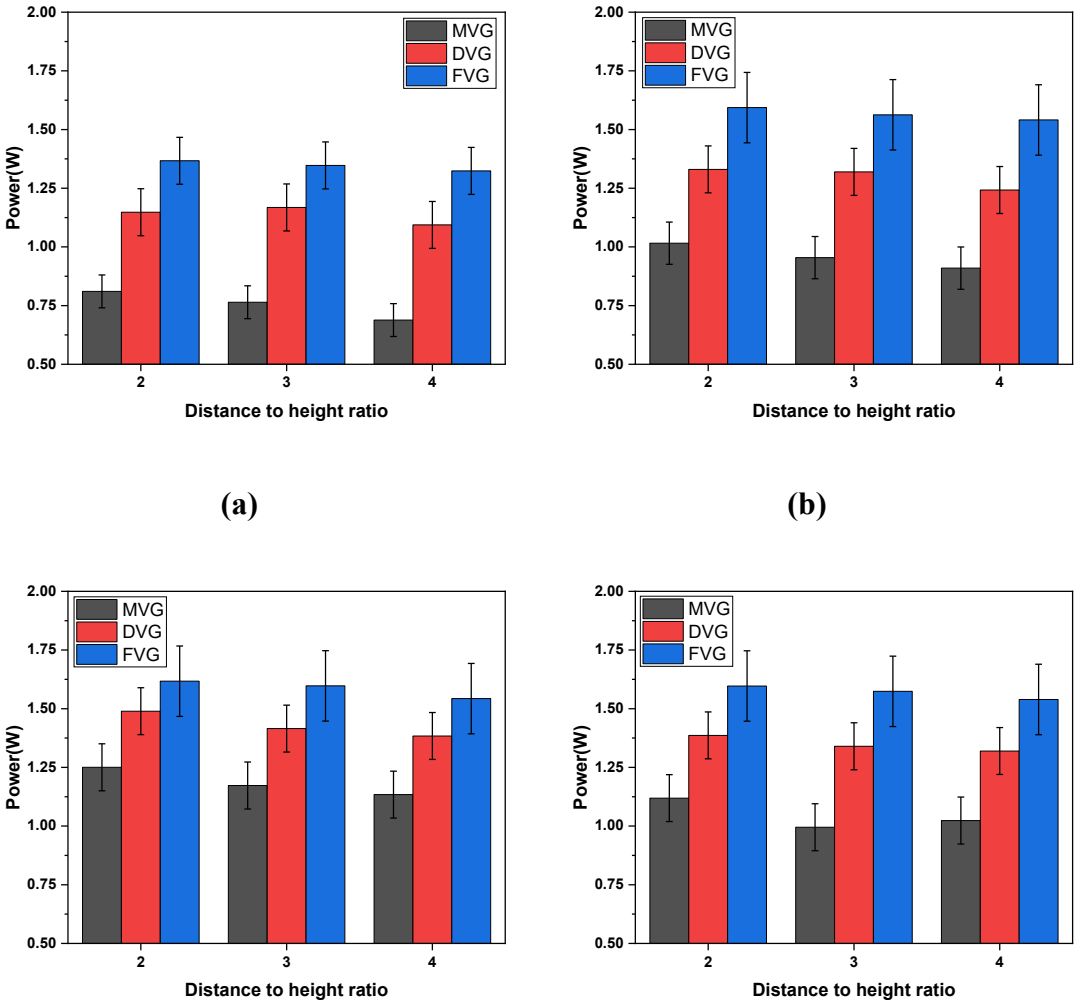

Fig. 3.9 TEG power output for VG shapes and D/H ratios at angle of inclination of (a) 30°, (b) 45°, (c) 60°, and (d) 90°

The trend of increasing TEG power output with an inclination angle up to 60°, followed by a decline at 90°, is governed by the interplay between heat transfer enhancement and flow resistance. At lower inclination angles, the vortex generators generate moderate yet effective vortices, improving convective heat transfer and raising the heat exchanger surface temperature, which in turn boosts TEG power. As the inclination reaches 60°, vortex strength and interaction reach an optimal state, maximizing heat transfer augmentation and, consequently, TEG power output. However, at 90°, the vortex generators act as significant obstructions to the airflow, causing

excessive pressure losses and flow stagnation, which disrupts efficient convective heat transfer. This leads to a reduction in the heat exchanger surface temperature, thereby diminishing the temperature gradient available for TEG power generation. Thus, the decrease in TEG power at 90° is primarily due to the adverse effects of increased flow resistance and disrupted thermal transport mechanisms.

3.3 Highlights

- Vortex generators create longitudinal vortices that enhance fluid mixing. This improves heat transfer by disrupting the boundary layer and bringing hotter fluid closer to the cooler surface. By improving mixing, VGs help achieve a more uniform temperature profile across surfaces, which is beneficial in heat exchangers.
- The maximum increment in heat transfer coefficients are 45.16%, 51.85%, and 56.18% for MVG, DVG, and FVG respectively at D/H=2 and θ=60°.
- The vortex generators come with a penalty in the form of increased pressure drop which is high at a lower D/H ratio and high inclination angle because of the increase in obstruction to hot air flow. The highest pressure drops obtained are 3.46Pa, 3.72Pa, and 3.27Pa for MVG, DVG, and FVG respectively at D/H=2 and θ=90°.
- The heat exchanger equipped with vortex generators gives a thermal enhancement factor greater than 1 which depicts that placement of VGs for waster heat recovery through TEG is successful.
- The TEG output improved due to higher surface temperature in channels equipped with VGs than the smooth channel, owing to better heat transfer. The highest average TEG power obtained is 1.62W.

- Vortex generators have the capacity to improve TEG performance as well as support in reducing the size of the waste heat recovery systems.

This page is left intentionally blank

Chapter 4

Dissimilar Material-based Multistage Thermoelectric Generator with Varying Leg Geometry

Overview: This chapter presents a modified thermoelectric generator (TEG) featuring a two-stage configuration with variable leg geometry and dissimilar thermoelectric materials. A comprehensive iterative model is developed to analyze its performance under varying operating conditions. The study examines the influence of row number, exhaust inlet temperature, and coolant flow on key performance parameters, including voltage, power output, conversion efficiency, and their normalized counterparts. To optimize thermal performance, a varying cross-section is employed on the cold side to induce a more pronounced temperature gradient compared to a uniform geometry. The objective is to identify the optimal configuration that maximizes the efficiency and output of the multistage variable-shape thermoelectric generator (MVS-TEG).

4.1 Mathematical Modeling of MVS-TEG

Fig. 4.1 shows the newly designed multistage-variable shape TEG (MVS-TEG) designed for the present study. The first stage is comprised of the constant cross-section while the preceding stage is a variable one. A varying cross-section is employed because it ensures a greater temperature gradient as compared to a constant cross-section on the cold side. Fig. 4.2 shows the schematic of the complete system comprising the parallel heat exchangers, the computational units, and the direction system used. The grey strips in between the flat and converging legs in figure 4.1 has been used to differentiate the different stages. Table 4.1 lists the thermoelectric properties of the MVS-TEG **(**Massetti

et al., 2021). Parallel flow is preferred per the findings of Bejan et al. (2014). The system consists of a heat exchanger at the hot side, then the MVS TEG, and eventually the coolant channel at the cold side of the generator. When exhaust gas flows through the exhaust heat exchanger, the TEG experiences heat input at the hot side and cold at the cold side due to coolant. A potential difference due to temperature difference is produced. With time, the temperatures at the terminals achieve a steady state, and a steady flow of current is also reached.

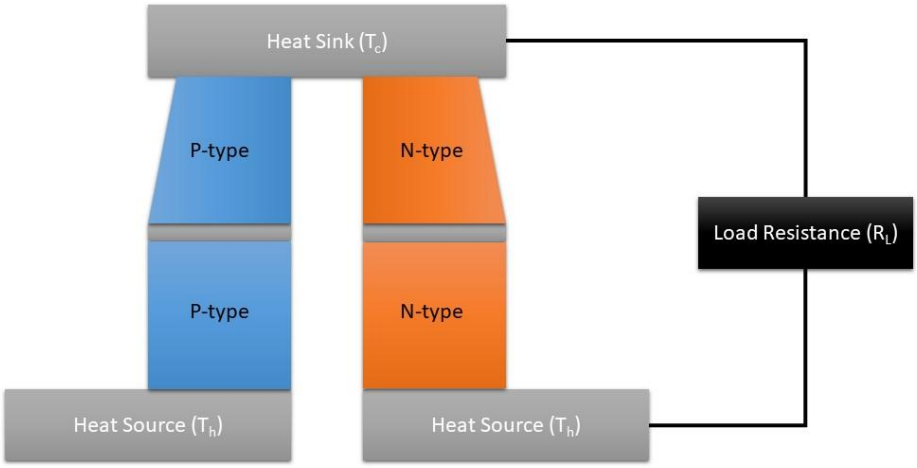

Fig. 4.1 Schematic Diagram of MVS-TEG

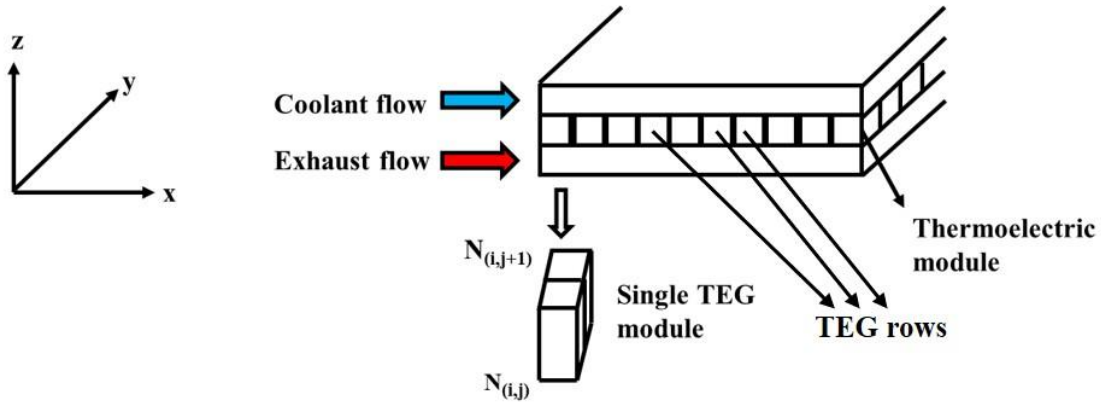

Fig. 4.2 Schematic Diagram of fluid flow and TEG system

The MVS-TEG is modeled on various energy conservation assumptions. Firstly, heat transfer attains a steady state across the TEG, which implies that the heat gained by the hot side of the TEG from the exhaust and the heat lost by the cold side of the TEG to the coolant is the same, respectively. Radiative heat transfer of any kind and heat transfer in the ducts are also neglected. The contact resistances between fluids and heat source and sink are neglected. The Thomson effect is disregarded because of the constant transport properties (α, ρ, k). The boundary conditions for the TEG are $x = 0 \rightarrow T = T_h$ and $x = h \rightarrow T = T_c$.

Table 4.1: Thermoelectric characteristics of p-type and n-type TEG materials (Massetti et al., 2021b)

TEG Material	Thermal conductivity (W/m K)	Seebeck coefficient (μV/K)	Electrical Conductivity (S/cm)	Figure of Merit (ZT)
P-type				
PEDOT/Bi_2Te_3	0.7	165	500	0.58
PEDOT:PSS	0.33	73	880	0.42
N-type				
Poly [Kx(Ni-ett)] (1)	0.31	-151.7	64	0.2
Poly [Kx(Ni-ett)] (2)	0.84	-150	310	0.32

Based on the above assumptions, the governing equations for the heat transfer across the MVS-TEG are as follows (Sun et al., 2014):

$$Q_{i,h} = N_y \left[\alpha_{pn} I T_{i,h} + k_{pn}\left(T_{i,h} - T_{i,m}\right) - \frac{I^2 R_{pn}}{2} \right] \tag{4.1}$$

$$Q_{i,m} = N_y \left[\alpha_{pn} I T_{i,m} + k_{pn}\left(T_{i,h} - T_{i,m}\right) + \frac{I^2 R_{pn}}{2} \right] \tag{4.2}$$

$$Q_{i,m} = N_y \left[\alpha_{pn} I T_{i,m} + k_{pn}\left(T_{i,m} - T_{i,c}\right) - \frac{I^2 R_{pn}(z)}{2} \right] \tag{4.3}$$

$$Q_{i,c} = N_y \left[\alpha_{pn} I T_{i,c} + k_{pn}\left(T_{i,m} - T_{i,c}\right) - \frac{I^2 R_{pn}(z)}{2} \right] \tag{4.4}$$

Where N_y, I, and T represent the number of legs along the y-direction, steady-state current, and temperatures respectively. The above equations consider the Peltier effect, the Joule effect, and thermal conduction losses. The different thermoelectrical properties are as follows (Sahoo and Karana, 2020):

$$\alpha_{pn} = \alpha_p - \alpha_n \tag{4.5}$$

$$k_{pn} = \frac{lb(\beta_p - \beta_n)}{h} \tag{4.6}$$

$$R_{pn} = \frac{h(\rho_p - \rho_n)}{lb} \tag{4.7}$$

Where α, k, R, l, b, h, and ρ denotes the Seebeck coefficient, thermal conductivity, electrical resistance, length, breadth, and height of the TEG leg, and resistivity of the TEG material respectively. The thermoelectric module is composed of several TEGs which are connected in series electrically and parallel thermally. For analysis purposes, the module is divided into N_x and N_y calculation units along the x-axis and y-axis respectively. Considering the variable cross-section of the second stage, we have:

$$A(z) = A_0 \left(\frac{h - {}^{z}/_{2}}{h} \right) \tag{4.8}$$

Where areas $A_0 = lb$ and $A(z) = l(z)b$. Thus, we have:

$$l(z) = l\left(\frac{h - {}^{z}/_{2}}{h}\right) \tag{4.9}$$

Based on the above geometry of the latter stage, the thermoelectric property varies as follows:

$$k_{pn}(z) = \frac{l(z)b(\beta_p - \beta_n)}{h} \tag{4.10}$$

$$R_{pn}(z) = \frac{h(\rho_p - \rho_n)}{l(z)b} \tag{4.11}$$

Table 4.2 enlists the fluid flow and thermophysical properties of the exhaust gas and coolant **(**Karana and Sahoo, 2018**)**. The heat exchange between the different fluids follows Newton's law of cooling:

$$Q_{i,h} = N_y h_{ex} A_{TEG,h}\left(T_{ex,avg} - T_{i,h}\right) \tag{4.12}$$

$$Q_{i,c} = N_y h_{co} A_{TEG,c}\left(T_{i,c} - T_{co,avg}\right) \tag{4.13}$$

Table 4.2: Thermal and flow properties of exhaust gas and coolant

Property	Value
Mass flow rate of exhaust gas	0.03kg/s
Specific heat of exhaust gas	1020J/kgK
Exhaust gas heat transfer coefficient	80W/m^2 K
Specific Heat of coolant	4180J/kgK

Also, assuming smooth walls of the coolant channel, the suitable Nusselt number and friction factor correlation used for the study are as follows (Bergman et al., 2011):

$$Nu = \frac{(f/8)(Re - 1000)Pr}{1 + 12.7(f/8)^{1/2}(Pr^{2/3} - 1)} \tag{4.14}$$

$$f = (0.79 \ln Re - 1.64)^{-2} \tag{4.15}$$

When the system attains a steady state, the heat lost by exhaust gas equals the heat gained on the hot side, and the heat lost by the cold side equals the heat gained by the coolant.

$$Q_{i,h} = \dot{m}_{ex} c_{p,ex} (T_{i+1,ex} - T_{i,ex}) \tag{4.16}$$

$$Q_{i,c} = \dot{m}_{co} c_{p,co} (T_{i,co} - T_{i+1,co}) \tag{4.17}$$

As the exhaust gas and coolant flow across the module, the temperature gradient causes the production of potential across the two sides of the TEG. The potential developed is a function of the thermoelectric property and the temperature difference between the hot and cold sides, also known as the Seebeck effect:

$$V_i = N_y \alpha_{pn} \left(T_{i,h} - T_{i,c}\right) \tag{4.18}$$

Hence, the total output voltage is given as:

$$V_{Total} = N_y \alpha_{pn} \sum_{1}^{N_x} \left(T_{i,h} - T_{i,c}\right) \tag{4.19}$$

The combined resistance offered by the TEG and resistance load gives the current I_c with the help of Ohm's law.

$$R_{eq} = N_x N_y R_{pn} + R_L \tag{4.20}$$

$$I_c = V_{Total} / R_{eq} \tag{4.21}$$

Another critical parameter, demonstrating the utility of the TEG is the power produced, which can be calculated as follows:

$$P = I_c^2 R_L \tag{4.22}$$

To understand the benefit of the TEG, the output relative to the heat input is measured, which is commonly known as conversion efficiency:

$$\eta_{conv} = \frac{P}{\sum_i^{N_x}(Q_{i,h})} \tag{4.23}$$

Now, the maximum current occurs when the load resistance, $R_L = 0$ (Sahoo and Karana, 2020). Thus, the expression for maximum parameters like output voltage and power are:

$$V_{max} = \alpha_{pn}(T_h - T_c) \tag{4.24}$$

$$Power_{max} = \alpha_{pn}^2(T_h - T_c)^2/4R_{TEG} \tag{4.25}$$

However, the maximum efficiency of the TEG is given by:

$$\eta_{max} = \frac{\left(1 - {}^{T_c}/_{T_h}\right)\sqrt{1+ZT} - 1}{\sqrt{1+ZT} - {}^{T_c}/_{T_h}} \tag{4.26}$$

The second law efficiency of the device is also ascertained to quantify its exergetic performance with the help of the following equations:

$$\eta_{II} = \frac{Power}{Power + I_{rr}} \tag{4.27}$$

$$I_{rr} = T_0 S_{gen} \tag{4.28}$$

$$S_{gen} = \frac{Q_h}{T_h} - \frac{Q_c}{T_c} \tag{4.29}$$

Where I_{rr} is the irreversibility associated with the heat transfer across the TEG while S_{gen} is the entropy generated at the same condition of flow. For the present theoretical research, the following nomenclature has been employed as shown in Table 4.3. An iterative approach is developed for steady-state calculations with the help of Energy Equation Solver (EES) software. The algorithm utilized is shown in Fig. 4.3. The material poly[Kx(Ni-ett)](1) is poly(Nickel 1,1,2,2-ethylenetetrathiolate) while poly[Kx(Ni-ett)](2) is electrochemically treated poly(Nickel 1,1,2,2-ethylenetetrathiolate).

Table 4.3: Nomenclature of the generators under study

Combination no.	P-type material	N-type material
MVS TEG 1	PEDOT/Bi_2Te_3	poly[Kx(Ni-ett)] (1)
MVS TEG 2	PEDOT/Bi_2Te_3	poly[Kx(Ni-ett)] (2)
MVS TEG 3	PEDOT:PSS	poly[Kx(Ni-ett)] (1)
MVS TEG 4	PEDOT:PSS	poly[Kx(Ni-ett)] (2)

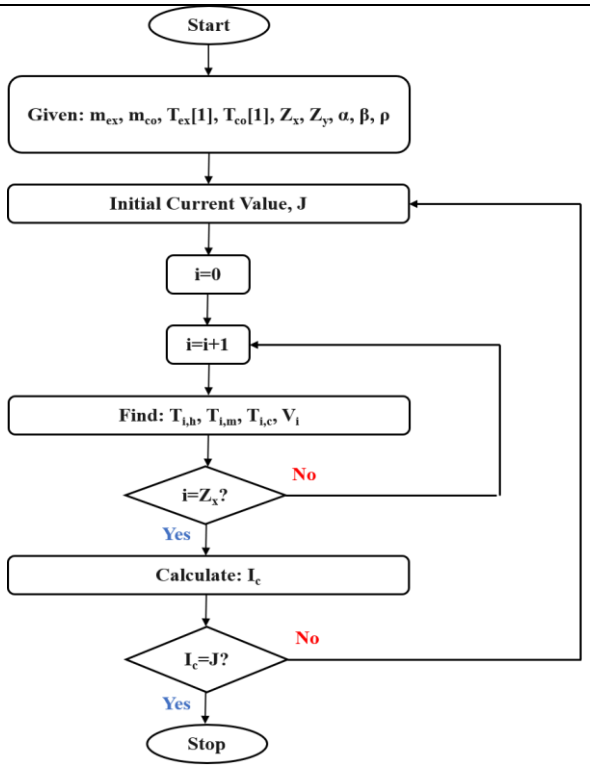

Fig. 4.3 Iterative approach employed in the current study

The validation of the proposed new configuration has been done with the published data (Karana and Sahoo, 2019), and shown in Fig. 4.4. The exhaust and coolant temperatures are found to be following a similar trend with some deviation that occurs due to different initial conditions. The average error in prediction of ΔT across the TEG is 1.54%.

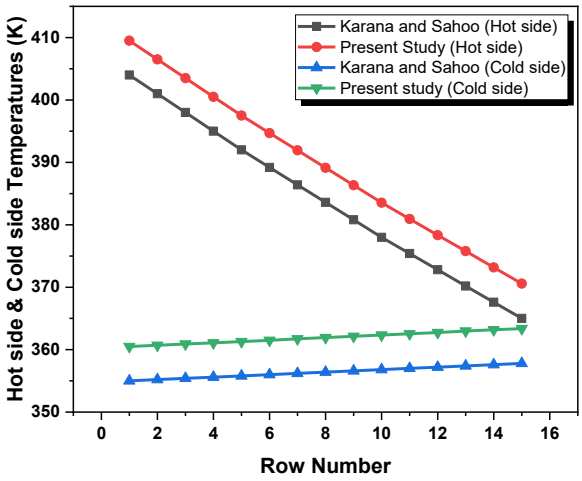

Fig. 4.4 Validation of the present study with the published study

4.2 Results and Discussion

4.2.1 Variation in TEG performance with number of rows

Variation of voltage produced for an exhaust flow rate of 0.03kg/s and exhaust inlet temperature condition of 500K with the row number for different MVS-TEG combinations is shown in Fig. 4.5. From the result obtained, it can be observed that voltage increases as the row number increases. However, the rate of increase in the voltage produced keeps on decreasing in the direction of the flow. It is because as the exhaust and coolant advance their flow across the MVS-TEG system, the temperature difference between the hot side and cold side of the MVS-TEG decreases. This fall in the temperature difference between the two sides of the MVS-TEG is because as both fluids flow, the exhaust loses its heat content while the coolant is heated along the flow. This decreases the exhaust temperature while the coolant temperature rises. Now, the main cause behind the development of the voltage is the existence of the temperature gradient. As this gradient decreases along the flow, this results in lower voltage production of the TEG module.

From the outcome, it can also be deduced that the highest voltage is produced by MVS TEG-2 followed by MVS TEG-1, MVS TEG-4, and MVS TEG-3. The voltage increases by 8.405, 8.505, 8.316, and 8.373 times for MVS TEG-1, MVS TEG-2, MVS TEG-3, and MVS TEG-4 respectively of the voltage produced by the generators in the first row. Also, a critical point to be noted is that an optimum value of the TEG is observed as 19 for MVS TEG-1, MVS TEG-3, and MVS TEG-4, and 18 for MVS TEG-2. This helps us in defining the maximum number of useful rows for the application.

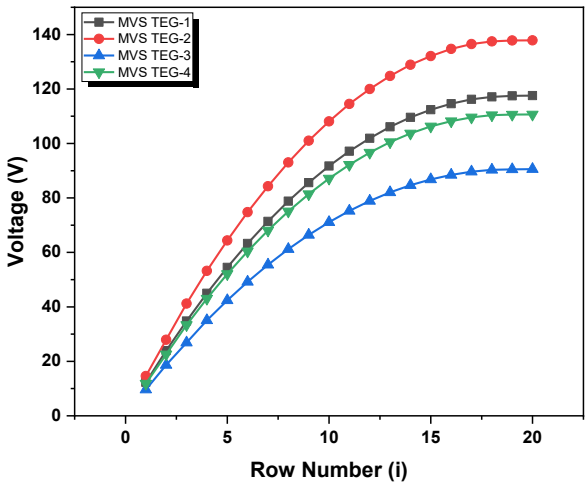

Fig. 4.5 Voltage v/s Row number

Fig. 4.6 shows the effect of row number on the power developed by the different MVS-TEG systems for 0.03kg/s exhaust flow rate and 500K exhaust inlet temperature. The power developed increases rapidly with the row number. However, this increment is soon retarded and a lower power generation rate is seen by further increasing the generator's row. This decrement is such that after a particular row, the MVS-TEG produces lesser power in comparison with the row just before it.

This is because power generation is highly dependent on the temperatures of the exhaust and coolant on the hot and cold side of the MVS-TEG respectively. The temperature gradient causes the motion of electrons and holes throughout the TEG system

resulting in the Seebeck effect, Joule's effect, and thermal conduction of heat. The result is the generation of a certain amount of power across the resistance load. However, on adding a greater number of rows beyond a certain limit, the power generation falls. This gives the optimum row number that must be utilized and helps to determine the nominal size of the module. Also, it is observed that the maximum power is generated by MVS TEG-2, followed by MVS TEG-1, MVS TEG-4, and MVS TEG-3. The increment is 8.406, 8.508, 8.313, and 8.37 folds for MVS TEG-1, MVS TEG-2, MVS TEG-3, and MVS TEG-4 respectively.

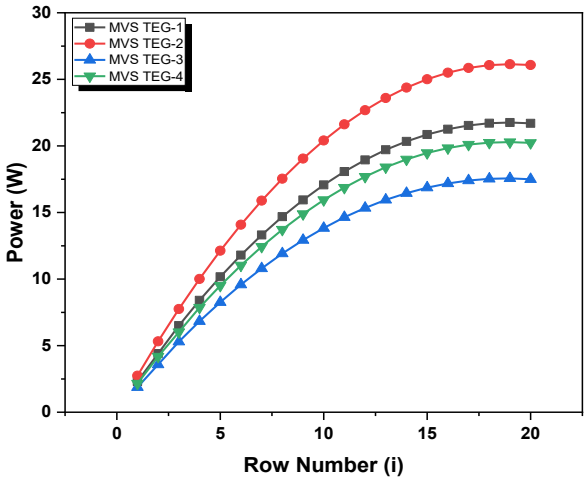

Fig. 4.6 Power v/s Row number

The variation of conversion of different MVS-TEG for the exhaust flow rate and inlet temperature for the coolant flow rate of 0.03kg/s and inlet temperature of 298K is shown in Fig. 4.7. The conversion efficiency of all the MVS-TEG is observed to decrease with the row number. This may be due to lower power generation relative to the heat supplied to the hot side of the MVS-TEG. As the row number is increased, it is seen that the exhaust temperature decreases which results in lower heat supplied. However, simultaneously, the power generation decreases due to lower temperatures along the flow direction. Also, different thermoelectrical properties result in varying performances of the

generators. MVSTEG-2 was able to convert maximum heat into power among the different MVS-TEGs considered in the theoretical study. The conversion efficiency is found to be lower for the subsequent generators in MVS TEG-1, MVS TEG-4, and MVS TEG-3 order. However, the parameter is found to fall by 50.32%, 49.86%, 50.76%, and 50.47% for MVS TEG-1, MVS TEG-2, MVS TEG-3, and MVS TEG-4. Thus, it can be remarked that the conversion efficiency falls by almost half for all the MVS-TEG. Also, MVS TEG-2 (p-type: PEDOT:Bi_2Te_3, n-type: poly[Kx(Ni-ett)](2)) not only exhibits the maximum conversion efficiency but also it displays the least decrement in it.

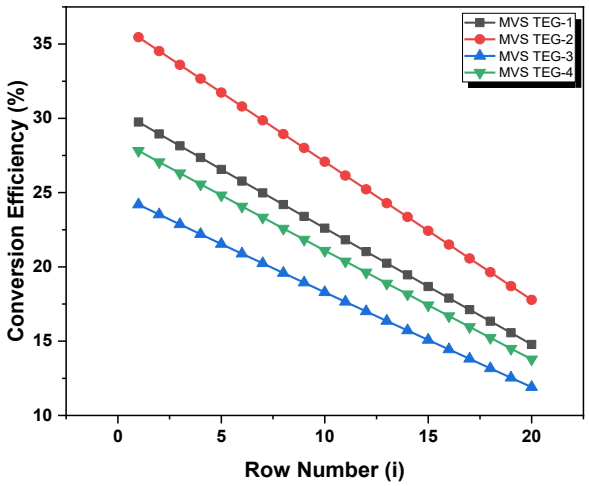

Fig. 4.7 Conversion efficiency v/s Row number

The second law efficiency of any device gives its exergetic performance concerning the different input variables. Fig. 4.8 shows the variation of the second law efficiency of different MVS-TEG with TEG unit row numbers for an exhaust flow rate of 0.03kg/s and 500K exhaust inlet temperature. The second law efficiency which is a measure of the irreversibility of the generator falls in a slightly non-linear fashion. This shows that the irreversibility increases along the exhaust flow direction. This is because as the row number is increased the rate of entropy generation increases because of more heat transfer across the system. The second law of efficiency incorporates the power

produced, heat transfers at both sides of the MVS-TEG, and their respective junction temperature. The second law efficiency decreases as the irreversibility increases due to a lower temperature gradient as the exhaust loses its heat content while the coolant gains heat from the generator.

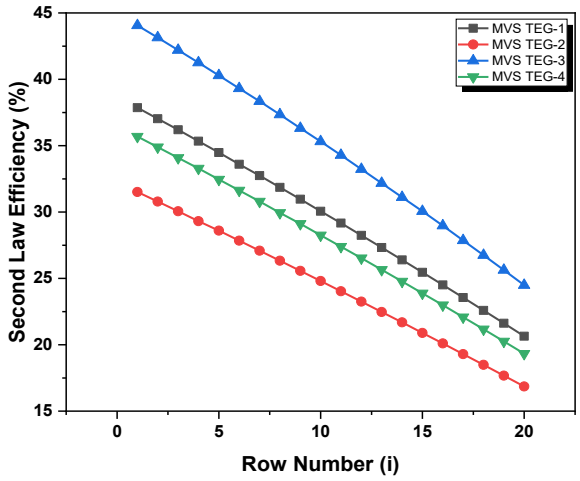

Fig. 4.8 Second law efficiency v/s Row number

Quantitatively, the second law efficiency decreases by 45.72%, 46.78%, 44.76%, and 46.1% for MVS TEG-1, MVS TEG-2, MVS TEG-3, and MVS TEG-4 respectively. MVS TEG-3 exhibits the maximum parameter value throughout while MVS TEG-2 shows the least. MVS TEG-1 and MVS TEG-2 display intermediate performance. However, it is observed that MVS TEG-3 exhibited the best performance parameter over other generators concerning the input variables and hence, this TEG is appreciated over others.

Besides output performance parameters (voltage, power, and conversion efficiency), it is important to ascertain how the generator performed relative to its maximum performance. It helps to find out how much the device has scope to improve. For this, normalized parameters become very crucial to calculate. Fig. 4.9 shows the normalized voltage variation with the row number for 0.03kg/s exhaust flow rate and

500K exhaust inlet temperature. The parameter decreases gradually till the second-row number for all generators after which it falls linearly. This decrement implies that all the MVS-TEGs have a greater potential for voltage generation at higher row numbers since the later TEG rows operate under lower hot side temperatures and higher coolant temperatures. It happens because of the decrement in temperature gradient across every row. At higher row numbers, a lower temperature gradient results in the above-mentioned decrement.

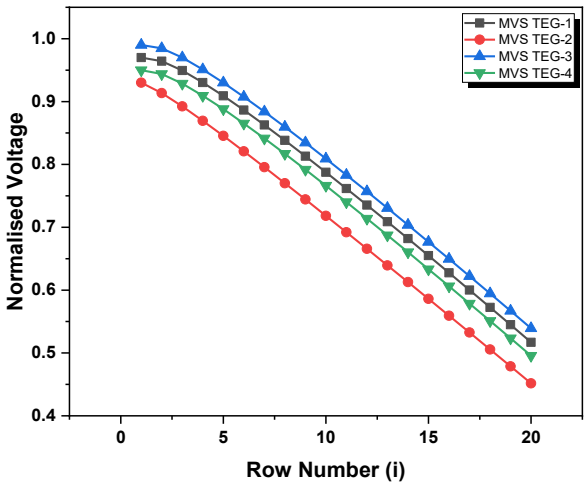

Fig. 4.9 Normalized voltage v/s Row number

The results exhibit that MVS TEG-3 (p-type: PEDOT/PSS, n-type: poly[Kx(Ni-ett)] (1)) displays the best overall performance in voltage generation as it has the highest parameter value. Furthermore, the normalized voltage decreases by 46.7%, 51.4%, 45,5%, and 47.8% for MVS TEG 1, 2, 3, and 4 respectively.

The effect of row number on the normalized power is shown in Fig. 4.10. Normalized power slopes downward slowly until the second row after which it reduces close to half of its initial value for all the MVS-TEG. Even though the power developed was observed to increase as shown in Fig. 4, when compared to the maximum power

output, it decreases. This implies that in comparison to maximum power, actual power produced decreases with row number.

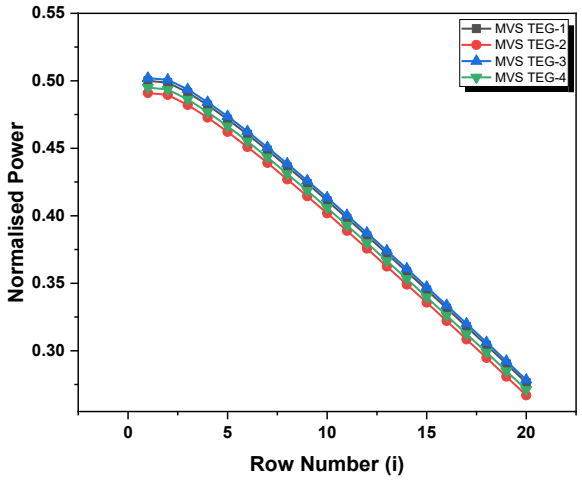

Fig. 4.10 Normalized Power v/s Row number

This trend is also observed to follow the results of the power versus row number where the power output is in the following order: MVS TEG-3, MVS TEG-1, MVS TEG-4, and MVS TEG-2. The normalized power decreases by 44.72%, 45.61%, 44.52, and 45.23% for MVS TEG-1, MVS TEG-2, MVS TEG-3, and MVS TEG-4 respectively. Normalized power values of the generators lie very close meaning that with the variation in row number under the same boundary and initial conditions, the generator gives similar normalized performance quantitatively.

On drawing a comparison of the normalized conversion efficiency of the different MVS-TEGs against row number, it is observed that the parameter decreases, signifying that the generators could have converted the heat more efficiently along the flow. This effect is made known in Fig. 4.11. The maximum conversion efficiency is the function of the Figure of merit (Z) and means temperature or dimensionless Figure of merit (ZT) in general. However, conversion efficiency depends on the actual performance of the generators governed exclusively by temperature. Thus, as the difference between the hot

side and cold side of the MVS-TEG decreases, conversion efficiency decreases. A point worth noting here is the decrement in the normalized conversion efficiency. The reason is that the decrement in conversion efficiency is more pronounced than its maximum counterpart. The constraint value decreases by 51.98%, 49.86%, 49.94%, and 55.42% for MVS TEG-1, MVS TEG-2, MVS TEG-3, and MVS TEG-4 respectively.

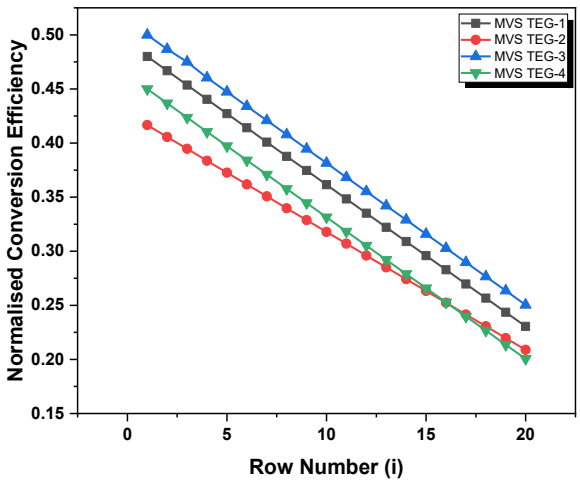

Fig. 4.11 Normalized conversion efficiency v/s Row number

Thus, the best action is exhibited by MVS TEG-3, followed by MVS TEG-1, MVS TEG-4, and MVS TEG-2. However, MVS TEG-2 (p-type: PEDOT/Bi_2Te_3, n-type: poly[Kx(Ni-ett)] (2)) performs better than MVS TEG-4(p-type: PEDOT:PSS, n-type: poly[Kx(Ni-ett)] (2)) for row number 17 and above.

4.2.2 Variation in TEG performance with exhaust inlet temperature

Fig. 4.12 shows the variation of voltage concerning the exhaust inlet temperature. The exhaust inlet temperature plays an important role in the MVS-TEG performance as it alters the end temperatures of the generators and hence the output. With the increase in exhaust temperature, the voltage produced by the MVS-TEG increases. It happens because the overall heat transfer rate increases which helps in creating higher temperature gradients along the flow. Maximum voltage is produced by MVS TEG-2, followed by

MVS TEG-1, MVS TEG-4, and MVS TEG-3. The voltage developed rises by 54%, 56.5%, 57.4%, and 58.9% for MVS TEG-1, MVS TEG-2, MVS TEG-3, and MVS TEG-4 respectively when the exhaust inlet temperature variation is studied from 450K to 545K. Overall, exhaust temperature increment raises the voltage performance. However, MVS TEG-2 has the maximum voltage because of the highest thermoelectric properties of p-type PEDOT/Bi_2Te_3 and n-type poly[Kx(Ni-ett)] (2).

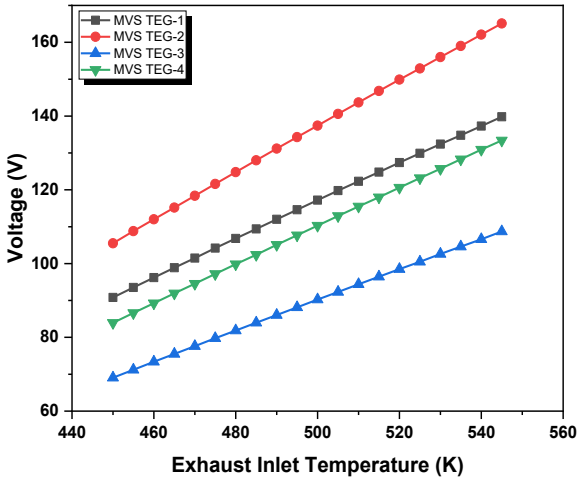

Fig. 4.12 Voltage v/s Exhaust inlet temperature

The power developed by the generators increases as the exhaust temperature is increased (Fig. 4.13). With higher temperature as the initial condition, the generators capture to work in a higher temperature zone. This enhances the Seebeck effect which is responsible for voltage and power generation. Not only does Seebeck power increase but also the heat conducted across the MVS-TEG rises which results in more heat loss due to the negative impact of electron and hole movement. However, fortunately, the Seebeck effect overwhelms the other performance-hampering traits of the material due to improved thermoelectric properties and Figures of merit. The tapering and multi-staging effect further enhance this action. Talking of the quantitative performance, MVS TEG-2 (p-type: PEDOT:Bi_2Te_3, n-type: poly[Kx(Ni-ett)] (2)) produces maximum power while

MVS TEG-3 (p-type: PEDOT/PSS, n-type: poly[Kx(Ni-ett)] (1)) produces the least. The increments in power development with the exhaust temperature at the inlet for 0.03kg/s exhaust mass flow rate are 53%, 55.5%, 56.3%, and 57.9% for MVS TEG-1, MVS TEG-2, MVS TEG-3, and MVS TEG-4 respectively.

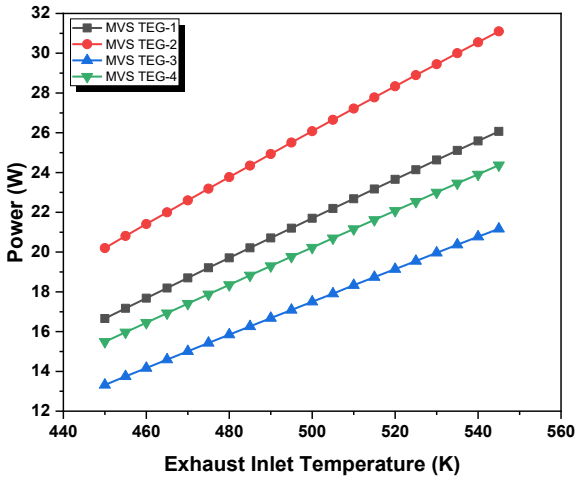

Fig. 4.13 Power v/s Exhaust inlet temperature

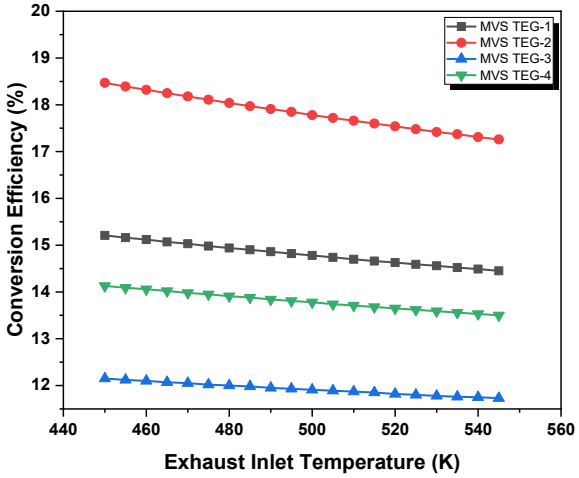

Fig. 4.14 Conversion efficiency v/s Exhaust inlet temperature

Fig. 4.14 shows the effect of exhaust inlet temperature on the conversion efficiency for 0.03Kg/s exhaust and coolant flow rate for exhaust temperature variation from 450K to 545K. With the temperature increase, the conversion efficiency decreases

because the increment in power generation is overpowered by enhanced heat transfer. The thermoelectric conversion efficiency decreases by 5%, 6.55% 3.46%, and 4.46% for MVS TEG-1, MVS TEG-2, MVS TEG-3, and MVS TEG-4 respectively. Thus, the employment of multiple-stage and variable cross-sections with novel materials not only helps to lower the efficiency losses but also helps achieve high values that have not been seen in conventional TEG with single-leg material of bismuth telluride. Therefore, the use of dissimilar materials with suitable characteristics is encouraged in the present study.

The effect of exhaust inlet temperature on the second law efficiency for different MVS-TEG at an exhaust flow rate of 0.03kg/s is negligible as the heat transfer rates vary per the temperatures at the generator ends. This is exhibited in Fig. 4.15. Maximum decrement is exhibited by MVS TEG-3 even though it inherits the highest second-law efficiency throughout the temperature range. However, the second law efficiency falls by 3.34%, 1.98%, 4.75%, and 2.87% for MVS TEG-1, MVS TEG-2, MVS TEG-3, and MVS TEG-4 respectively.

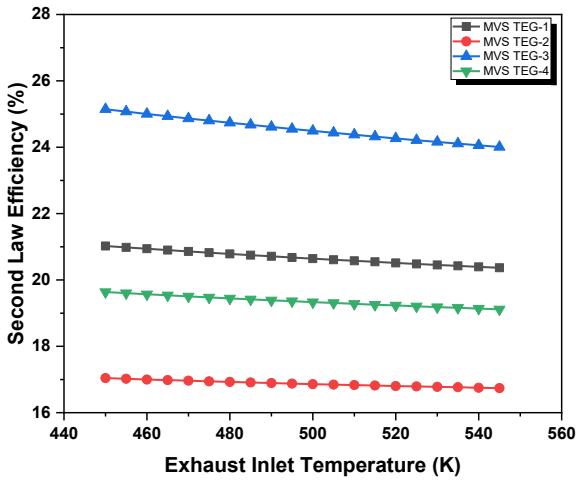

Fig. 4.15 Second law efficiency v/s Exhaust inlet temperature

However, the significant gap between individual second law efficiencies occurs due to distinct Seebeck coefficient, electrical conductivity, and thermal conductivity.

Overall, the effect of exhaust temperature is more noticeable over voltage and power while other factors are trivially affected. The decrease in normalized voltage with exhaust temperature for the previously mentioned inlet and initial conditions is displayed in Fig. 4.16. Contrary to other outputs subjected to similar conditions, the normalized voltage is very least affected by the change in exhaust inlet temperature. This means that the voltage developed and the maximum voltage run together throughout the temperature variation. It happens because as exhaust inlet temperature is increased, the maximum voltage that can be produced overpowers the actual voltage produced. The generators exhibit maximum normalized voltage at the minimum exhaust temperature. The parameter value decreases by 0.2%, 0.3%, 0.2%, and 0.2% respectively for MVS TEG-1, MVS TEG-2, MVS TEG-3, and MVS TEG-4.

The variation of the normalized power for different exhaust inlet temperatures is shown in Fig. 4.17 for different MVS-TEGs. It is observed that the normalized power decreases with the increase in exhaust inlet temperature. The reason is the falling rate of power generation relative to maximum power because of improved hot side temperature. The parameter value decreases by 0.19%, 0.26%, 0.15%, and 0.19% for MVS TEG-1, MVS TEG-2, MVS TEG-3, and MVS TEG-4 respectively under the exhaust flow rate of 0.03kg/s. However, MVS TEG-3 exhibits better performance than MVS TEG-1 for exhaust inlet temperatures of 530K and above. Also, MVS TEG-4 (p-type: PEDOT:PSS, n-type: poly[Kx(Ni-ett)] (2)) performs second to MVS TEG-2 (p-type: PEDOT/Bi_2Te_3, n-type: poly[Kx(Ni-ett)] (2)) up to 545K, though it appears that it may provide better results than MVS TEG-2 above this temperature.

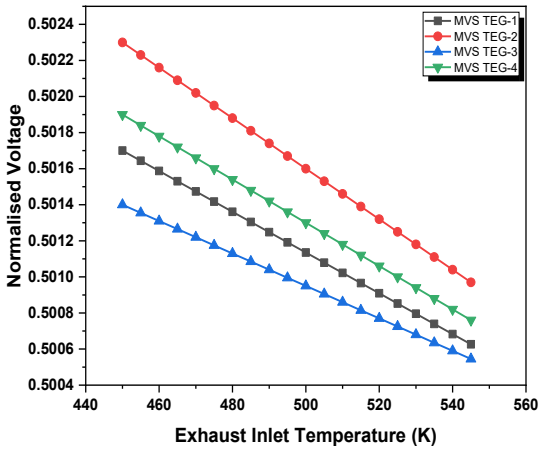

Fig. 4.16 Normalized voltage v/s Exhaust inlet temperature

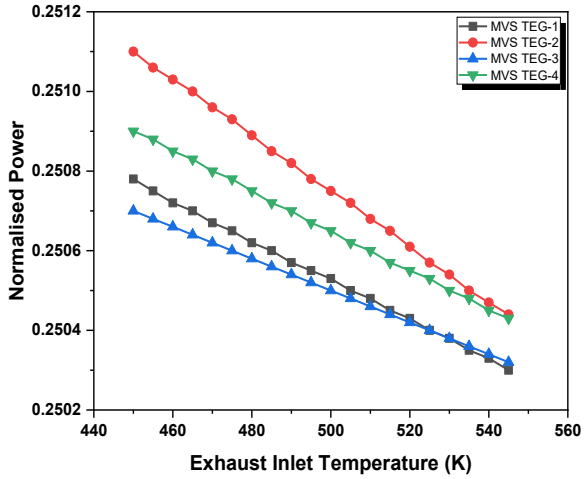

Fig. 4.17 Normalized Power v/s Exhaust inlet temperature

The effect of exhaust inlet temperature on the normalized parameter of conversion efficiency is depicted in Fig. 4.18 for the exhaust flow rate of 0.03kg/s. The normalized conversion efficiency falls as the exhaust inlet temperature rises. There is a negligible fall in the Parameter value which shows its weak reliance on the input variable under study. The normalized conversion efficiency decreases by 0.2%, 0.27%, 0.16%, and 0.2% for MVS TEG-1, MVS TEG-2, MVS TEG-3, and MVS TEG-4 respectively.

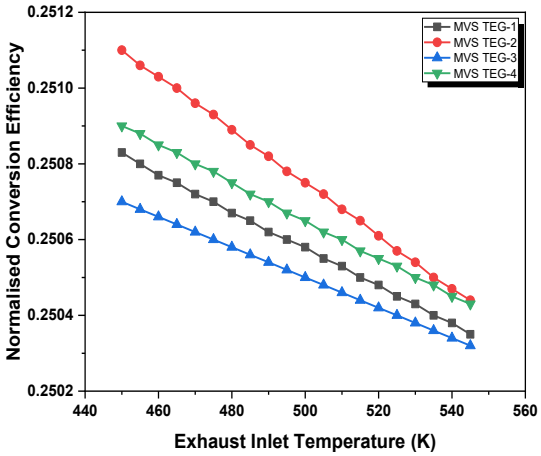

Fig. 4.18 Normalized conversion efficiency v/s Exhaust inlet temperature

However, a close observation would tell us that the MVS TEG-2 and MVS TEG-4 perform better for all the normalized parameters when the exhaust inlet temperature is varied. Also, the normalized parameters appear to be negligibly influenced by the variation in exhaust temperature.

4.2.3 Variation in TEG performance with the coolant flow rate

The variation of voltage produced with the coolant flow rate is shown in Fig. 4.19. With the increase in coolant flow rate, the heat transfer rate at the cold side of the MVS-TEG increases. This, coupled with muti-staging and tapering cross-section of the second stage enhances the cooling rate, which eventually results in increased voltage production. Faster coolant flow carries away more heat and thus higher temperature gradient results in more voltage production. MVS TEG-2 produces the highest voltage. MVS TEG-1, MVS TEG-4, and MVS TEG-3 come subsequent in action after MVS TEG-1. However, the increment in output is by 7.8%, 7.4%, 7.2%, and 6.9% in MVS TEG-1, MVS TEG-2, MVS TEG-3, and MVS TEG-4 respectively.

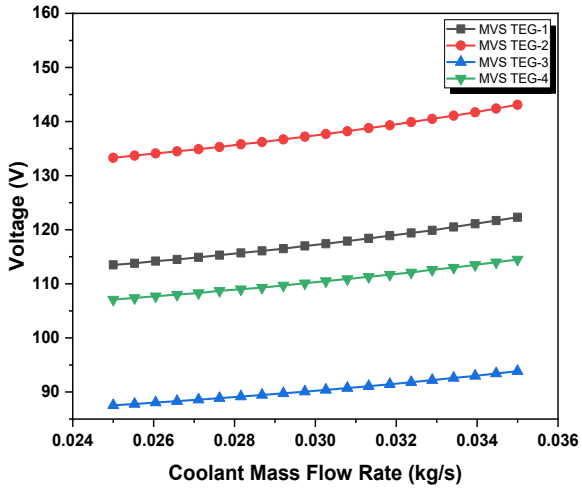

Fig. 4.19 Voltage v/s Coolant flow rate

When the coolant flow rate is raised, the increase in cold side temperature along the flow across the MVS-TEG is reduced which marks the occurrence of higher power production. This trend is observed in Fig. 4.20. Overall maximum power is generated by MVS TEG-2 which increases by 7.8%. MVS TEG-1, MVS TEG-4, and MVS TEG-3 are next in line with 7.4%, 7.2%, and 6.9% increments in power generation. Maximum power is produced by MVS TEG-2(p-type: PEDOT:Bi_2Te_3, n-type: poly[Kx(Ni-ett)] (2)).

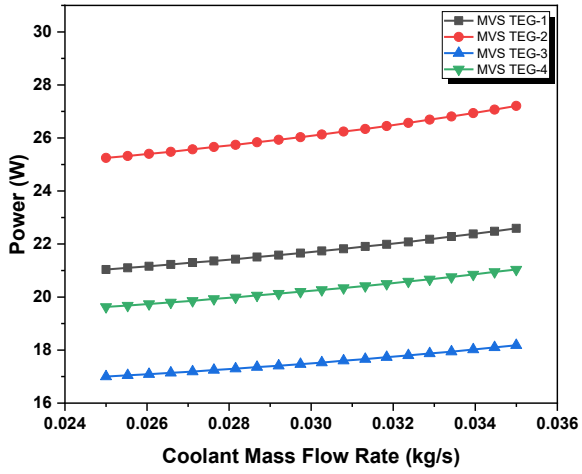

Fig. 4.20 Power v/s Coolant flow rate

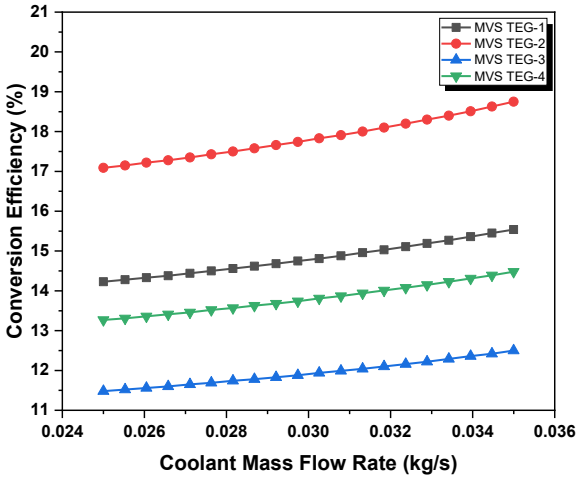

Fig. 4.21 Conversion efficiency v/s Coolant flow rate

Fig. 4.21 shows the effect of coolant flow rate on the conversion efficiencies of different MVS-TEG for 0.03kg/s and 500K exhaust flow rate and inlet temperature. Conversion efficiency increases as the coolant flow rate is varied. This happens because a higher cooling rate due to increased flow rate cools the cold side of MVS-TEG better and greater conversion efficiency is obtained as a result of a higher temperature gradient. The best performance is exhibited by MVS TEG-2 (p-type: PEDOT:Bi_2Te_3 and n-type: poly[Kx(Ni-ett)] (2)) followed by MVS TEG-1, MVS TEG-4, and MVS TEG-3. The increment in conversion efficiencies is by 9.2%, 9.71%, 8.88%, and 9.12% respectively for MVS TEG-1, MVSTEG-2, MVSTEG-3, and MVSTEG-4.

The variation of second law efficiency when the coolant flow rate is changed from 0.025 to 0.035kg/s is for different MVS-TEG at an exhaust flow rate of 0.03kg/s, the exhaust inlet temperature of 500K, and coolant flow rate of 0.03kg/s is shown in Fig. 4.22. The second law efficiency decreases by 9.13%, 8.98%, 10.33%, and 9.04% for MVS TEG-1, MVS TEG-2, MVS TEG-3, and MVS TEG-4 respectively. This happens because an increased coolant flow rate increases the overall entropy generation due to heat

transfer. However, the most efficient irreversibility action is exhibited by MVS TEG-3 while MVS TEG-2 is the worst.

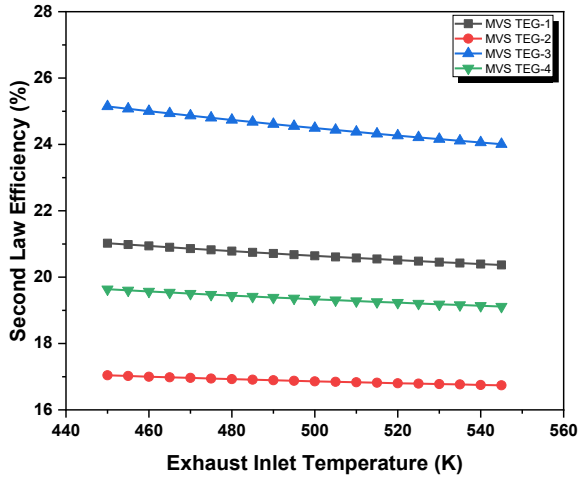

Fig. 4.22 Second law efficiency v/s Coolant flow rate

The variation of normalized parameters against coolant flow rate for different MVS-TEG considered under the theoretical study are shown in Fig. 4.23, and 4.24.

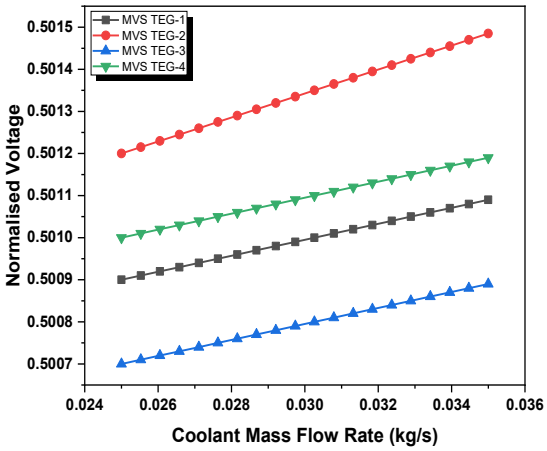

Fig. 4.23 Normalized voltage v/s Coolant flow rate

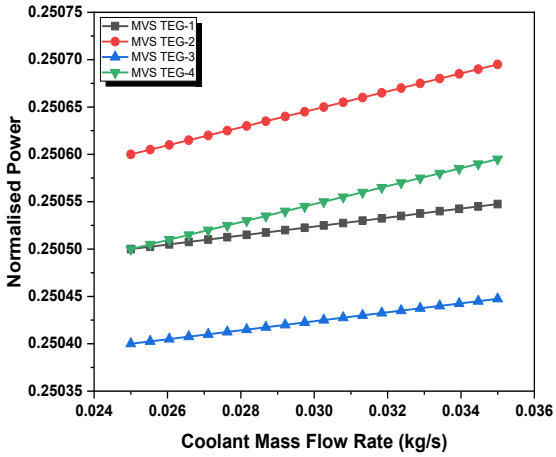

Fig. 4.24 Normalized power v/s Coolant flow rate

The normalized parameters display improved action with the coolant flow rate which is understandable due to the improved heat-carrying capacity of the coolant. The normalized voltage increases by 0.04%, 0.056%, 0.04%, and 0.038%; normalized power by 0.02%, 0.04%, 0.019%, and 0.041% for MVS TEG-1, MVS TEG-2, MVS TEG-3, and MVS TEG-4 respectively.

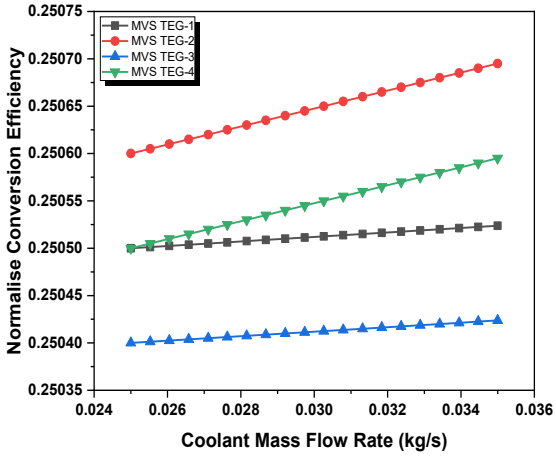

Fig. 4.25 Normalized conversion efficiency v/s Coolant flow rate

The effect of coolant flow rate on normalized conversion efficiency for different MVS-TEG at an exhaust flow rate and inlet temperature of 0.03kg/s and 500K, respectively, is shown in Fig. 4.25. The normalized conversion efficiency increases with

the coolant flow rate by 0.04% for both MVS TEG-2 and MVS TEG-4. However, it increases negligibly for MVS TEG-1 and MVS TEG-3.Thus, it is concluded that MVS TEG-3 performed the best for variation in generator row number, exhaust inlet temperature, and coolant flow rate. MVS TEG-1 occupies the second position followed by MVS TEG-4 and MVS TEG-2. Even though the transport characteristics of any material may seem healthier than the others, the effect of multi-staging and variable shape coupled with the dissimilar material combination is visible in the output parameters. The good output voltage, power, and most importantly conversion efficiency back the development of such a generator.

4.3 Highlights

- The results revealed that the most drastic effect is obtained when the row number is varied. Also, the work gives optimum values for voltage and power output as $N_x = 19$ for MVS TEG-1, MVS TEG-3, and MVS TEG-4 while $N_x = 18$ for MVS TEG-2.
- The novel MVS TEG also exhibited improved conversion efficiency, theoretically, over the conventional bismuth telluride generators. This justifies the implementation of multi-staging, tapering cross-section, and dissimilar material combinations with enhanced thermoelectric transport properties.
- The results show that exhaust inlet temperature conditions had a great influence on productivity parameters like voltage and power. The former varies by 54% to 59% and the latter by 53% to 58%.
- The second law efficiency falls by 3.12%, 1.77%, 4.53%, and 2.66% for MVS TEG-1, MVS TEG-2, MVS TEG-3, and MVS TEG-4 respectively.

- On average, the conversion efficiency increases by 9.23% for the different MVS TEG analyses in the theoretical work. However, it is observed that the second law efficiency decreases with the coolant flow rate.

Chapter 5

Thermohydraulic and TEG performance analysis with dissimilar shape-based hybrid nanofluids

Overview: This chapter explores how different nanoparticle shapes affect the cooling performance of a mini channel heat sink used to enhance the cold side of a thermoelectric generator (TEG). The study focuses on a 50:50 mixture of hybrid nanofluids containing various nanoparticles: graphene (platelet-shaped), Al_2O_3 (blade-shaped), MWCNT (cylindrical-shaped), and Fe_3O_4 (brick-shaped). The investigation considers different coolant flow rates and nanoparticle concentrations (0.1–1%). Important performance factors analyzed include heat transfer efficiency, Nusselt number, exergy at the inlet and outlet of the heat sink, cooling system efficiency (coefficient of performance, Figure of merit), and the overall impact on TEG power output and efficiency. Water is used as a reference coolant for comparison. The goal is to determine the best hybrid nanofluid composition that improves TEG performance by enhancing heat dissipation.

5.1 Mathematical Modeling

5.1.1 Design of Mini channel Heat Sink

Figs. 5.1 (a), (b), and (c) show the schematic of the overall system and the mini channel heatsink that has been investigated in the study. Copper has been chosen as the material of the MCHS because of its high thermal conductivity. The MCHS has a base area of 30mm X 20mm with nine parallel rectangular channels. The channel width and the channel height are 1mm and 3mm respectively.

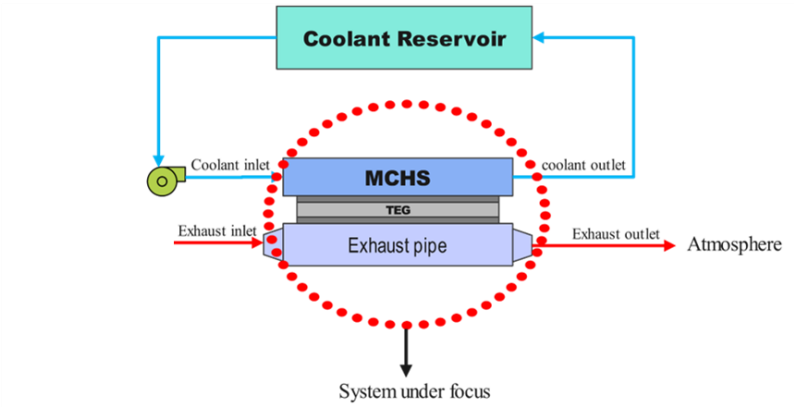

(a)

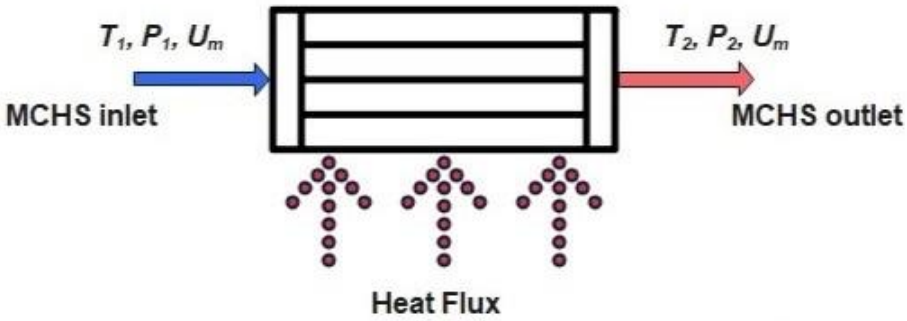

(b)

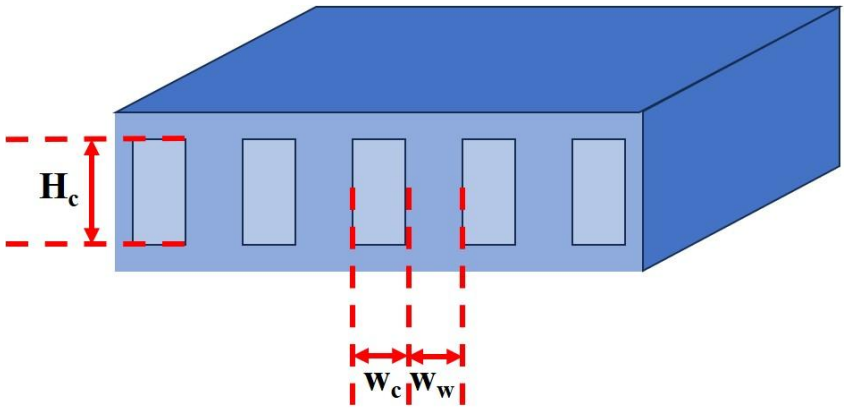

(c)

Fig. 5.1 (a) Schematic diagram of the overall system, (b) MCHS used, and (c) schematic showing MCHS dimensions

The various design variables that have been used for the numerical analysis are defined as (Shamsuddin et al., 2021):

$$\gamma = \frac{H_c}{w_c} \tag{5.1}$$

$$\beta = \frac{w_w}{w_c} \tag{5.2}$$

$$D_h = \frac{2H_c w_c}{H_c + w_c} \tag{5.3}$$

Where γ, β, and D_h denote the MCHS aspect ratio, the width ratio, and the hydraulic diameter respectively. Other important geometric parameters of the MCHS are calculated below:

$$A_c = H_c w_c \tag{5.4}$$

$$W = n(w_c + w_w) \tag{5.5}$$

$$\gamma_{inv} = \frac{1}{\gamma} \tag{5.6}$$

5.1.2 Boundary Conditions

Uniform velocity and temperature have been assumed at the inlet. The coolants (water and hybrid nanofluid of different shapes i.e., graphene-platelet shape, Al_2O_3-blade shape, MWCNT-cylindrical shape, and Fe_3O_4-brick shape) are incompressible, Newtonian, and no-slip boundary condition applies at the MCHS walls (Kumar and Sarkar, 2019). The MCHS is identical in both heat transfer and hydrodynamics. The remaining walls have been considered adiabatic. Also, the numerical analysis is done by treating the flow as steady-state, and single phase. The range of volume flow rate considered renders laminar flow because of the low value of the hydraulic diameter of the MCHS (Tuckerman and Pease, 1981). Heat rejected from the exhaust gas is equal to the heat gained by the hot side of TEG. Heat transfer due to thermal radiation is neglected. The contact resistances between the TEG - exhaust gas and TEG - coolant are neglected. Heat transfer in the ducts is neglected.

5.1.3 Fluid flow correlations

The commonly used flow parameters are calculated below:

$$\dot{m} = \rho n A_c U_m \tag{5.7}$$

$$\dot{V} = \frac{\dot{m}}{\rho} \tag{5.8}$$

$$Re = \frac{\rho U_m D_h}{\mu} \tag{5.9}$$

The pressure drop across the channel is accounted for by the following relations (Shamsuddin et al., 2021):

$$\Delta P = \Delta P_{laminar} + \Delta P_{constriction\ and\ expansion} \tag{5.10}$$

Where the individual pressure drop terms have been defined as:

$$\Delta P_{laminar} = \frac{f_{app}\rho U_m^2}{2}\left(\frac{1+\gamma}{2\gamma}\right) + \frac{\rho U_m^2}{2}\left(1.8 - \left(\frac{2.4}{1+\beta}\right) + \left(\frac{0.6}{1+\beta}\right)\right) \tag{5.11}$$

$$\Delta P_{constriction\ and\ expansion} = \frac{\rho U_m^2}{2}\left(1.79 - \left(\frac{2.32}{1+\beta}\right) + \left(\frac{0.53}{1+\beta}\right)\right) \tag{5.12}$$

$$f_{app} = \frac{\left[\left\{3.2\left(Re\frac{D_h}{L}\right)^{0.52}\right\}^2 + (18.8 + 78.57Be)^2\right]^{0.5}}{Re} \tag{5.13}$$

Where f_{app} is the friction factor that depends on the hydraulic diameter, Reynolds number, length of the mini channel heatsink, and a dimensionless parameter, *Be*, defined by Bejan (2013) as:

$$Be = \frac{\left(1 + \frac{1}{\gamma^2}\right)}{\left(1 + \frac{1}{\gamma}\right)^2} \tag{5.14}$$

Thus, the power consumed in pumping the working fluid is the product of the total pressure drop and the volume flow rate:

$$Power = \Delta P\dot{V} \tag{5.15}$$

5.1.4 Heat transfer correlations

The capacitive heat transfer by the exhaust and the coolant during flow through and various other heat transfer relations is given as follows:

$$\dot{Q_{ex}} = \dot{m}_{ex} C_{p,ex}(T_{in,ex} - T_{out,ex}) \tag{5.16}$$

$$\dot{Q}_{ex} = h_{ex} SA_{ex}(T_{avg,ex} - T_{pipe}) \tag{5.17}$$

$$\dot{Q}_H = \dot{Q}_{ex}({}^{A_{TEG}}/_{SA_{ex}}) \tag{5.18}$$

$$\dot{Q}_H = (T_{pipe} - T_h)/R_{cond} \tag{5.19}$$

$$\dot{Q}_H = N(\alpha I T_H + k(T_H - T_L) + {}^{I^2R}/_2) \tag{5.20}$$

$$\dot{Q}_L = N(\alpha I T_H + k(T_H - T_L) - {}^{I^2R}/_2) \tag{5.21}$$

$$\dot{Q}_L = \dot{m}_c C_{p,c}(T_{out} - T_{in}) \tag{5.22}$$

For the calculation of the Nusselt number, the following correlations have been used (Bejan, 2013):

$$x^* = \frac{L}{D_h Re Pr} \tag{5.23}$$

$$Nu = 1.87(x^*)^{-0.3} {\gamma_{inv}}^{-0.056} Pr^{-0.036} \tag{5.24}$$

$$Nu = 3.35(x^*)^{-0.13} {\gamma_{inv}}^{-0.12} Pr^{-0.038} \tag{5.25}$$

$$Nu = \frac{hD_h}{k_f} \tag{5.26}$$

Where x^* is the thermal entry length. The thermal entry length helps choose the Nusselt number correlation which will be used for the calculation of the average heat transfer coefficient. This parameter takes the geometry of the mini channel heatsink as well as the thermophysical properties of the coolant into account, and hence the effect of the shape factor of the various nanoparticles. The following equations are used for

ascertaining the fin efficiency of the walls, the total resistance, and the individual resistances comprising it i.e., conductive, convective, and capacitive resistance (Yang et al., 2017):

$$R_{total=}R_{cond} + R_{conv} + R_{cap} \tag{5.27}$$

$$R_{cond} = \frac{t}{k_w WL} \tag{5.28}$$

$$R_{conv} = \frac{1}{nhL(w_c + 2\eta_{fin}H_c)} \tag{5.29}$$

$$R_{cap} = \frac{1}{\dot{m}c_p} = \frac{1}{n\rho U_m H_c w_c c_p} \tag{5.30}$$

$$\eta_{fin} = \frac{\tanh(mH_c)}{mH_c}, where\ m = \sqrt{\frac{2h}{k_w w_w}} \tag{5.31}$$

Where k_w denotes the thermal conductivity of the MCHS wall and η_{fin} indicates the fin efficiency of the heatsink wall for convection. The heatsink temperature, average fluid temperature, and total heat transfer can be expressed as:

$$T_{hs} - T_{avg} = R_{total}\dot{Q}_L \tag{5.32}$$

$$T_{avg} = \frac{T_{in} + T_{out}}{2} \tag{5.33}$$

Where T_{hs} is the uniform heatsink temperature for the applied heat flux. Also, the coolant reservoir is assumed to be an infinite sink.

5.1.5 Nanoparticles and Nanofluid

Despite their enhanced thermal properties, nanofluids face challenges related to stability, as nanoparticles tend to agglomerate and settle. This can be remedied by using surfactants or surface functionalization. Additionally, their increased viscosity leads to higher pumping power requirements. Optimizing nanoparticle concentration and utilizing non-spherical shapes can help mitigate this pressure drop penalty while maintaining

superior heat transfer. However, nanofluids provide a major advantage: significantly higher thermal conductivity than base fluids, leading to vastly improved heat transfer and cooling efficiency. This allows for the design of more compact thermal systems. Their properties can also be customized for specific applications.

The volume fraction for the hybrid nanofluid is given below where subscripts 1 and 2 denote the dissimilar-shaped nanoparticles according to the blend. The Eqs. incorporate the shape effect of the nanoparticles viz., platelet, blade, brick, and cylindrical into the thermophysical property of thermal conductivity and rheological property of dynamic viscosity (Kumar and Sahoo, 2019) which considers the heat transfer characteristics, micro-convection, and frictional effects.

$$\varphi = \varphi_1 + \varphi_2 \tag{5.34}$$

$$k_{nf,1} = k_{bf}\left(1 + \left(C_{surface,1} + C_{shape,1}\right)\varphi_1\right) \tag{5.35}$$

$$\mu_{nf,1} = \mu_{bf}(1 + A_1\varphi_1 + B_1\varphi_1^2) \tag{5.36}$$

$$k_{nf,2} = k_{bf}\left(1 + \left(C_{surface,2} + C_{shape,2}\right)\varphi_2\right) \tag{5.37}$$

$$\mu_{nf,2} = \mu_{bf}(1 + A_2\varphi_2 + B_2\varphi_2^2) \tag{5.38}$$

The shape and surface influence on the thermal conductivity and viscosity are reported in Tables 5.1 and 5.2, respectively (Kumar and Sahoo, 2019).

Table 5.1: Shape-based nanoparticle thermal conductivity coefficients

Particle Type	Image	Aspect Ratio	C_{shape}	$C_{surface}$
Platelet	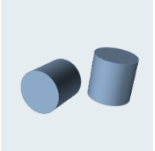	1:1/8	5.72	-3.11

Blade	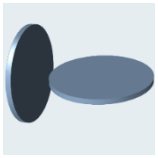	1:6:1/12	8.26	-5.52
Cylindrical	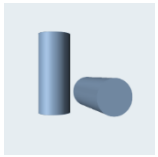	1:8	4.82	-0.87
Brick	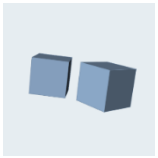	1:1:1	3.71	-0.35

Table 5.2: Shape-based nanoparticle viscosity coefficients

Coefficient	Platelet	Blade	Cylindrical	Brick
A	37.1	14.6	13.5	1.9
B	612.6	123.3	904.4	471.4

The effective thermal conductivity and dynamic viscosity have been calculated using the mixture rule for the dissimilar-shaped nanoparticle hybrid nanofluid (Ramzan et al., 2022):

$$k_{hnf} = \frac{\varphi_1 k_1 + \varphi_2 k_2}{\varphi} \tag{5.39}$$

$$\mu_{hnf} = \frac{\varphi_1 \mu_1 + \varphi_2 \mu_2}{\varphi} \tag{5.40}$$

The effective density and specific heat capacities are expressed below:

$$\rho_{hnf} = \varphi_1 \rho_1 + \varphi_2 \rho_2 + (1 - \varphi)\rho_{bf} \tag{5.41}$$

$$\rho_{hnf} c_{p,hnf} = \varphi_1 \rho_1 c_{p,1} + \varphi_2 \rho_2 c_{p,2} + (1 - \varphi)\rho_{bf} c_{p,bf} \tag{5.42}$$

The properties of the nanoparticles are illustrated in Table 5.3 (Kumar and Sarkar, 2020).

Table 5.3: Nanoparticle thermophysical properties

Particle	ρ, kg/m^3	C_p, J/kgK
Al_2O_3	3970	880
MWCNT	2600	740
Fe_3O_4	5180	670
Graphene	2200	790

The resulting heat transfer and fluid flow properties of the nanofluid are shown in Table 5.4 along with that of water.

Table 5.4: Coolant heat transfer and fluid flow properties

Coolant	k (W/mK)	μ (kg/ms)	Prandtl no.
Water	0.5945	0.0008936	6.287
Plat-blad	0.6025	0.001017	6.889
Plat-cyl	0.6043	0.001024	6.948
Plat-bric	0.6034	0.0009928	6.677
Blad-cyl	0.6045	0.0009678	6.521
Blad-bric	0.6036	0.0009371	6.256
Cyl-bric	0.6054	0.0009433	6.312

5.1.6 Performance parameters

The exergy of a system is the maximum potential work that is possible during heat interaction with the surroundings. Considering negligible changes in the kinetic and the potential energies, the fundamental exergy equations can be written as below (Mahmoud et al., 2021):

$$Ex_{in} = \dot{m}C_p\left[T_{in} - T_{amb} - T_{amb}\ln\left(\frac{T_{in}}{T_{amb}}\right)\right] \tag{5.43}$$

$$Ex_{out} = \dot{m}C_p \left[T_{out} - T_{amb} - T_{amb} \ln\left(\frac{T_{out}}{T_{amb}}\right)\right] \tag{5.44}$$

The coefficient of performance (COP) of a system is the ratio of the desired effect to the power consumed in obtaining it. Thus, the COP of the mini channel heatsink is defined as:

$$COP = \frac{\dot{Q}}{Power} \tag{5.45}$$

The Figure of Merit (FOM) is defined as the ratio of the relative Nusselt number of the hybrid nanofluid to the one-third power of the relative pressure drop of the hybrid nanofluid concerning the base fluid for a given flow rate and volume fraction in the present study. Thus, FOM gives the relative thermal advantage of the fluid over its frictional disadvantage.

$$FOM = \frac{Nu_{hnf}/Nu_{bf}}{\left(\Delta P_{hnf}/\Delta P_{bf}\right)^{1/3}} \tag{5.46}$$

5.1.7 TEG performance

The power generated and the conversion efficiency of the TEG is given as:

$$Power_{TEG} = \dot{Q}_H - \dot{Q}_L \tag{5.47}$$

$$\eta_{conversion} = \frac{Power_{TEG}}{\dot{Q}_H} X\ 100 \tag{5.48}$$

5.2 Validation

The validation process in this study consists of comparing the flow properties of the different mini-channel heat sink models used in the experimental investigation by Tuckerman and Pease (1981) with the current model. The validation is carried out for friction factor and Nusselt number against Reynolds number. The same trend is observed

in Figs. 5.2 and 5.3. As the Reynolds number increases, the inertia force dominates the viscous force, and the friction factor decreases. Also, a greater number of coolant particles interact with the hot surface per unit of time and heat transfer rate due to convection enhancement. The dimensional parameters of the Tuckerman and Pease heat sinks are tabulated in Table 5.5. The various models have been suffixed as A, B, and C.

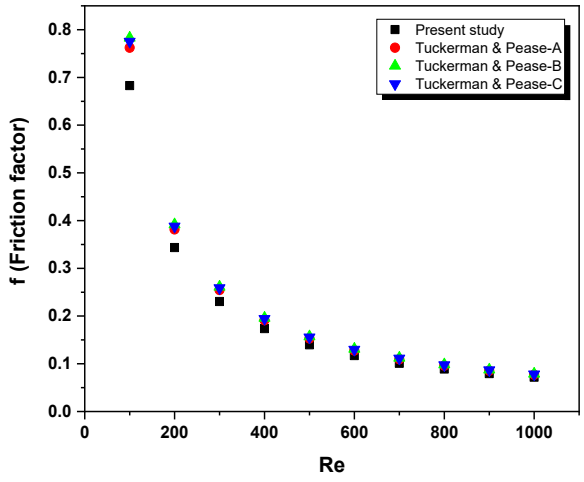

Fig. 5.2 Friction factor versus Reynolds number validation of the present model

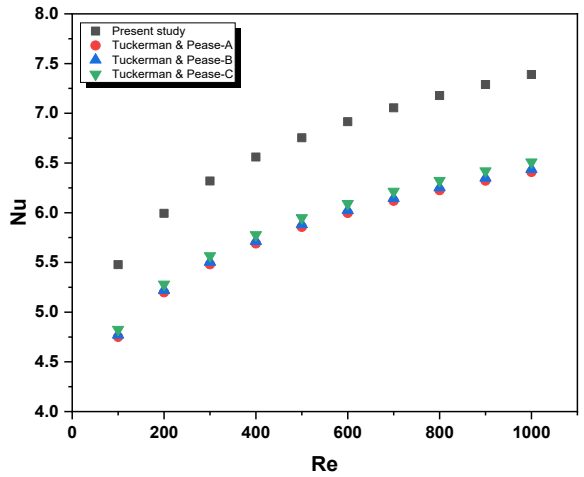

Fig. 5.3 Nusselt number versus Reynolds number validation of the present model

Table 5.5: Geometric specifications of the Tuckerman & Pease model used for validation

Parameters	Model A	Model B	Model C
H_c (mm)	0.287	0.302	0.320
w_c (mm)	0.055	0.05	0.056
w_w (mm)	0.045	0.05	0.044
t (mm)	0.143	0.256	0.213
D_h (mm)	0.0923	0.0858	0.0953

The friction factor of the different models confirms more precisely the present model at a high Reynolds number. However, the Nusselt number somewhat maintains a regular deviation for the Reynolds number variation from 100 to 1000. The difference in the hydraulic diameter of the different MCHS causes this variation in the values. For the validation process, water has been used as the coolant. On evaluation, the percentage variation in the friction factor of the present model is 8.4%, 10.74%, and 9.93% concerning models A, B, and C respectively. The deviation variations are 12.76% with model B and 6.39% with model A respectively. Similarly, the average variations in the Nusselt numbers are 15.29%, 14.87%, and 13.53%. Thus, a good agreement of the friction factors and Nusselt number values is found among different T and P models and the present model.

5.3 Results and Discussion

5.3.1 Heat transfer coefficient

The variation of the heat transfer coefficient with the volume flow rate for different coolants (i.e., water and hybrid nanofluid of dissimilar-shaped nanoparticles for φ=0.001) is shown in Fig. 5.4 (a). The coolant has been supplied at 25°C inlet temperature

as it was the room temperature measured at the time of the study. It is observed that the heat transfer coefficient increases with the volume flow rate. The hybrid nanofluids exhibit enhanced heat transfer coefficients due to increased thermal conductivity which is supported by Eq. (5.26) and pieces of literature. The cylindrical-brick (MWCNT-Fe_3O_4) shape blend shows the highest heat transfer coefficient throughout the variation of the volume flow rate. This shape blend is observed to have maintained an average heat transfer coefficient of 79.27% more than that of the water. The last enhancement is shown by the platelet-blade (graphene-Al_2O_3) shape blend which is 79.24% more than that of the water for the smallest volume flow rate. The rest of the blends possess relatively lower values of heat transfer coefficient than the cylindrical-brick (MWCNT-Fe_3O_4) blend. It is also found that the rate of increase of the parameter starts decreasing slowly as the volume flow rate of the coolant is increased. It may be because as the flow rate is increased, along with the introduction of the nanoparticles, the phenomena of Brownian motion is enhanced, and movement of the base fluid causes micro-convection around the nanoparticles. It happens because an increased volume flow rate enhances the Brownian motion and the micro-convection of the base fluid around the nanoparticles. The increase in volume concentration of the nanoparticles on the base fluid has been known to enhance the heat transfer coefficient.

Fig. 5.4 (b) shows that at a volume flow rate of 0.000004m^3/s and an inlet temperature of 25°C, the coefficient of heat transfer rises with the volume fraction of the nanoparticles. As the number of nanoparticles is increased in the base fluid, the number of nanoparticles carrying the heat in the mini channel increases, and the thermal transport properties of the coolant are improved. Among all the blends that have been studied, the cylindrical-brick (MWCNT-Fe_3O_4) shape blend exhibited the maximum heat transfer coefficient throughout the volume fraction variation.

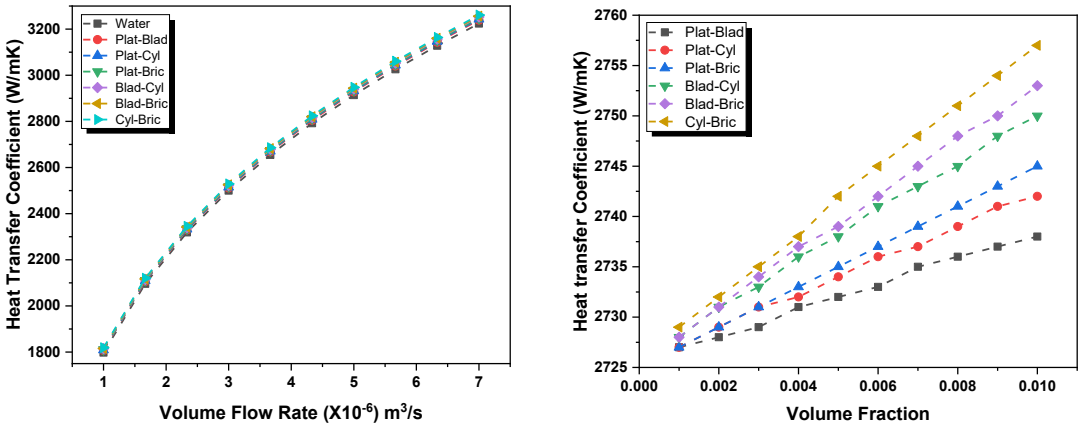

(a) **(b)**

Fig. 5.4 (a) Heat Transfer Coefficient v/s Volume Flow Rate (b) Heat Transfer Coefficient v/s Volume Fraction

This increment is about approximately 1.03% at φ=0.01 in comparison with that at φ=0.001 of the dissimilar-shaped nanoparticles hybrid nanofluid. However, is noticed that the coefficient increased by only 0.4% or 11W/m^{2}K for the platelet-blade blend. Also, it is noticeable, both in the case of volume flow rate and volume fraction variation, that any hybrid nanofluid blend consisting of the platelet shape performs relatively poorly in comparison to the rest of the blends in terms of the heat transfer coefficient. It may be because of the inefficient collision of the platelet-shaped nanoparticles with the other shapes that are being studied. However, it still exhibits better thermal characteristics than the base fluid i.e., water.

5.3.2 Nusselt number

With an increase in flow rate, the number of nanoparticles carrying away the heat from the channel surface increases. Thus, the Nusselt number, a dimensionless parameter that characterizes heat transfer increases with an increase in the volume flow rate of the working fluid. Fig. 5.5 (a) shows the same trend where the Nusselt number rises as the volume flow rate rises at φ=0.001 and inlet temperature of 25°C for the water-based,

dissimilar-shaped nanoparticles hybrid nanofluid. The variation trend of the Nusselt number is like that of the heat transfer coefficient when the volume flow rate is varied. As the volume flow rate is increased, the Reynolds number increases which is one of the major factors for the Nusselt number increment. The highest values of the Nusselt number are observed for the blade-brick blend which stays marginally higher than the cylindrical-brick blend. Initially, the Nusselt number value of the blade-brick blend is 1.74% higher than that of the water.

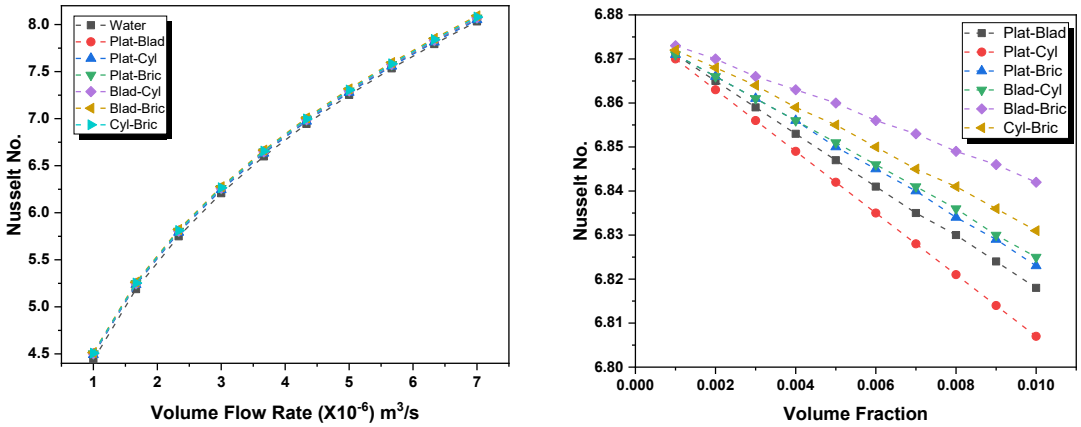

(a) **(b)**

Fig. 5.5 (a) Nusselt number v/s Volume Flow Rate (b) Nusselt number v/s Volume Fraction

However, as the flow rate is increased, this increment slowly diminishes to 0.75% at the flow rate of 0.000007m^3/s. The Nusselt number enhancement also implies that the convective heat transfer rate using a hybrid nanofluid also surges in comparison to the conductive heat transfer that occurs at the solid-liquid interface. The dispersing of dissimilar-shaped nanoparticles into the base fluid results in a trivial reduction in the Nusselt number as the volume fraction is increased. Fig. 5.5 (b) shows this fall at 25°C inlet temperature and 0.000004m^3/s volume flow rate of the different coolants. In the instance of similar particles, the particles tend to aggregate and form clusters that have

better heat transfer capabilities. This effect seemed to be lacking in the case of the combination of dissimilar nanoparticles. However, the negligible fall in the parameter is something that can be traded off in exchange for the faster cooling rate that comes along with the increase in the thermal conductivity of the coolants. This is because the addition of nanoparticles results in increased Brownian motion, rupture of the thermal boundary layer, and micro-convection. Talking about the shape effect of the nanoparticles, the blade-brick (Al_2O_3-Fe_3O_4) blend renders the best performance while the platelet-cylindrical (graphene-MWCNT) blend does not. The Nusselt number of the blade-brick blend reduces by 0.45% whereas, for the platelet-cylindrical blend, the reduction is 0.92%. A point that should be noted is that the brick shape presence enhances the heat transfer capabilities of the hybrid nanofluid. It might be due to the availability of surfaces of equal area on all sides which improves the efficiency of heat transfer due to better collision. A similar fall has been observed in a previous study.

5.3.3 Inlet and Outlet Exergy

Fig. 5.6 (a) shows the variation of the exergy at the inlet of the mini channel of the coolants against the volume flow rate at φ=0.001 and 25°C inlet temperature. Since the exergy directly depends on the coolant's mass flow rate, it rises as the volume flow rate rises. This variation has been reported before by authors. The exergy at the inlet is also a function of the temperature at the inlet of the mini channel and the ambient temperature. However, when the inlet temperature and the ambient temperature are fixed, the inlet exergy varies directly with the mass flow rate. Also, the different densities and heat capacities result in the discrete exergetic performance of the dissimilar-shaped nanoparticle hybrid nanofluid. From the figure, it can be ascertained that the blade-cylindrical (Al_2O_3-MWCNT) blend possesses the highest inlet exergy and increases by 1.044W. The blade-brick (Al_2O_3-Fe_3O_4) blend does not achieve fair exergetic

performance as it had been achieved in the thermal parameters. This might be due to better convective and conductive characteristics than capacitive ones. However, the rise in the exergetic opportunity is very close to that of the blade-brick blend i.e., 1.03 W for the blade-brick blend. The rise in the inlet exergy of the cylindrical-brick (MWCNT-Fe_3O_4) blend is also 1.044 W and it is next in the exergetic performance when compared to the blade-cylindrical blend.

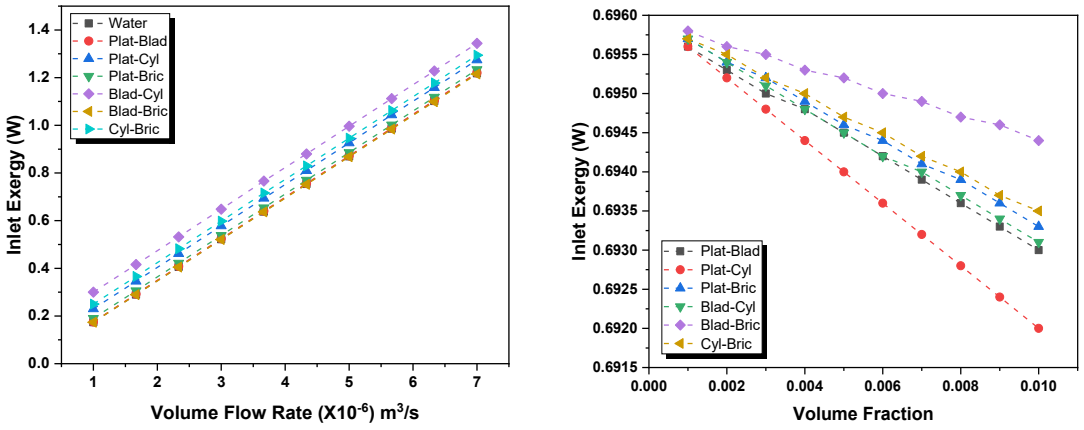

(a) **(b)**

Fig. 5.6 (a) Exergy at inlet v/s Volume Flow Rate (b) Exergy at inlet v/s Volume Fraction

With the increase in the proportion of the dissimilar-shaped nanoparticle in the coolant, the exergy at the inlet decreases, as can be observed from Fig. 5.6 (b). As the volume percentage of the different-shaped nanoparticle rises, the inlet exergy falls. The blade-brick shape blend exhibits the highest exergy while the platelet-cylindrical (graphene-MWCNT) shows the least. The minimum fall in the parameter is approximately 0.2% for the blade-brick blend.

The exergy at the outlet decreases as the volume flow rate increases. This is because as the volume flow rate is increased thermal entropy generation reduces due to a reduction in outlet temperature. Fig. 5.7 (a) shows the non-linear decrement of outlet

exergy as the volume flow rate is increased. The exergy at the outlet reaches negligible exergy because of a drastic fall in the outlet temperature, close to the ambient temperature. The exergy for blade-cylindrical (Al_2O_3-MWCNT) shape blend reduces by 25.7W while that for water decreases by 24.9W.

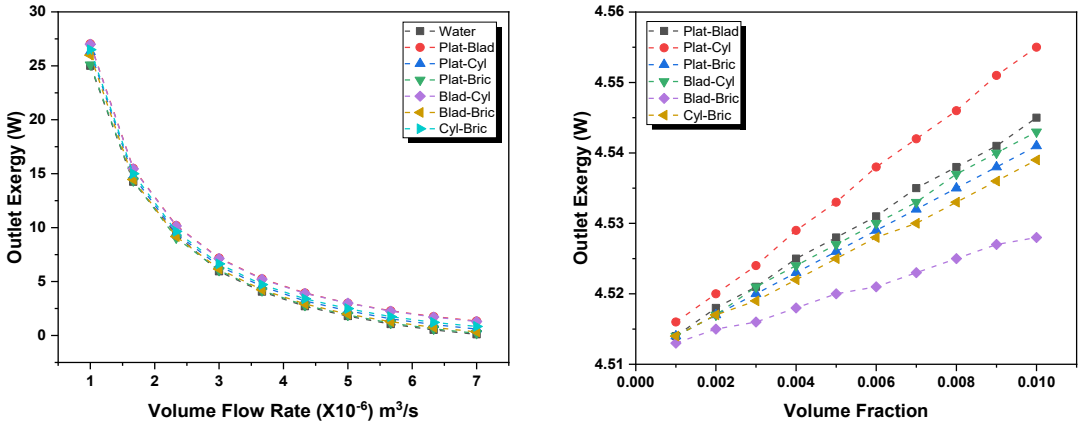

(a) **(b)**

Fig. 5.7 (a)Exergy at outlet v/s Volume Flow Rate (b) Exergy at outlet v/s Volume Fraction

Fig. 5.7 (b) shows the variation of outlet exergy with the change in volume fraction of the dissimilar-shaped nanoparticle hybrid nanofluids at 0.000004m^3/s and 25°C inlet temperature. The exergy at the outlet increases as the concentration of the particles increases. This is because the heat capacity of the coolant decreases with the introduction of the nanoparticles. The particles get heated up easily and so does the fluid surrounding the nanoparticles. The different shapes of the particles influence the heat transfer capabilities. Hence, this increment in the parameter is observed. Talking of the quantitative rise in the exergy at the outlet, it is 0.86% for the platelet-cylindrical shape blend, and 0.36% for the blade-brick shape blend.

5.3.4 Effect on the performance parameters

The coefficient of performance (COP) drops drastically as the volume flow rate is increased for both water and the hybrid nanofluid with φ=0.01 at 25°C inlet temperature as depicted in Fig. 5.8 (a). The COP of the heat sink applied with the hybrid nanofluid shows poor performance relative to water in terms of COP. This is because, for the removal of heat flux, the drop in pressure across the channel is more for the nanofluid. The dispersion of dissimilar-shaped nanoparticles to enhance thermal performance comes at the penalty of increased pressure drop or pumping power. The presence of nanoparticles increases the density and viscosity of the coolant which has been proved in many pieces of literature. The cylindrical-brick (MWCNT-Fe_3O_4) shape blend performs better than the other blends while the platelet-cylindrical combination exhibits the worst performance.

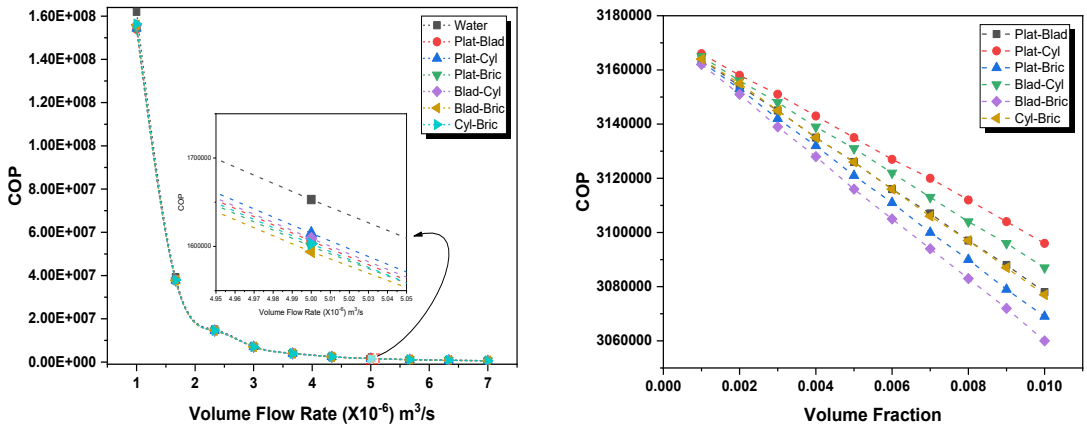

(a) **(b)**

Fig. 5.8 (a) COP v/s Volume Flow Rate (b) COP v/s Volume Fraction

However, at high flow rates, the COP of all the coolants converges which indicates that water is as good as any combination of articles at high volume flow rates. Fig. 5.8 (b) demonstrates the variation of COP with the volume fraction of dissimilar-shaped nanoparticle hybrid nanofluid from φ=0.001 to φ=0.01 at 25°C inlet temperature at a volume flow rate of 0.000004m^3/s. The COP of the mini channel heat sink applied with

the nanofluid for the given conditions and properties is observed to decrease with the increase in the volume concentration of nanoparticles. The platelet-cylindrical (graphene-MWCNT) shape blend exhibits the highest while the blade-brick (Al_2O_3-Fe_3O_4) shape blend shows the least COP among the combinations that are investigated in the study. The COP of platelet-cylindrical decreases by 2.21% and that of blade-brick decreases by 3.22%.

Fig. 5.9 (a) shows FOM variation with the volume flow rate of the coolant. As the flow rate increases, the Figure of merit increases. The enhancement is rapid in some of the dissimilar-shaped nanoparticle hybrid nanofluids. The ones possessing higher values initially do not exhibit much improvement while the ones with relatively smaller values show drastic increments. From close observation, the coolant with platelet shape nanoparticles in the blend showed a sudden increment. Also, the highest FOM is demonstrated by the blade-brick (Al_2O_3-Fe_3O_4) and the blade-cylindrical (Al_2O_3-MWCNT) shape blend at different flow rates. However, the highest enhancement is exhibited by the platelet-cylindrical (graphene-MWCNT) shape blend i.e., by 0.83%. Even though the Nusselt number is enhanced with the introduction of nanoparticles, pressure drop caused due to their presence hamper the FOM of the dissimilar-shaped hybrid nanofluid. As the volume flow rate increases, the Nu increases but still FOM value remains lower than 1 due to an overwhelming pressure drop.

The impact of the volume fraction variation of the dissimilar-shaped nanoparticles at 25°C inlet temperature and volume flow rate of 0.000004m^3/s is shown in Fig. 5.9 (b). The Figure of merit drops as the volume fraction of the nanoparticles increases.

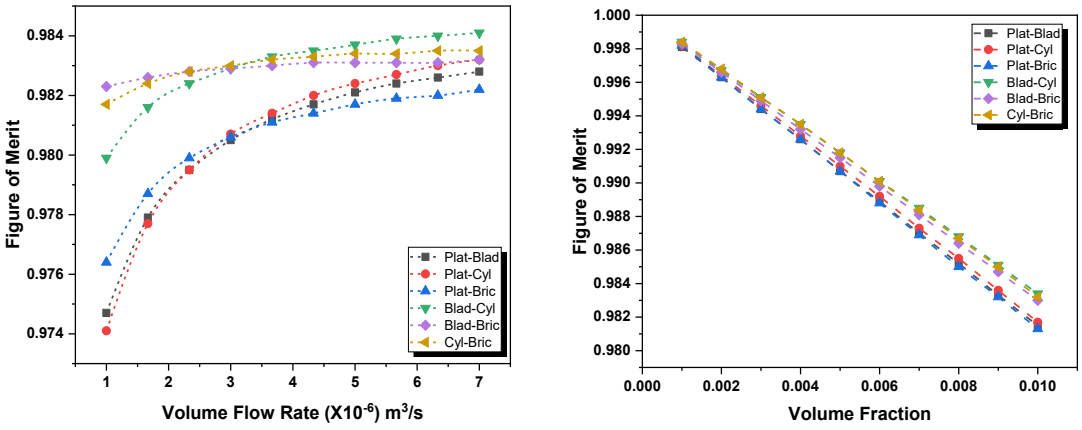

(a) **(b)**

Fig. 5.9 (a) Figure of Merit v/s Volume Flow Rate (b) Figure of Merit v/s Volume Fraction

It decreases by 1.5% for the blade-cylindrical (Al_2O_3-MWCNT) shape blend and by 1.69% for the platelet-brick (graphene-Fe_3O_4) blend. This is because the increase in the volume concentration of the nanoparticles of dissimilar shapes affects the hydraulic performance of the nanofluid adversely. It increases the density and viscosity of the coolant while decreasing its heat capacity. As a result, increased density and viscosity deteriorate the FOM of the hybrid nanofluid.

5.3.5 Effect on TEG performance

Fig. 5.10 (a) illustrates the relationship between the power output of a thermoelectric generator (TEG) and the volume flow rate of hybrid nanofluids. A distinct upward trend is observed, indicating that as the volume flow rate increases, the power output of the TEG also improves. This suggests that higher flow rates enhance the convective heat transfer, effectively maintaining a greater temperature gradient across the TEG, which directly contributes to increased power generation. Compared to water, which serves as the baseline coolant, all hybrid nanofluid formulations exhibit superior performance, demonstrating their enhanced thermal conductivity and heat transfer

capabilities. As the flow rate increases, the gap between different nanofluid formulations widens, indicating that at higher flow rates, the influence of nanoparticle shape on heat transfer becomes more pronounced. Fig. 5.10 (b) presents the relationship between the power output of a thermoelectric generator (TEG) and the volume concentration of hybrid nanofluids. A clear increasing trend is observed, indicating that as the volume concentration of nanoparticles increases, the power output of the TEG also rises. This suggests that higher nanoparticle concentrations enhance heat transfer, leading to more effective temperature differences across the TEG, which directly improves power generation. The highest TEG power and conversion efficiency is exhibited when a cylindrical-brick (MWCNT-Fe_3O_4) blend is used. The highest values obtained are 6.085W and 5.47% respectively.

Fig. 5.11 (a) illustrates the relationship between the conversion efficiency of a thermoelectric generator (TEG) and the volume flow rate of hybrid nanofluids. A clear trend is observed where the efficiency of TEG increases with an increasing flow rate for all the hybrid nanofluids tested. This trend suggests that higher flow rates enhance convective heat transfer, improving thermal management on the cold side of the TEG. Among the various hybrid nanofluids, platelet-brick (graphene-Fe_3O_4) and blade-brick (Al_2O_3-Fe_3O_4) exhibit the highest efficiency gains, outperforming all other combinations. These formulations likely benefit from the superior thermal conductivity and surface area effects of the brick-shaped nanoparticles, which enhance heat dissipation. Following closely behind, the blade-cylindrical (Al_2O_3-MWCNT) and cylindrical-brick (MWCNT-Fe_3O_4) blend also show significant efficiency improvements. On the other hand, the platelet-blade (graphene-Al_2O_3) hybrid nanofluid shows the least enhancement in conversion efficiency, performing only marginally better than water, which serves as the baseline coolant.

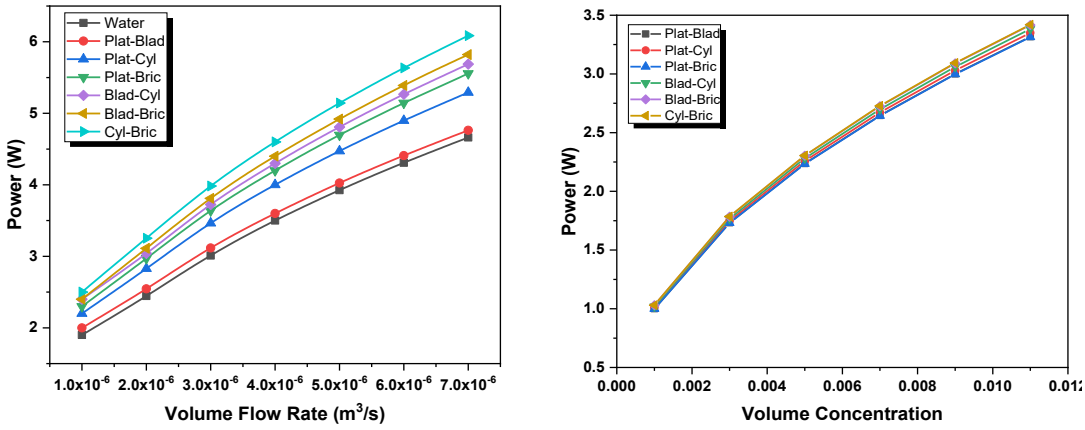

(a) **(b)**

Fig. 5.10 (a) TEG Power v/s Volume Flow Rate (b) TEG Power v/s Volume Fraction

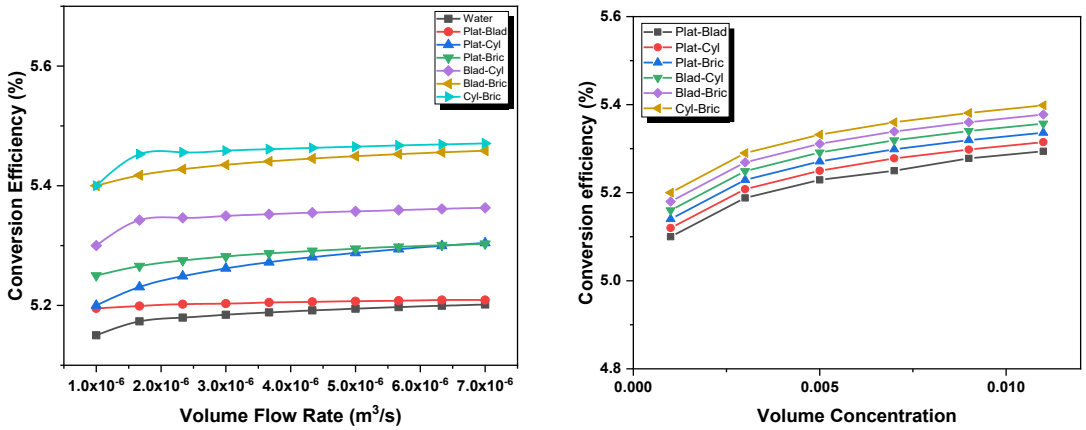

(a) **(b)**

Fig. 5.11(a) TEG conversion efficiency v/s Volume Flow Rate (b) TEG conversion efficiency v/s Volume Fraction

Fig. 5.11 (b) depicts the relationship between the conversion efficiency of a thermoelectric generator (TEG) and the volume concentration of hybrid nanofluids. A clear increasing trend is observed, where the TEG efficiency improves as the volume concentration of the nanofluid increases. This suggests that higher nanoparticle

concentrations contribute to enhanced thermal conductivity and improved convective heat transfer, resulting in better cooling on the cold side of the TEG. Among the tested hybrid nanofluids, the cylindrical-brick blend consistently achieves the highest efficiency across all volume concentrations, followed closely by the blade-brick (Al_2O_3-Fe_3O_4) and blade-cylindrical blend. These results indicate that incorporating brick-shaped nanoparticles significantly enhances the thermal performance, likely due to their high thermal conductivity and effective dispersion in the fluid.

5.4 Highlights

This research presents a novel investigation into the pivotal, yet underexplored, role of nanoparticle geometry in optimizing hybrid nanofluids for thermoelectric generator (TEG) cooling. Its primary contribution is a comprehensive evaluation of four distinct nanoparticle shapes (platelets, blades, cylinders, bricks) within a 50:50 hybrid mixture, providing deep insight into their synergistic effects on thermal-hydraulic performance and exergy dynamics. While employing established correlations, the innovative methodology lies in its systematic multi-parameter analysis, linking specific shapes to enhanced heat dissipation, improved coefficient of performance, and ultimately, significant gains in overall TEG power output and efficiency, surpassing conventional water or single-shape studies. The highlights are as follows:

- The average HTC increases with the increase in both volume flow rate and volume concentration due to an increase in thermal conductivity, relative motion between the nanoparticles, and micro-convection at the nanoparticle surface.
- The cylindrical-brick (MWCNT-Fe_3O_4) blend performs the best in terms of thermal properties with 79.27% enhancement with volume flow rate variation and 1.03% enhancement with the volume concentration.

- The blade-cylindrical (Al_2O_3-MWCNT) blend shows the best performance when the FOM is considered. The Figure of merit increases with the increase in the volume flow rate and the highest FOM observed is 0.9841.
- Also, a value of the Figure of merit lower than 1 for all the hybrid nanofluids is obtained.
- TEG power increases with volume flow rate due to increased cooling effect. Volume concentration increment enhances the TEG performance in terms of power and conversion efficiency.
- The highest TEG power and conversion efficiency are 6.085W and 5.47% respectively.
- Cylindrical-brick (MWCNT-Fe_3O_4) hybrid nanofluid gives the best TEG performance.

This page is left intentionally blank

Chapter 6

Taguchi optimization and ANN modeling for Uni-array Vortex Generators

Overview: The present chapter investigates the thermohydraulic performance of different vortex generator (VG) geometries in a rectangular channel under varying ambient conditions. The examined VG shapes include delta (D), envelope (M), and fishtail (F), with ambient heat transfer coefficients (HTCs) of 5, 15, and 25W/m²K. Various thermal and fluid flow parameters are considered to evaluate performance. The study employs the Taguchi design of experiments to determine the necessary run combinations, while analysis of variance (ANOVA) and signal-to-noise (S/N) ratios help identify the optimal factors influencing the outcome. Additionally, an artificial neural network (ANN) model is developed, demonstrating high prediction accuracy with a strong coefficient of determination.

6.1 Geometry, Governing Equation, and Boundary Conditions

The arrangement of the vortex generators has been shown in Fig. 6.1 (a-c). The vortex generators shown are (a) Delta VG (DVG), (b) Envelope VG (MVG, the acronym M for their M-like shape), and Fishtail VG (FVG). The dimensions of the channel under study are 360mm x 70mm x 20mm (length x width x height). The angle of inclination (θ) employed here is 60° respectively, as per the findings of the previous chapter. Thus, a total of 8 VGs are placed inside the rectangular channel. The distance between consecutive VGs is 40mm. The angle of inclination (θ) is defined as the angle between the face of the vortex generator and the horizontal as depicted in Fig. 6.2 (a). Fig. 6.2 (b-d) exhibits the geometry of the different vortex generators used.

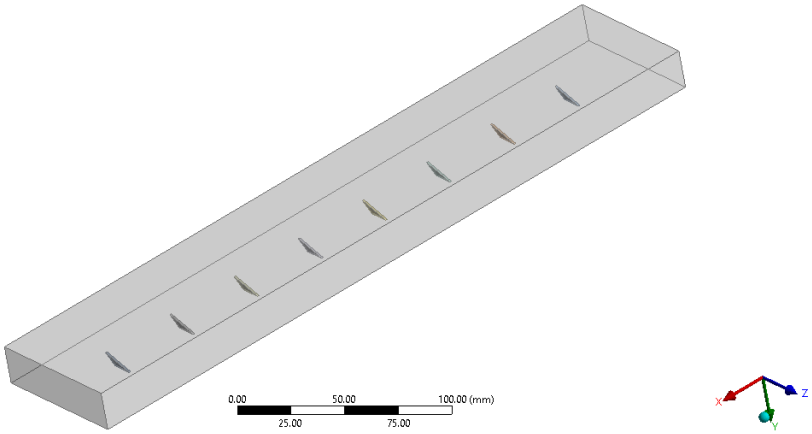

(a)

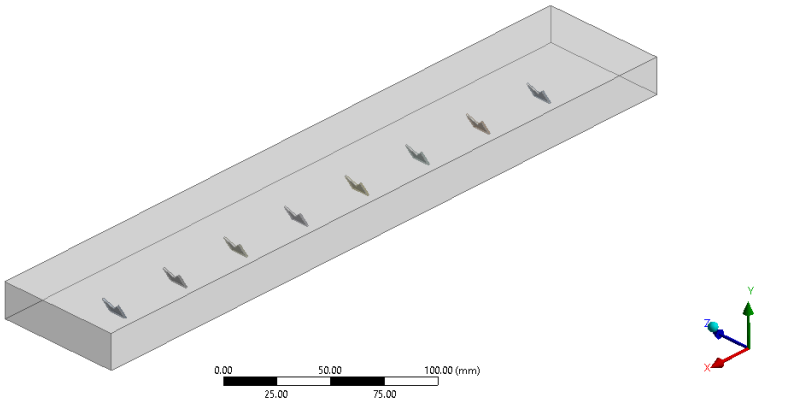

(b)

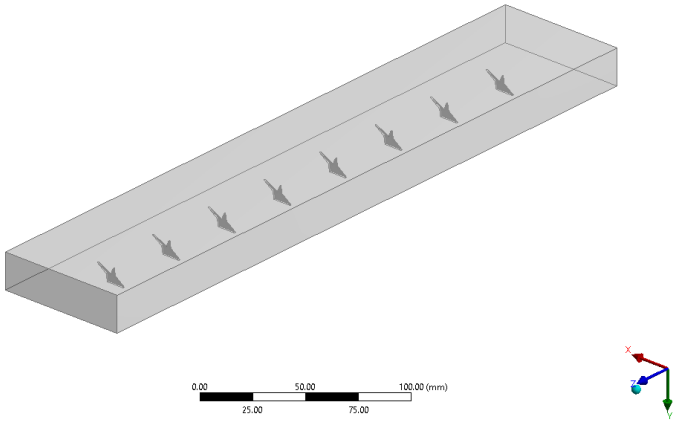

(c)

Fig. 6.1 (a-c) Different Vortex Generator configurations

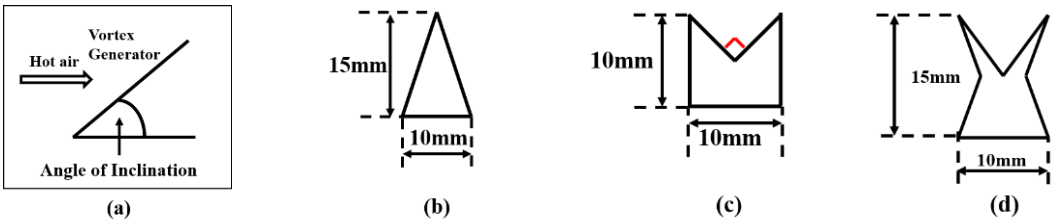

Fig. 6.2 (a) Angle of inclination definition, (b-d) Dimensions of the VGs

When the hot air flows past these vortex generators, their path gets deflected and vortices are formed. Vortex generators create controlled vortices or swirls in the fluid flow. This increased turbulence disrupts the boundary layer, promoting better mixing among the fluid particles. Enhanced turbulence results in more efficient heat transfer by diminishing the thickness of the thermal boundary layer and upsurging the heat transfer coefficient. A low-pressure region is created just adjacent to the vortex generators. This causes whirling of the hot air, which mixes the fluid thoroughly. The growth of the thermal boundary layer is disrupted. However, it also increases turbulence in the flow. Turbulence causes more frictional losses as the fluid moves through the channel, resulting in a higher pressure drop. The vortices themselves also dissipate energy as they interact with the fluid, further contributing to pressure loss. Furthermore, different shapes of the VGs produce different flow patterns, resulting in unique hydraulic and thermal performances. Several vortex generators in an array help to enhance the thermal action by continuously disrupting the flow. The numerical analysis has been done using ANSYS 2022R2.

In this study, the considered hot air is treated as incompressible and continuous, and the simulations are conducted under stable states. The determination of the heat exchanger surface temperature is achieved through the application of conjugate heat transfer equations within the computational unit. The governing eqs. are as follows:

Continuity Eq., $\frac{\partial}{\partial x_i}(\rho u_i) = 0$ (6.1)

Momentum Eq., $\frac{\partial}{\partial x_i}(\rho u_i u_k) = \frac{\partial}{\partial x_i}\left(\mu \frac{\partial u_k}{\partial x_i}\right) - \frac{\partial p}{\partial x_k}$ (6.2)

Energy Eq., $\frac{\partial}{\partial x_i}(\rho u_i T) = \frac{\partial}{\partial x_i}\left(\Gamma \frac{\partial T}{\partial x_i}\right)$ (6.3)

Here, ρ and μ represent density and dynamic viscosity, respectively. The diffusion coefficient Γ is defined as thermal conductivity divided by the specific heat ($\Gamma=k/Cp$). Eqs. (6.4) and (6.5) simulate turbulent flow using the k-ε model, as given by (Wilcox, 1998).

$$\frac{\partial}{\partial x_i}(\rho k u_i) = \frac{\partial}{\partial x_j}\left[\left(\mu + \frac{\mu_t}{\sigma_k}\right)\frac{\partial k}{\partial x_j}\right] + G_k + G_b - \rho\epsilon - Y_M + S_k \tag{6.4}$$

$$\frac{\partial}{\partial x_i}(\rho \epsilon u_i) = \frac{\partial}{\partial x_j}\left[\left(\mu + \frac{\mu_t}{\sigma_\epsilon}\right)\frac{\partial \epsilon}{\partial x_j}\right] + C_{1\epsilon}\frac{\epsilon}{k}(G_k + C_{3\epsilon}G_b) - C_{2\epsilon}\rho\frac{\epsilon^2}{k} + S_\epsilon \tag{6.5}$$

Within this framework, G_k, G_b, and Y_M signify the creation of turbulence kinetic energy arising from the mean velocity gradient, buoyancy effects, and the involvement of fluctuating dilation in turbulence towards the comprehensive dissipation rate. The constants $C_{1\epsilon}$, $C_{2\epsilon}$, and $C_{3\epsilon}$ play a crucial role in these formulations. The turbulent viscosity, μ_t, is modeled as:

$$\mu_t = \rho C_\mu \frac{k^2}{\epsilon} \tag{6.6}$$

The production of k is defined by the following Eqs.:

$$P_k = -\rho \overline{u_i' u_j'} \frac{\partial u_j}{\partial x_i} \tag{6.7}$$

$$P_k = \mu_t S^2 \tag{6.8}$$

Where the mean rate of strain tensor, S, is:

$$S \equiv \sqrt{2 S_{ij} S_{ij}} \tag{6.9}$$

The channel is supplied with a uniform velocity and temperature of the hot air at the inlet. No-slip boundary condition prevails at the walls. The rectangular channel is subjected to natural convection in the surroundings. Boundary conditions are specified at the inlet, and wall as follows:

Inlet: $u = u_{in}, v = w = 0, T = T_{in}$ (6.10)

Wall: $u = v = w = 0, q = q_{conv}$ (6.11)

The heat conservation eq. can be derived for each control volume, delineating the heat dissipation within the control unit originating from the hot gas (Q).

$$Q_i = m_e C_{p,e}(T_{e,i} - T_{e,i+1}) \tag{6.12}$$

The average control unit temperature can be computed utilizing Eq. (6.13). Furthermore, convective heat transfer is given by Eq. (6.14).

$$T_{avg\ i,i+1} = \frac{T_{e,i} + T_{e,i+1}}{2} \tag{6.13}$$

$$Q_i = h_{e,i} Ar\left(T_{avgi,i+1} - T_{in,i,i+1}\right) \tag{6.14}$$

The friction factor and TEF are determined using the Eqs. (6.15), and (6.16) respectively.

$$f = \frac{(\Delta P/L) D_m}{(\rho V^2/2)} \tag{6.15}$$

$$TEF = \frac{\frac{Nu}{Nu_o}}{\left(\frac{f}{f_o}\right)^{1/3}} \tag{6.16}$$

Here, *Nu* is the Nusselt number, Nu_o is for a smooth channel, *f* is the friction factor, and f_{or} smooth channel.

6.2 Grid Independence Test and Data Validation

The comprehensive simulations conducted for 3D vortex generators on heat exchangers necessitate precise mesh generation to accurately compute temperature and

velocity distributions. Considering the complexity of VGs, a tetrahedral mesh is utilized for fluid and plate areas, while a quad-mesh is employed for upstream and downstream extended regions, as depicted in Figs. 6.3(a-c). An adaptive mesh refinement technique is applied to the fluid regions and the walls of VGs to ensure a finer mesh.

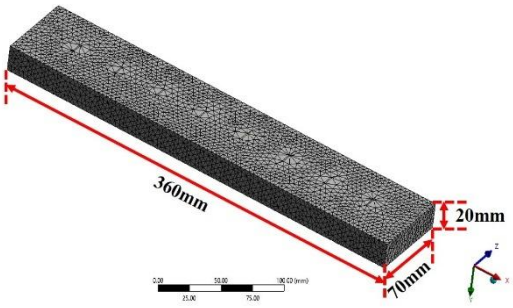

(a)

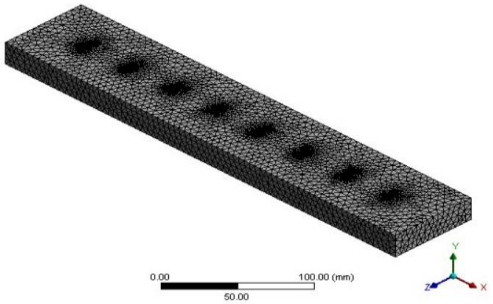

(b)

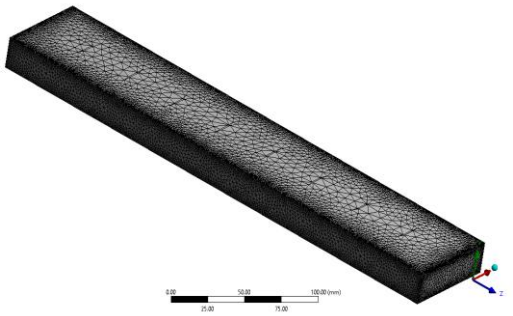

(c)

Fig. 6.3 (a-c) Meshing of VGs and rectangular channel

To evaluate numerical accuracy, flow through a channel with vortex generators set at a 60° angle, and fishtail-shaped at node 1, was studied. Four different grid

configurations, ranging from 104,003 to 853,102 elements, were examined. Table 6.1 illustrates that the grid setup containing 571,835 cells displays a comparative discrepancy in HTC and pressure drop of less than 1% compared to the configuration with the highest number of cells (853,102). Therefore, for subsequent calculations, the grid configuration with 571,835 cells or a closely resembling setup was selected as the working grid size, with consideration given to computational resources and computation time.

Table 6.1: Grid Independence Test (α=60°, distance to height=2, fishtail shape)

Grid	Elements	h(W/m^{2}K)	Error	ΔP(Pa)	Error
Grid 1	104,003	101.878	-	39.7574	-
Grid 2	324,866	98.1927	3.61%	35.7181	10.15%
Grid 3	571,835	95.8460	2.37%	34.4426	11.96%
Grid 4	853,102	96.0089	0.19%	34.6182	0.50%

Fig. 6.4 shows the data validation for the present study with the experimental work discussed previously. Validation has been performed for fishtail vortex generator configuration (α=60°, distance to height=2). The extreme discrepancy occurs at the highest Reynolds number. The validation is done for the smooth channel. The deviation value calculated reaches a maximum of 6.77%. The cause of this may be the presence of environmental conditions like ambient temperature variation during the experiment, humidity content in the air, and experimental uncertainties. The maximum deviation is well within the acceptable limits.

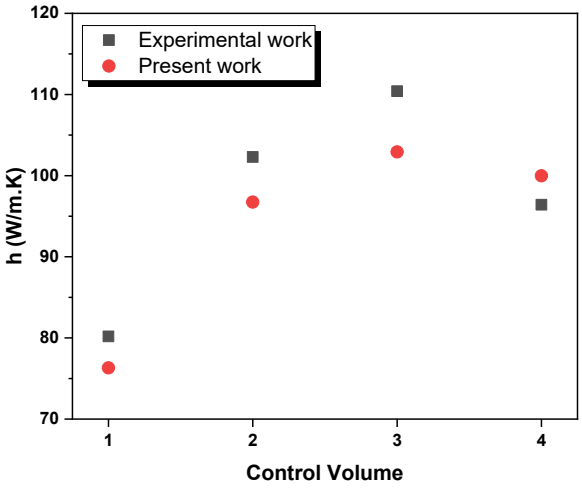

Fig. 6.4 Validation with experimental work

6.3 Taguchi's Analysis-Design of experiments

The Taguchi method is a statistical approach to optimization and quality improvement in processes. It aims to minimize variation and improve the quality of methods and processes by identifying and optimizing the influential factors (also called parameters or control factors) that affect method or process performance. The first step in the Taguchi method is to identify the key factors that influence the value of the product or process. Once the control factors are identified, the next step is to design a set of experiments to systematically study the effects of these factors on the response variable (the quality characteristic being optimized). The Taguchi method typically uses orthogonal arrays, which allow for a relatively small number of experiments to be conducted while still providing robust and reliable results. Orthogonal arrays are structured matrices that ensure a balanced and efficient allocation of experimental runs across the different combinations of control factors. The S/N ratio measures the deviation of the response variable from the target value relative to the variability in the process. After conducting the experiments and collecting the data, statistical analysis techniques are used to analyze the results and identify the optimal levels of the control factors that

minimize variation and maximize the S/N ratio. This often involves techniques such as analysis of variance (ANOVA) to determine the criticality of the factors and their interactions. In the current study, input factors and levels have been used to create Taguchi experiments using Minitab 16 software. Two factors namely, the shape of the VGs and the ambient condition, with three levels each are taken for optimizing output response. Fig. 6.5 and Table 6.2 depict the flowchart of Taguchi analysis, and input parameters along with their levels respectively.

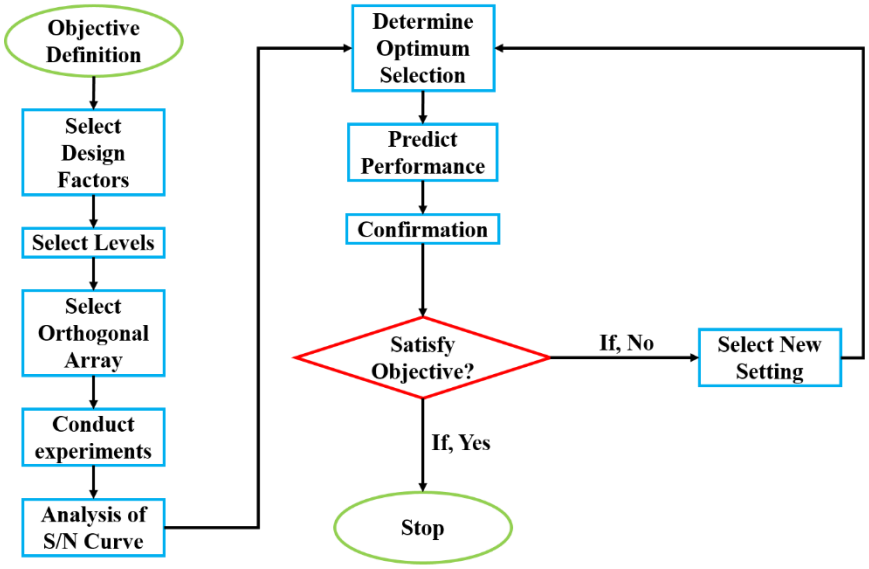

Fig. 6.5 Taguchi flowchart

Table 6.2: Input factors and levels for the Taguchi method

Factor	**Input Parameter**	**Levels**		
A	Shape of the VG	Delta	Envelope	Fishtail
B	Ambient HTC (W/m^2K)	5	15	25
Objective function	Thermal Enhancement Factor (TEF)			

In the present study, the output response is required to be as large as possible. Hence the criteria chosen here is larger is better. Under such circumstances, the following correlation is deployed:

$$\frac{S}{N}\text{HB} = -10\log\left(1/n\sum_{i=1}^{n}\frac{1}{Y_i^2}\right) \tag{6.17}$$

While the Reynolds number is a critical parameter for fluid flow, its well-established effects are extensively documented in prior research. Including it as a variable would redundantly increase the number of experimental runs and computational cost without providing novel insight. This study instead focuses its analysis on the less-explored, critical factors of vortex generator geometry and ambient heat transfer coefficient to efficiently isolate their unique impact on thermohydraulic performance.

6.4 Artificial Neural Network

In the present study, ANN has been employed using MATLAB 16 software. Artificial neural networks (ANNs) in MATLAB work by simulating the behavior of biological neural networks to solve various computational tasks, such as pattern recognition, classification, regression, and optimization. Leveraging its strength in discerning intricate patterns, the Artificial Neural Network (ANN) was employed to process the dataset through a structured pipeline. This involved training the model to recognize underlying relationships, validating its parameters to prevent overfitting, and finally testing its predictive accuracy on a separate subset of data to evaluate its generalization capability. A suitable ratio of training, validating, and testing data set is used to acquire the maximum value of the coefficient of determination (R^2), which represents better predictability of the ANN model.

6.5 Results and Discussion

6.5.1 Numerical Analysis

Figs. 6.6 (a-c) show the temperature profile for the delta, envelope, and fishtail VGs arranged in a uni-array manner in the rectangular channel. Figs. 6.6 (a-c) show profiles for vertical and horizontal midplanes. Vortex generators are observed to have a significant influence on the temperature of air flowing in a rectangular channel. By introducing vortices into the flow, the VGs enhance the heat transfer between the air and the channel walls. This is typically achieved by promoting better mixing of the air, which helps to diminish the boundary layer thickness and increase convection. As a result, the temperature of the air tends to decrease more rapidly as it moves through the channel, leading to improved thermal performance. Additionally, vortex generators can help to reduce flow separation. Furthermore, Figs. 6.7 (a-c) showcase the pressure profiles for the delta, envelope, and fishtail VGs arranged in a uni-array manner in the rectangular channel. Vortex generators tend to induce local pressure variations along with themselves, leading to changes in pressure distribution. From Figs. 6.7 (a-c), it is clear that the first VG creates a region of higher pressure drop. Moreover, they influence the overall pressure drop across the channel, primarily aiming to enhance flow mixing and heat transfer. However, their impact on pressure can vary; they may delay flow separation and reattachment, increase pressure losses, develop controlled airflow patterns, depending on the vortex generator geometry, and improve overall flow performance. Ultimately, the effect of VGs on air temperature and pressure in a rectangular channel is complex, influenced by factors like design, placement, and airflow characteristics. The temperature is predominantly uniform in the upper section of the channel (Figs. 6.8 (a-c)). The bottom region near the vortex generators shows slight temperature variations because the vortex generators induce localized mixing. Slight cooling effects are observed near the last

vortex generator (small blue/green region). This suggests an enhancement in heat transfer due to increased turbulence. Temperature reduction is subtle, implying that while the vortex generators enhance heat transfer, the flow is still dominated by the high-temperature inlet condition.

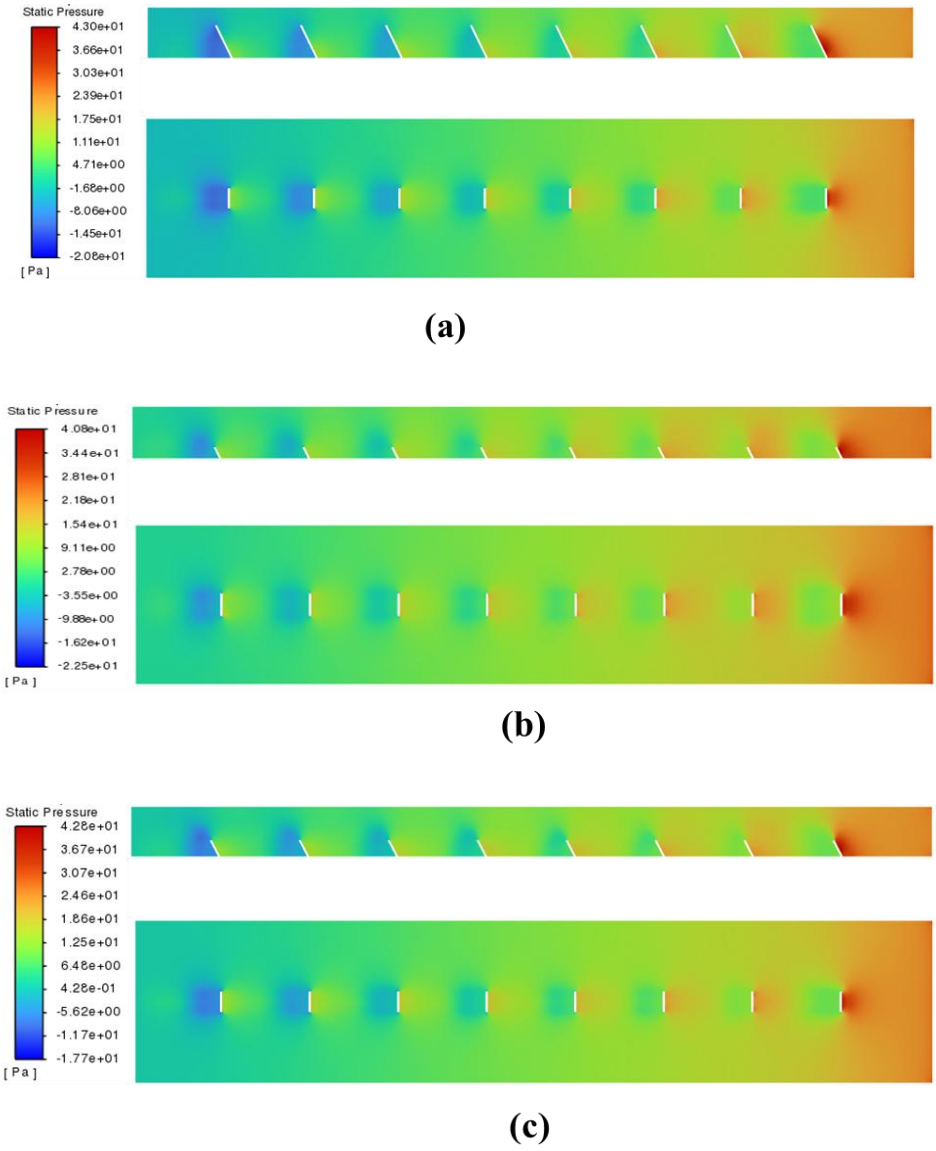

Fig. 6.6 Pressure contours for (a) Delta VG, (b) Envelope VG, and (c) Fishtail VG

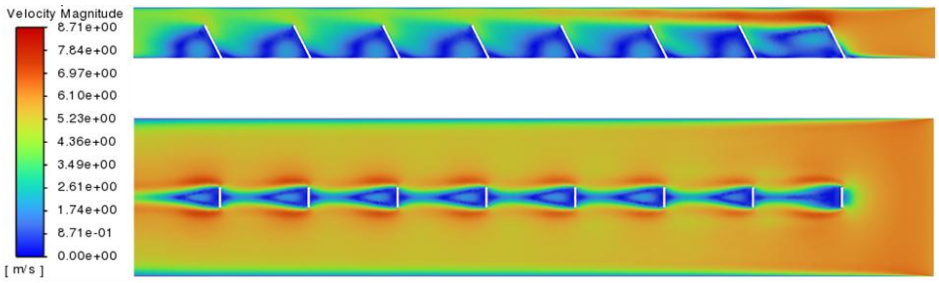

(a)

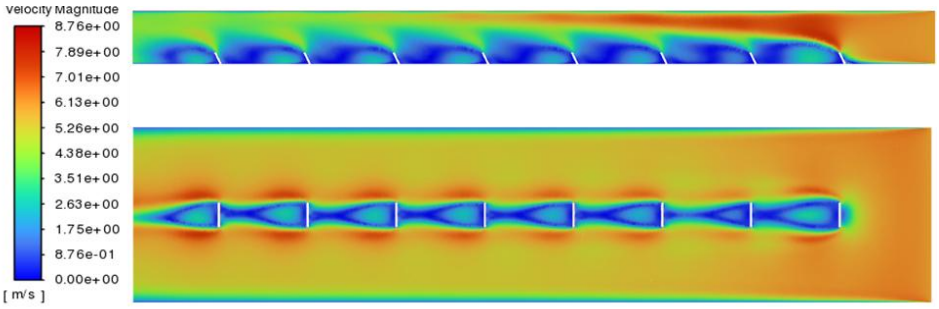

(b)

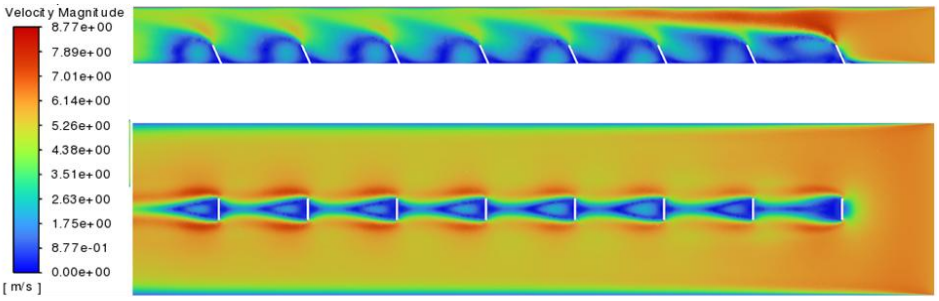

(c)

Fig. 6.7 Velocity contours for (a) Delta VG, (b) Envelope VG, and (c) Fishtail VG

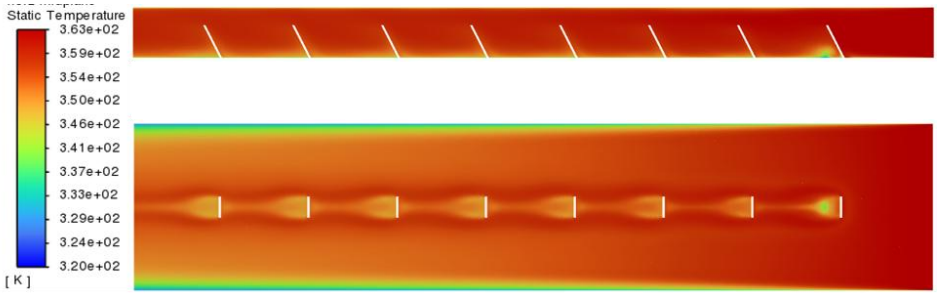

(a)

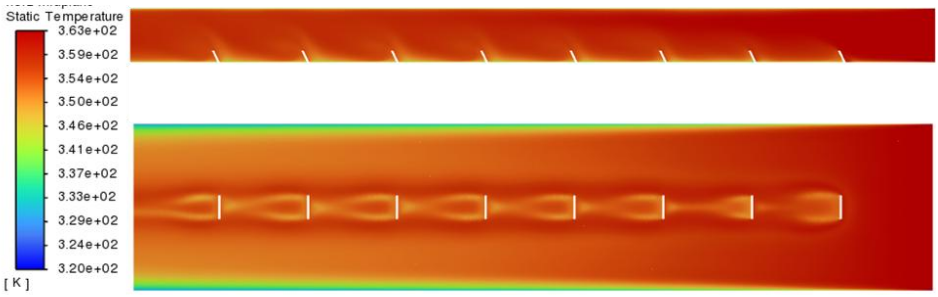

(b)

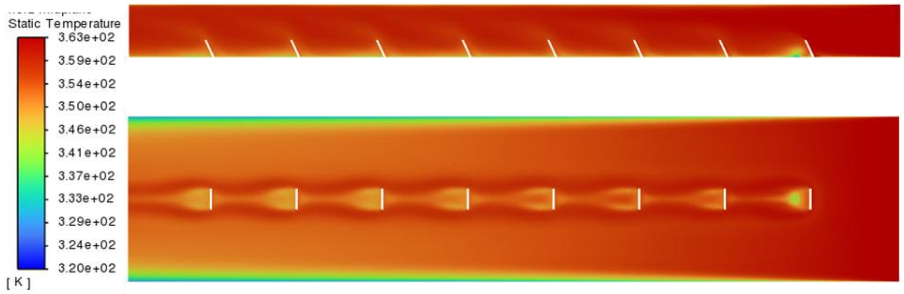

(c)

Fig. 6.8 Temperature contours for (a) Delta VG, (b) Envelope VG, and (c) Fishtail VG

6.5.2 Heat transfer capability

Figs. 6.9 (a-d) shows the variation of the heat transfer coefficient for different conditions. The impact of different ambient conditions (varying ambient HTC) has been studied in Figs. 6.9 (a-c). Three different configurations of VGs have been investigated for their heat transfer capabilities in comparison to that of a smooth rectangular channel. It is seen in Figs. 6.9 (a-c) that the HTC increases after every consecutive computational domain. For all the cases, the channels with VGs exhibit a higher value of *h* than the ones without the VGs. Quantitatively, the heat transfer coefficient value at the outlet increases by 2.797, 2.777, and 2.834 times for DVG, MVG, and FVG respectively as compared to the inlet for h=25W/m^{2}K. Similarly, for h=15W/m^{2}K, *h* raises by 2.801, 2.783, and 2.838 times at the outlet when compared to the parameter value at the inlet. For h=5W/m^{2}K, these values are 2.785, 2.766, and 2.566 for DVG, MVG, and FVG respectively. This

happens because, VGs enhance heat transfer by increasing turbulence, promoting mixing of fluid flow, and delaying boundary layer separation. Vortex generators introduce turbulence into the flow, which helps break up the boundary layer. Boundary layer separation can lead to reduced heat transfer efficiency as it creates stagnant regions where heat exchange is limited.

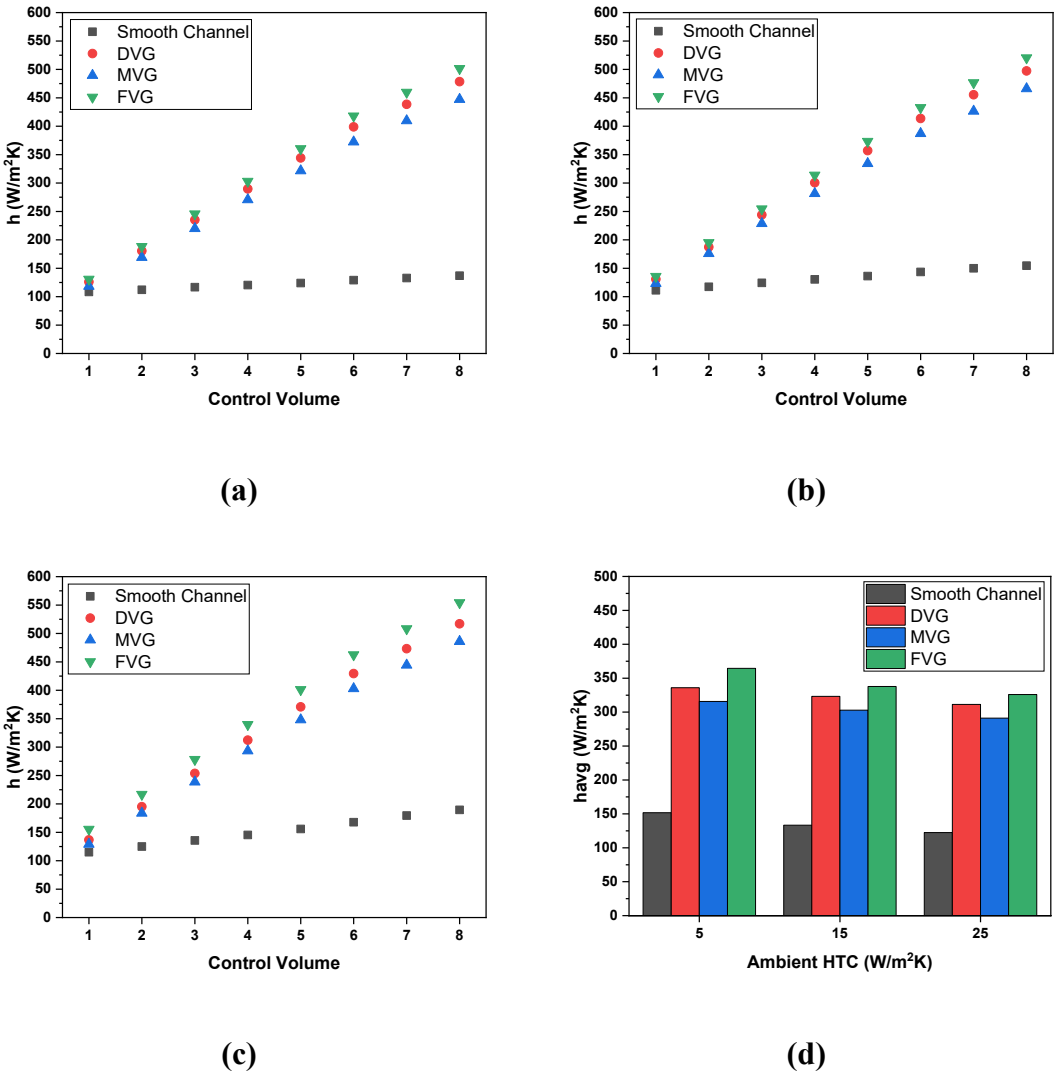

Fig. 6.9 Variation of (a) heat transfer coefficient in computational domains for h=25W/m²K, (b) h=15W/m²K, (c) h=5W/m²K and (d) Average heat transfer coefficient for different ambient conditions

By delaying separation, vortex generators ensure that the flow remains attached to the surface for longer, maximizing heat transfer. By increasing turbulence, promoting

mixing, and delaying boundary layer separation, vortex generators effectively increase the heat transfer coefficient. This means that for a given temperature difference between the fluid and the surface, more heat is transferred per unit area and per unit time. Out of all these, the maximum heat transfer coefficient is exhibited by FVG with a value of 554.17W/m^{2}K for h=5W/m^{2}K.

However, it is also observed that as the ambient heat transfer coefficient increases, the internal coefficients decrease, owing to the cooling effect of higher ambient heat transfer coefficients. This is evident from Figs. 8 (a-c). A higher ambient heat transfer coefficient causes greater heat dissipation and reduced external thermal resistance. The above fact is also evident from Fig. 6.9 (d) where a decrement in the average ***h*** is observed as the ambient heat transfer coefficient increases. It shows the variation of the average heat transfer coefficient for smooth channel, DVG, MVG, and FVG against different values of ambient heat transfer coefficient. The impact of ambient HTC can be observed here, for instance at h=25W/m^{2}K, 15W/m^{2}K, and 5W/m^{2}K, the average internal heat transfer coefficients for the smooth channel are 122.475W/m^{2}K, 133.4W/m^{2}K, and 151.687W/m^{2}K respectively. For h=25W/m^{2}K, the average HTC for DVG, MVG, and FVG incorporated channels are 154.26%, 137.7%, and 166.13% higher than that of the smooth channel. When the ambient condition is studied at h=15W/m^{2}K, this increment is found to be 142.28%, 127.07%, and 153.18% for DVG, MVG, and FVG respectively. Furthermore, the parameter value increases by 121.51%, 108.14%, and 140.33% for DVG, MVG, and FVG respectively, against the smooth channel for h=5W/m^{2}K. Thus, the vortex generators exhibit great heat transfer enhancement with their incorporation in the smooth channel. In summary, the decrease in the internal HTC when the external heat transfer coefficient increases is a consequence of the changing balance of thermal resistances within the system, with the reduction in external thermal resistance playing a

more significant role. Nevertheless, the maximum average HTC is shown by the Fishtail VG with a value of 501.57W/m^{2}K, 520.37W/m^{2}K, and 554.18W/m^{2}K for h=25W/m^{2}K, 15W/m^{2}K, and 5W/m^{2}K. Nevertheless, the results show that the internal HTC is sensitive to the VG shape and ambient conditions.

6.5.3 Impact on pressure drop

Fig. 6.10 depicts the manner of the pressure drop along the computational domains or length of the channel in smooth and DVG, MVG, and FVG-incorporated rectangular channels. It is seen from the Fig. that the pressure drop decreases along the length of the channel for all the configurations. The pressure drops by 84.94%, 92.42%, 91.39%, and 89.44% for the smooth-, DVG-, MVG-, and FVG-incorporated channels. Thus, higher pressure drop is observed in channels with vortex generators. This is because of increased turbulence, energy dissipation, boundary layer effect, flow obstruction, and development of secondary flow. Turbulence causes more frictional losses as the fluid moves through the channel, resulting in a higher pressure drop. The creation of vortices requires energy. This energy is taken from the flow, leading to a reduction in kinetic energy and an increase in pressure. The vortices themselves also dissipate energy as they interact with the fluid, further contributing to pressure loss. Furthermore, VGs disrupt the boundary layer of the fluid flowing over the channel walls. This disruption increases mixing and promotes heat transfer, but it also affects the flow profile and increases shear stresses at the channel walls. This results in higher frictional losses and consequently, a higher pressure drop along the channel. It is commendable that the change in ambient conditions does not affect the pressure drop. In quantitative terms, the highest pressure occurs for the DVG arrangement, followed by MVG, FVG, and the smooth channel. The smooth channel will have the least pressure drop due to the absence of any obstruction to the flow. The

maximum value of pressure drops exhibited by the smooth channel, DVG-, MVG-, and FVG- arrangements are 1.042Pa, 2.704Pa, 2.622Pa, and 2.533Pa.

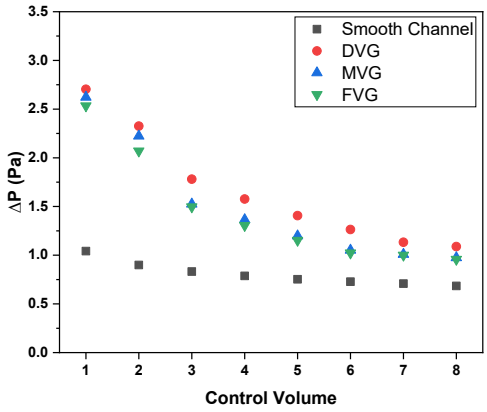

Fig. 6.10 Pressure drop variation along the channel

The reason for this observation can be understood with the help of Fig. 6.11. As seen from the diagram, DVG creates vortices all along its height, MVG creates vortices on the sides as well as the top V-notch, and FVG- also creates a vortex in the top V-notch region. Even though all their cross-section areas are the same, DVG possesses greater height than the MVG and hence its domain of influence increases. On the other hand, the side cuts of the FVG allow a smoother flow of the vortex generator when compared to the MVG.

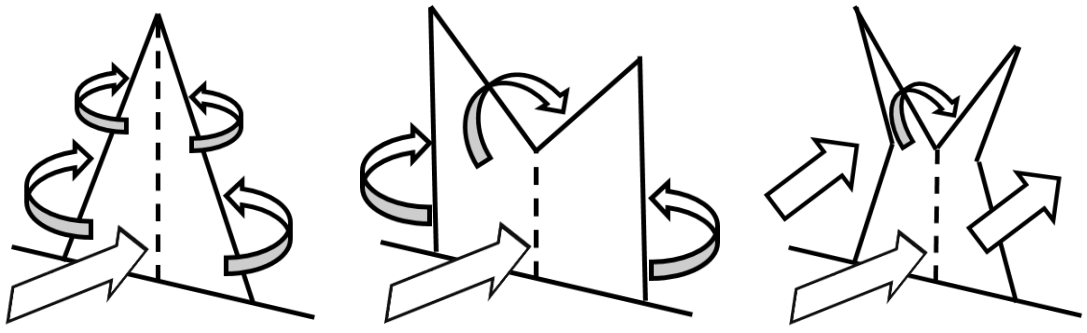

(a) **(b)** **(c)**

Fig. 6.11 Vortices in different VGs

6.5.4 Thermal Enhancement factor

Fig. 6.12 shows the variation of TEF for different conditions. The impact of different ambient conditions (varying ambient heat transfer coefficient) has been studied in Fig. 6.12 (a-c). Three different configurations of VGs have been investigated for their heat transfer capabilities in comparison to that of a smooth rectangular channel. In Fig. 6.12 (a-c), the horizontal dashed line depicts the TEF for a smooth channel which always acquires the value of 1. From Figs. 6.12 (a-c), it can be easily observed that the TEF increases consecutively for computational domains. The parameter exhibits greater than 1 value for all the computational domains except the first one. The obvious explanation for this is high pressure drop which occurs as a result of the first-time interaction of air with an obstruction in the form of a vortex generator. Subsequently, the Nusselt number upsurges while the pressure drop dwindles. The TEF increases by 2.54, 2.61, and 2.65 times for DVG, MVG, and FVG, respectively, from inlet to outlet at h=25W/m^{2}K. For h=15W/m^{2}K, the gains in TEF are 2.22, 2.91, and 2.32 for DVG, MVG, and FVG, respectively. The parameter value for the ambient condition of h=5W/m^{2}K mounts up by 1.7, 1.76, and 1.61 times for DVG, MVG, and FVG, respectively. The reasons behind this increment are turbulence enhancement, heat mixing, convection augmentation, and delayed boundary layer separation. Enhanced turbulence results in more efficient heat transfer by diminishing the thermal boundary layer and increasing the heat transfer coefficient. The vortices generated by vortex generators induce the mixing of the fluid, bringing hotter fluid from the core of the channel closer to the channel walls and vice versa. This mixing helps distribute heat more evenly across the channel cross-section, reducing the occurrence of hot spots and promoting more effective heat transfer. By increasing fluid motion and mixing, vortex generators enhance convective heat transfer, leading to improved heat dissipation from the channel walls. Furthermore, boundary layer

separation can lead to reduced heat transfer effectiveness. By delaying separation, vortex generators ensure that the flow remains attached to the channel wall for longer, maximizing heat transfer. The highest values are exhibited by the FVG incorporated channel, which are 3.278, 3.011, and 2.614 for h=25, 15, and 5W/m^{2}K, respectively.

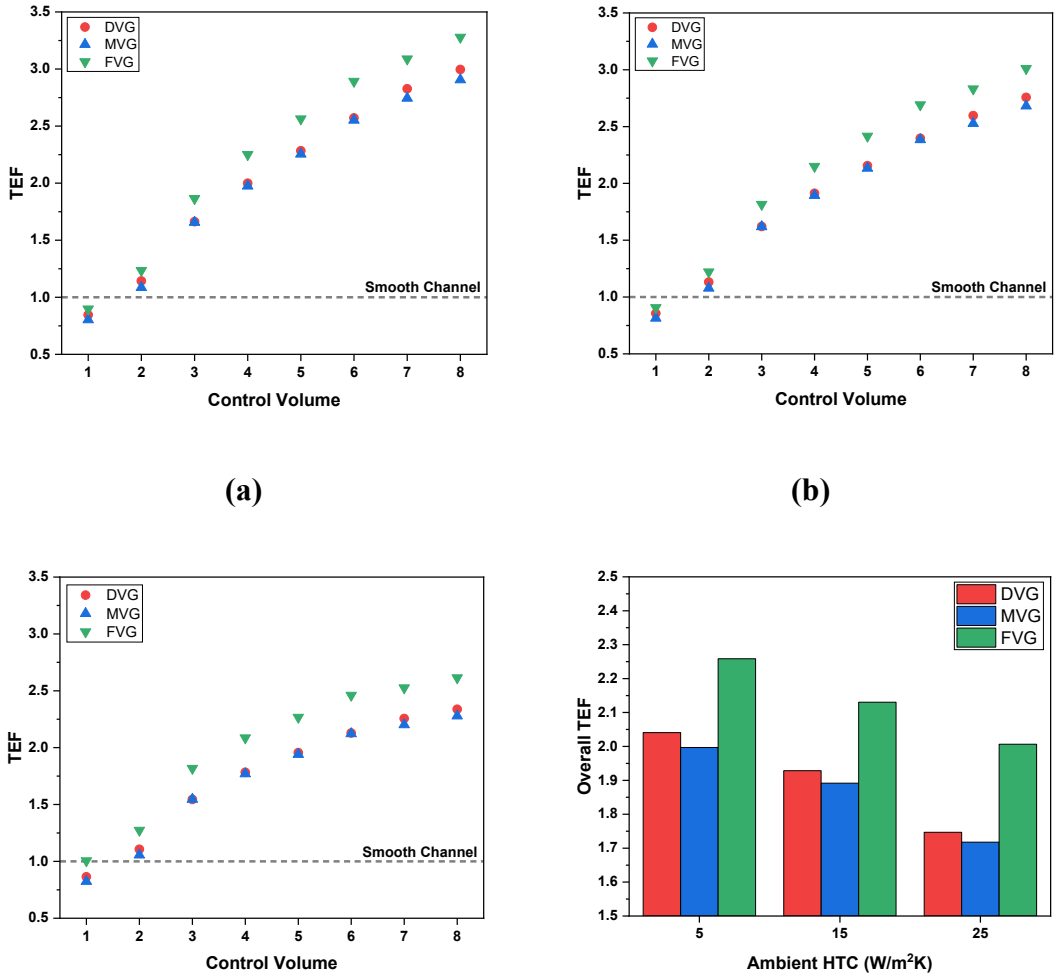

Fig. 6.12 Variation of (a) TEF in computational domains for h=25W/m^{2}K, (b) h=15W/m^{2}K, (c) h=5W/m^{2}K, and (d) Average TEF for different ambient conditions

Fig. 6.12 (d) shows the overall TEF across the channel. For h=25W/m^{2}K, the average TEF for DVG, MVG, and FVG incorporated channels are 104.1%, 99.69%, and 125.8% higher than that of the smooth channel. When the ambient condition is

studied at h=15W/m^{2}K, this increment is found to be 192.28%, 127.07%, and 153.18% for DVG, MVG, and FVG respectively. Furthermore, the parameter value increases by 121.51%, 108.14%, and 140.33% for DVG, MVG, and FVG respectively, against the smooth channel for h=5W/m^{2}K.

6.5.5 S/N ratio analysis

In the current study, the TEF (thermal enhancement factor) has been identified as the key factor as it incorporates both thermal and frictional aspects of the fluid flow. The optimization aimed to achieve the highest value of TEF. The optimization design uses L_9 orthogonal array which is described in Table 6.3.

Table 6.3: Designed L_9 orthogonal array (3^2) and the resulting TEF and S/N ratio values

Run	Factor		TEF	S/N
	A	B		
1	D	5	2.041	6.197
2	D	15	1.928	5.702
3	D	25	1.747	4.846
4	M	5	1.997	6.007
5	M	15	1.892	5.538
6	M	25	1.718	4.7
7	F	5	2.258	7.074
8	F	15	2.130	6.568
9	F	25	2.006	6.047

The S/N ratio values obtained after the utilization of the Taguchi method of the combinations obtained from the design of experiments are shown in Fig. 6.13. A higher value of the S/N ratio depicts more sensitivity of the objective function to that factor. The highest value of signal-to-noise ratio is exhibited by the factors A3 (fishtail VG), and B1 ($h=5W/m^2K$) out of the 9 runs. Table 6.4 shows the mean S/N ratio values as well as the rank obtained by the factors. It ranks the shape of the VG as first and the ambient HTC as second. This means that the shape of the VG had a greater influence on the thermohydraulic performance of the channel. However, if closely observed, the mean values obtained by the shape of the VGs are very close to that of the ambient HTC. This means, that even though the shape of the VGs stands first to the ambient HTC, the latter is as effective a factor as the former.

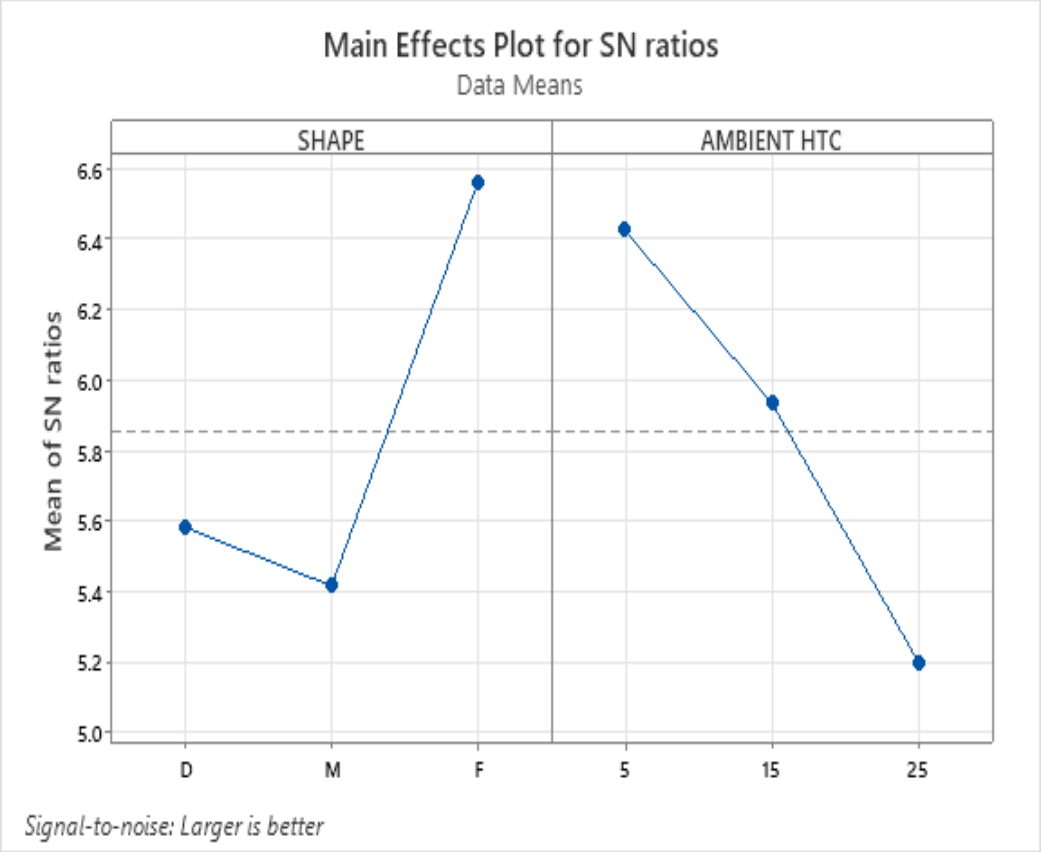

Fig. 6.13 SN ratios plot

Table 6.4: Response Table: for Signal-to-Noise Ratios

Criteria: Larger is better		
Level	**Shape**	**Ambient HTC**
1	5.582	6.426
2	5.415	5.936
3	6.563	5.198
Rank	**1**	**2**

Table 6.5: Analysis of Variance for SN Ratios

Source	DF	Seq SS	Adj SS	Adj MS	F	P
SHAPE	2	2.30706	2.30706	1.15353	103.87	0.003
AMBIENT HTC	2	2.29517	2.29517	1.14759	103.34	0.008
Residual Error	4	0.04442	0.04442	0.01111	-	-
Total	8	4.64666	-	-	-	-

In ANOVA (Analysis of Variance), the same can be predicted with the help of p-values. A small p-value (typically less than 0.05) implies that the observed differences in the means are likely not due to random chance alone, providing evidence in favor of the alternative hypothesis. In the context of the Taguchi method, this suggests that the factors being studied have a significant effect on the response variable. Table 6.5 exhibits that both factors acquire a value less than 0.05, implying that both parameters are critical to the performance of the channel. However, a smaller value means the greater influence of that factor, which again is owned by the shape of the VG.

6.5.6 Artificial Neural Network (ANN) model

In the current study, a two-layer feedforward network with sigmoid hidden neurons (with layer size 20) has been deployed (Fig. 6.14). To improve the predictability of the ANN model, the level of Factor B in the Taguchi method is increased from 3 to 21 levels in which the number of cases becomes 63 (=3x21). The range of the factor B remains the same but the values are taken at the interval of 1 i.e., 5,6,7…25W/m^{2}K. For the present ANN model, the data ratio used is 70:15:15 for training, validation, and testing. Thus, the overall model comprises of input, two hidden layers, and the output. The hidden layer used a sigmoid function for stimulation.

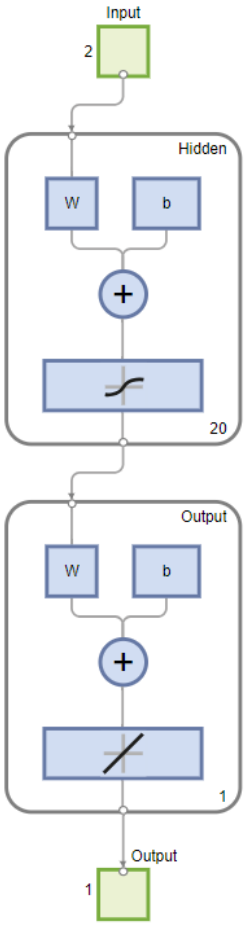

Fig. 6.14 Neural network visualization

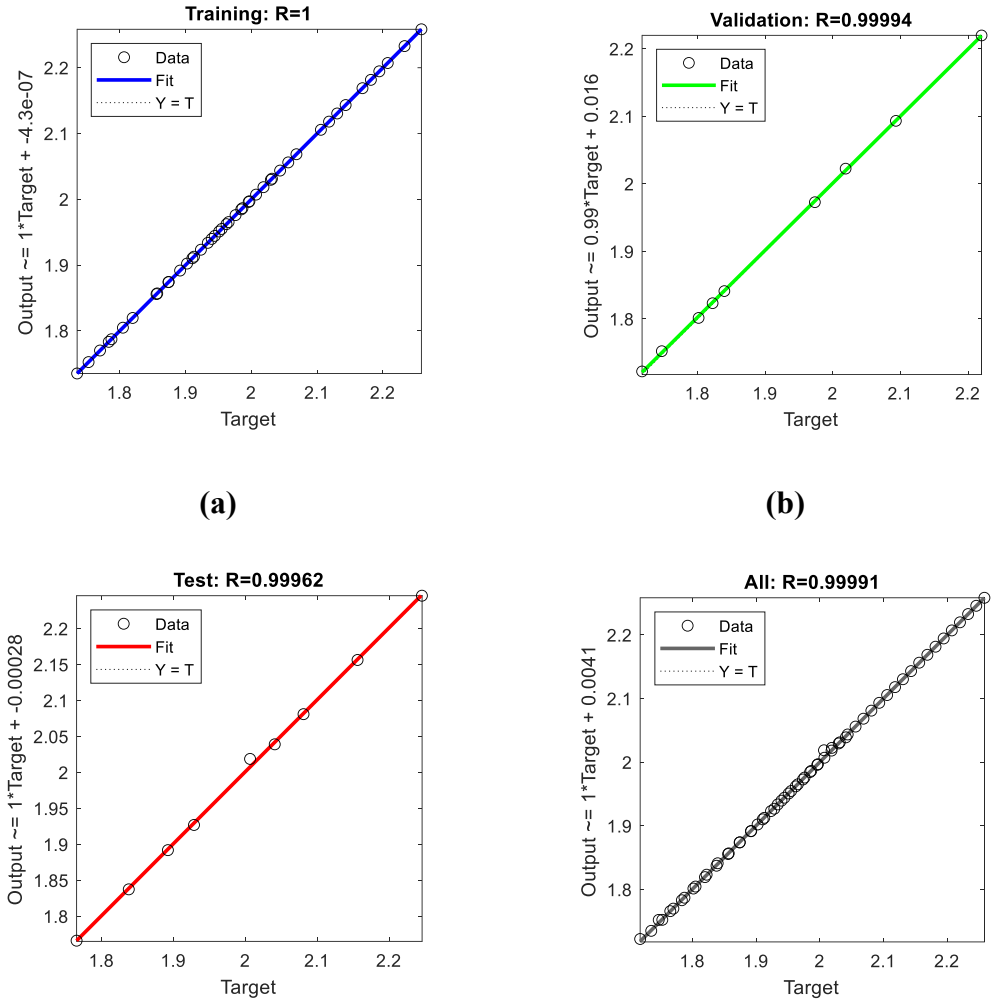

Fig. 6.15 (a-d) Prediction by ANN model for training, validation, and testing

The data division was taken randomly and the Levenberg-Marquardt training algorithm has been used along with mean-squared error performance. With 20 neurons in the hidden layer and 1 in the output layer, predicting fit quality (R^2) of 1, 0.99994, and 0.99962 (Figs. 6.15(a-d)). Hence, the present model configuration has very high prediction efficiency and can be used for similar computational problems.

6.6 Highlights

This work is aimed at numerically studying different geometries of vortex generators under different ambient conditions to ascertain the thermohydraulic

effectiveness of the VGs and carry out a comparative analysis. Various thermal and fluid flow parameters have been taken into consideration. Taguchi design-of-experiments is used to carry out the combinations of runs required for the analysis. The analysis of variance (ANOVA) and S/N ratios further helps in determining the optimum or the best factors for the outcome. Some salient features of the study are:

- Quantitatively, the heat transfer coefficient value at the outlet increases by 2.797, 2.777, and 2.834 times for DVG, MVG, and FVG respectively as compared to the inlet for h=25W/m^2K. Similarly, for h=15 W/m^2K, h raises by 2.801, 2.783, and 2.838 times at the outlet when compared to the parameter value at the inlet. For h=5W/m^2K, these values are 2.785, 2.766, and 2.566 for DVG, MVG, and FVG respectively.
- Out of all these, the maximum heat transfer coefficient is exhibited by FVG with a value of 554.17 W/m^2K for h=5W/m^2K.
- The pressure drops by 84.94%, 92.42%, 91.39%, and 89.44% for the smooth-, DVG-, MVG-, and FVG-incorporated channels.
- The highest TEF values are exhibited by the FVG incorporated channel, which are 2.258, 2.130, and 2.006 for h=25, 15, and 5W/m^2K, respectively.
- The highest value of signal-to-noise ratio is exhibited by the factors A3 (fishtail VG), and B1 (h=5 W/m^2K) out of the 9 runs.
- The machine learning ANN model gives the coefficient of determination value (R^2) of 1, 0.99994, and 0.99962 indicating high proficiency of the neural network.

Chapter 7

Solar Water Heater and TEG-based Hybrid System with Fishtail Vortex Generators

Overview: This chapter examines the performance of a hybrid system that combines an Evacuated U-tube Solar Water Heater (EUSWH) with a Thermoelectric Generator (TEG). To improve thermal and electrical efficiency, fishtail vortex generators (FVGs) are positioned on the hot side of the TEG module. The study explores how key operating factors, such as incident solar radiation intensity, water mass flow rate, inlet EUSWH temperature, and the presence of vortex generators, affect the performance of the EUSWH, TEG, and the overall system. The hybrid setup simultaneously provides heated water and electrical power, with vortex generators playing a crucial role in enhancing its overall effectiveness.

7.1 System description

Fig. 7.1 depicts the proposed EUSWH-TEG hybrid system. The hybrid system comprises an Evacuated U-tube Solar Water Heater (EUSWH), a Thermoelectric Generator (TEG), and the cold and hot channels. The cold water first enters the cold side of the TEG through the cold side channel. After this, the cold water goes into the solar water heater. The solar radiation falling onto the EUSWH heats the water, raising its temperature. This hot water then flows through the hot water channel after which it can be used for various purposes. The TEG is sandwiched between the cold and the hot channel. The temperature difference across the TEG results in an electric potential difference across its legs due to the Seebeck effect. Thus, electrical energy is also

produced along with the hot water. Q_{SUN} denotes the solar radiation received by the EUSWH in W. The ambient temperature is denoted by T_0. $T_{in,EUSWH}$, and $T_{out,EUSWH}$ denote the bulk temperature of water entering and leaving the EUSWH, respectively. $T_{in,cold}$, $T_{out,cold}$, $T_{in,hot}$, and $T_{out,hot}$ represent the bulk temperatures of water at the inlet of the cold channel, outlet of the cold channel, inlet of the hot channel, and outlet of the cold channel, respectively.

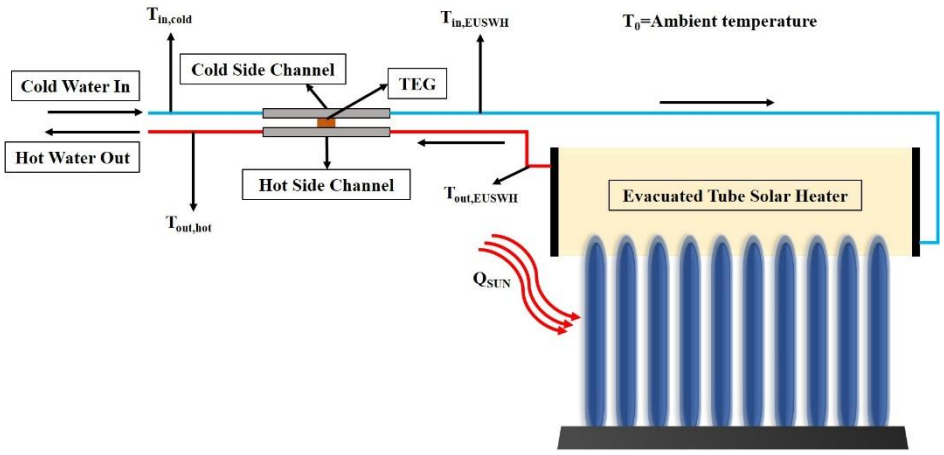

Fig. 7.1 EUSWH-TEG hybrid system schematic diagram

7.1.1 Evacuated U-tube solar water heater

The section view of a single U-tube is shown in Fig. 7.2. On the outside, the EUSWH embraces vacuum U-tubes in tandem and a tank for hot water storage.

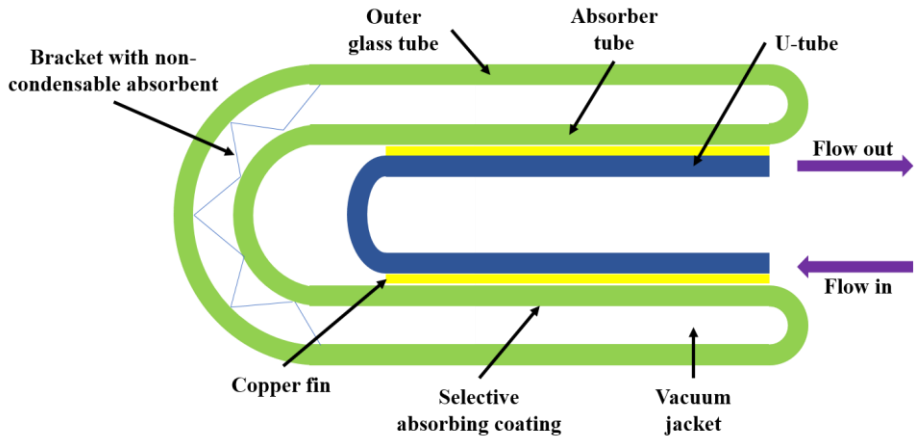

Fig. 7.2 Section view of a single U-tube of EUSWH

The U-tube contains a two-layer structure made of coated-vacuum glass tubes. The absorber tube is equipped with a selective coating on its surface, while the vacuum jacket minimizes conduction losses. Circular copper fins are used to attach or weld the tubes, facilitating the transport of solar energy captured by specialized absorptive coating to water flowing through the U-tube. The parameter values utilized in the EUSWH system are presented in Table 7.1. The EUSWH model has been developed using the Engineering Equation Solver code. To ensure a thorough analysis and simplify complex calculations without compromising accuracy, the following assumptions are made for the EUSWH system (Zhang et al., 2024):

- Heat transfer is considered one-dimensional and steady-state, with transient effects excluded.
- The heat resistance of the outer glass tube and its capacity to absorb solar irradiation are neglected.
- The working fluid's velocity within the tube is assumed to remain constant.
- The phase of the working fluid does not change.
- Heat losses within the vacuum layer are disregarded.

Table 7.1: Parameters used for the EUSWH

Parameter	Symbol	Value
Inner absorber tube's outer diameter	d_{SC}	0.047m
Inner absorber tube's effective length	L_{SC}	1.71m
Cross sectional area of the tube	A_t	1 x 10^{-3}m^2
Absorbing coating's absorptivity	α_a	0.9
Outer glass's light transmittance	τ	0.9
Number of tubes	N	36

Collector efficiency factor	F'	0.9
Ambient temperature	T_0	298K
Heat transfer coefficient at the fluid-tube wall interface	$h_{f,i}$	700W/m^{2}K

The EUSWH utilizes the solar irradiance falling onto it to heat the water which can be used for further purposes. The part of the solar energy absorbed by the EUSWH is called the useful solar energy Q_{EUSWH}. The Q_{EUSWH} is the difference between total incident solar energy and the heat lost to the environment (Q_E) and is given as follows:

$$Q_{EUSWH} = Q_{SUN} - Q_E = F_R\left[G \cdot \tau \cdot \alpha_a \cdot A_e - A_a \cdot U_L\left(T_{in,EUSWH} - T_0\right)\right] \quad (7.1)$$

Where F_R is the EUSWH's heat removal factor, G is the solar radiation, τ is the outer glass's light transmission, α is the selective coating's absorptivity, and U_L is the EUSWH's total heat loss coefficient. The areas A_e represents the effective heat absorption area of the absorber and A_a represents the outer surface area of the absorber (Zhang et al., 2024), and have been calculated as below:

$$A_e = N(1.43 d_{SC} \cdot L_{SC}) \quad (7.2)$$

$$A_a = N(\pi \cdot d_{SC} \cdot L_{SC}) \quad (7.3)$$

Where, d_{SC} and L_{SC} represent the outer diameter of the inner absorber tube, and the effective length of the inner absorber tube, respectively. The EUSWH's total heat loss coefficient, U_L (Zhang et al., 2024), has been determined as follows:

$$U_L = 0.003(T_i - T_0) + 0.89 \quad (7.4)$$

The EUSWH's heat removal factor is a function of the mass flow rate ($\dot{m}_w$) and heat capacity of water ($C_{p,w}$), the outer surface area of absorber tubes, EUSWH's heat loss coefficient, and the efficiency factor of the EUSWH (F'). It is calculated as follows:

$$F_R = \frac{\dot{m}_w \cdot C_{p,w}}{A_a \cdot U_L}\left[1 - \exp\left(-\frac{A_a \cdot U_L \cdot F}{\dot{m} \cdot C_{p,w}}\right)\right] \tag{7.5}$$

Where,

$$F' = \frac{\frac{1}{U_L}}{W\left[\frac{1 + \frac{U_L}{C_b}}{U_L[d + (W - d)F]} + \frac{1}{C_B} + \frac{1}{h_{f,i}}\right]} \tag{7.6}$$

$$\dot{m}_w = u_w \cdot \rho_w \cdot A_t \tag{7.7}$$

In the above equations, C_b, C_B, W, d, F, u_w, ρ_w, and A_t denote the integrated conductance, bond conductance, distance around the U-tubes, diameter of the U-tube, and efficiency standard for straight fins, flow velocity of water in tubes, density of water, and U-tube's cross-sectional area respectively. Furthermore, the useful solar energy and the bulk temperature of the water leaving the EUSWH can be calculated as follows:

$$Q_{EUSWH} = \dot{m}_w \cdot C_{p,w}\left(T_{out,EUSWH} - T_{in,EUSWH}\right) \tag{7.8}$$

$$T_{out,EUSWH} = T_{in,EUSWH} + \frac{F_R}{C_{p,w} \cdot u_w}\left[G \cdot \tau \cdot \alpha_a \cdot A_e - A_a \cdot U_L\left(T_{in,EUSWH} - T_0\right)\right] \tag{7.9}$$

Thus, with all the above parameters calculated, we can find the efficiency of the EUSWH which is defined as follows:

$$\eta_{EUSWH} = \frac{Q_{EUSWH}}{G \cdot A_e} \tag{7.10}$$

7.1.2 Thermoelectric Generator

A TEG comprises ceramic plates, solder, load resistance (R_L), and multiple sets of positive and negative thermoelectric legs (Fig. 7.3). The legs are connected electrically in series and thermally in parallel. Except at the junctions and ceramic plate and the channels, the TEG is electrically and thermally insulated elsewhere. As hot water flows through the hot water channel, it heats the ceramic plate of the TEG. The temperature

difference across the thermoelectric elements causes electricity generation due to the Seebeck effect. To enhance research efficiency, streamline intricate calculations, and ensure accuracy, the TEG system is based on the following assumptions (Shen et al., 2016):

- The EUSWH and TEG operate in steady states.
- The Thomson effect in thermoelectric elements of the TEG is neglected, and electric current is assumed to flow past the device's arm uninterrupted.
- The average Seebeck coefficient of the TEG is treated as constant at a uniform temperature.

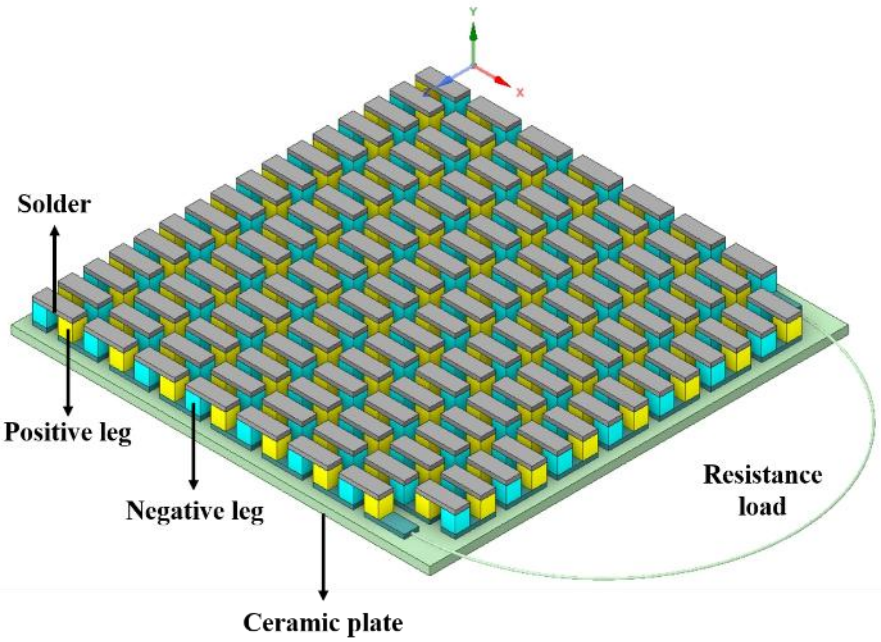

Fig. 7.3 TEG with its components

The properties of the commercially available Bi_2Te_3 and the TEG leg geometry description are given in Table 7.2 where l_{TEG}, b_{TEG}, and h_{TEG} denote the length, breadth, and height of the TEG leg, respectively. Bi_2Te_3 is a widely used thermoelectric material recognized for its advanced development and excellent reliability. Its suitable temperature range corresponds closely to the operating range of the EUSWH, making it a preferred

option for the thermoelectric elements. The choice of material for the ceramic plates and the solder are aluminum oxide and copper respectively. The channels and the TEG have been numerically simulated on ANSYS 2022R2.

Table 7.2: Thermoelectric properties of Bi_2Te_3 and leg dimensions (Zhang et al., 2024)

Property	Expression
Seebeck coefficient (V/K)	$\alpha_p(T) = 5.921376 \times 10^{-13}T^3 - 3.274207 \times 10^{-9}T^2 + 2.422355 \times 10^{-6}T - 2.743842 \times 10^{-4}$
	$\alpha_n(T) = 1.291689 \times 10^{-13}T^3 + 1.074408 \times 10^{-9}T^2 - 9.271759 \times 10^{-7}T + 8.958888 \times 10^{-6}$
Electrical conductivity (S/m)	$\sigma_p(T) = [2.248899 \times 10^{-14}T^3 - 1.250867 \times 10^{-10}T^2 + 1.388189 \times 10^{-7}T - 2.244786 \times 10^{-5}]^{-1}$
	$\sigma_n(T) = [-1.24614 \times 10^{-14}T^3 - 6.429015 \times 10^{-11}T^2 + 9.103036 \times 10^{-8}T - 1.049646 \times 10^{-5}]^{-1}$
Thermal conductivity (W/m^2K)	$k_p(T) = 1.251606 \times 10^{-7}T^3 - 1.242845 \times 10^{-4}T^2 + 3.873788 \times 10^{-2}T - 2.362707$
	$k_n(T) = -1.592653 \times 10^{-8}T^3 + 2.905845 \times 10^{-5}T^2 - 1.58323 \times 10^{-2}T + 3.727526$
$l_{TEG} = b_{TEG}$	1.4mm
h_{TEG}	1.6mm

Based on the above assumptions and parameters, the heat transfer on the hot side ($Q_{h,TEG}$), heat transfer on the cold side ($Q_{c,TEG}$), the power generated ($Power_{TEG}$), and the TEG efficiency (η_{TEG}) are given as follows:

$$Q_{h,TEG} = N\left[\alpha_{pn} I T_{h,TEG} + k_{pn}\left(T_{h,TEG} - T_{c,TEG}\right) - \frac{I^2 R_{pn}}{2}\right] \tag{7.11}$$

$$Q_{c,TEG} = N\left[\alpha_{pn} I T_{c,TEG} + k_{pn}\left(T_{h,TEG} - T_{c,TEG}\right) + \frac{I^2 R_{pn}}{2}\right] \tag{7.12}$$

$$Power_{TEG} = Q_{h,TEG} - Q_{c,TEG} = \alpha_{pn} I\left(T_{h,TEG} - T_{c,TEG}\right) - R_{pn} I^2 \tag{7.13}$$

$$\eta_{TEG} = \frac{Power_{TEG}}{Q_{h,TEG}} = \frac{\alpha_{pn} I\left(T_{h,TEG} - T_{c,TEG}\right) - R_{pn} I^2}{N\left[\alpha_{pn} I T_{h,TEG} + k_{pn}\left(T_{h,TEG} - T_{c,TEG}\right) - \frac{I^2 R_{pn}}{2}\right]} \tag{7.14}$$

7.1.3 Water flow channels

Fig. 7.4 shows the part of the hybrid system where thermoelectric generation comes into play. For the thermoelectric generator analysis, two configurations on the hot side of the TEG have been considered, viz. smooth channel and channel equipped with fishtail vortex generators (FVGs). The length, breadth, and height of the channel are 360mm x 70mm x 20mm, respectively. The channel and the VG material have been selected as aluminum due to its high thermal conductivity. The definition of the angle of inclination, the fishtail VG configuration, and the schematic of flow past the VG are shown in Fig. 7.5 (a-c). The thickness of the VG is 1mm while the angle of inclination selected is 60° as per the previous study.

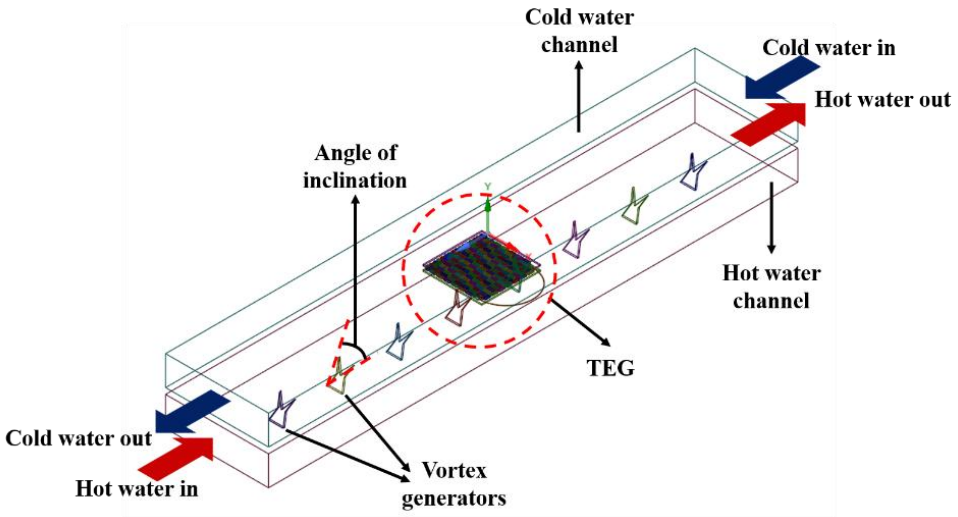

Fig. 7.4 TEG sandwiched between cold channel and hot channel (equipped with FVGs)

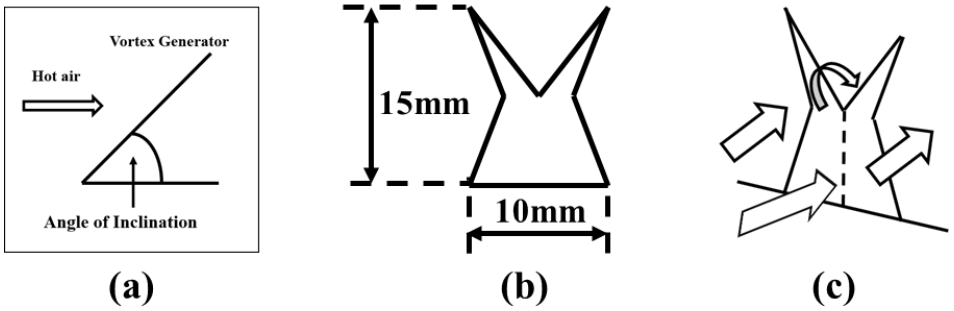

Fig. 7.5 (a) Angle of inclination, (b) FVG dimensions, and (c) FlowPast FVG

In this study, the considered hot air is treated as incompressible and continuous, and the simulations are conducted under stable states. The determination of the heat exchanger surface temperature is achieved through the application of conjugate heat transfer Eqs. within the computational unit. The governing Eqs. are as follows:

Continuity Eq., $\frac{\partial}{\partial x_i}(\rho u_i) = 0$ (7.15)

Momentum Eq., $\frac{\partial}{\partial x_i}(\rho u_i u_k) = \frac{\partial}{\partial x_i}\left(\mu \frac{\partial u_k}{\partial x_i}\right) - \frac{\partial p}{\partial x_k}$ (7.16)

Energy Eq., $\frac{\partial}{\partial x_i}(\rho u_i T) = \frac{\partial}{\partial x_i}\left(\Gamma \frac{\partial T}{\partial x_i}\right)$ (7.17)

Here, ρ and μ represent density and dynamic viscosity, respectively. The diffusion coefficient Γ is defined as thermal conductivity divided by the specific heat ($\Gamma=k/Cp$). Eqs. (7.18) and (7.19) simulate turbulent flow using k-ε model.

$$\frac{\partial}{\partial x_i}(\rho k u_i) = \frac{\partial}{\partial x_j}\left[\left(\mu + \frac{\mu_t}{\sigma_k}\right)\frac{\partial k}{\partial x_j}\right] + G_k + G_b - \rho\epsilon - Y_M + S_k \quad (7.18)$$

$$\frac{\partial}{\partial x_i}(\rho \epsilon u_i) = \frac{\partial}{\partial x_j}\left[\left(\mu + \frac{\mu_t}{\sigma_\epsilon}\right)\frac{\partial \epsilon}{\partial x_j}\right] + C_{1\epsilon}\frac{\epsilon}{k}(G_k + C_{3\epsilon}G_b) - C_{2\epsilon}\rho\frac{\epsilon^2}{k} + S_\epsilon \quad (7.19)$$

Within this framework, G_k, G_b, and Y_M signify the creation of turbulence kinetic energy arising from the mean velocity gradient, buoyancy effects, and the involvement of fluctuating dilation in turbulence towards the comprehensive dissipation rate. The

constants $C_{1\epsilon}$, $C_{2\epsilon}$, and $C_{3\epsilon}$ play a crucial role in these formulations. The turbulent viscosity, μ_t, is modeled as:

$$\mu_t = \rho C_\mu \frac{k^2}{\epsilon} \tag{7.20}$$

The production of k is defined by the following Eqs:

$$P_k = -\rho \overline{u_i' u_j'} \frac{\partial u_j}{\partial x_i} \tag{7.21}$$

$$P_k = \mu_t S^2 \tag{7.22}$$

Where the mean rate of strain tensor, S, is:

$$S \equiv \sqrt{2 S_{ij} S_{ij}} \tag{7.23}$$

7.1.4 Hybrid system

The overall hybrid system performance can be evaluated by ascertaining the hybrid system efficiency (η_{HS}). The TEG is responsible for the electrical power generation in the hybrid system, while the input to the hybrid system is free solar energy. Hence, the hybrid system efficiency is defined as (Zhang et al., 2024):

$$\eta_{HS} = \frac{Power_{TEG}}{Q_{SUN}} = \frac{\alpha_{pn} I \left(T_{h,TEG} - T_{c,TEG}\right) - R_{pn} I^2}{G . A_e} \tag{7.24}$$

7.1.5 Validation and Grid Independence Test

The coupling of the EUSWH-TEG hybrid system has not been done experimentally before, thus the validation for the EUSWH-TEG hybrid system is provided in the current work. So, the model validation of EUSWH and TEG has been validated with experimental results. If the models of the EUSWH and TEG are reliable, then it can ensure that the present EUSWH-TEG hybrid system model has achieved a satisfactory level. In Fig. 7.6 (a) the variation of η_{EUSWH} with $(T_{in,EUSWH}-T_0)/G$ is

represented, while the voltage changes with the temperature difference have been illustrated in Fig. 7. 6 (b).

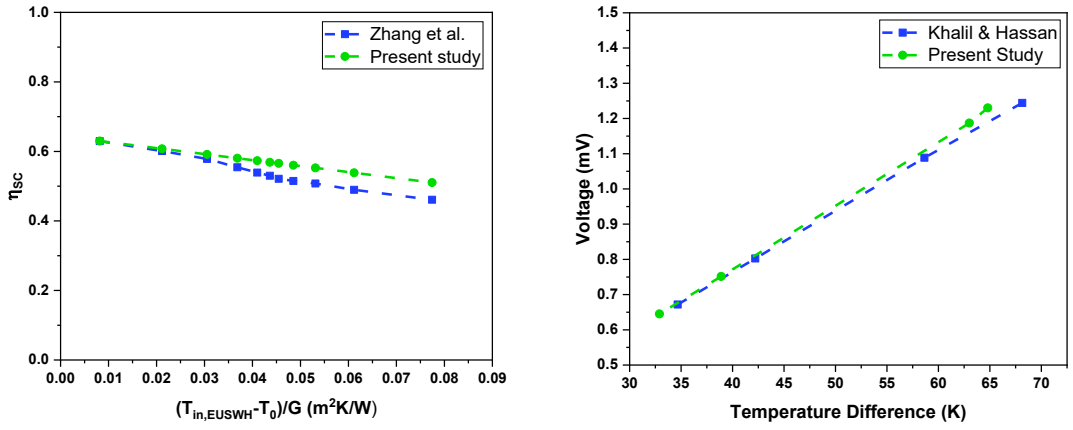

(a) **(b)**

Fig. 7.6 (a) Validation of present EUSWH with experimental results (b) Comparison of present numerical data and experimental work

In Fig. 7.6 (a), it is observed that the numerical model curve runs near the experimental study curve (Zhang et al., 2024). Furthermore, the maximum relative error calculated is 8.76%, suggesting the reliability of the EUSWH model. Also, Fig. 7.6 (b) represents the validation of the numerical model of TEG of the present study with that of an experimental one (Khalil and Hassan, 2020). The maximum discrepancy observed is 3.44%, depicting the high consistency of the current model. The limited deviation obtained in both validations might be the result of the assumption made before. The advantage of the study is, however, that it has been conducted within the same range as the validation, hence, the deviation will not exceed the maximum error value obtained.

The detailed simulations performed for the 3D TEG system require precise mesh generation to accurately evaluate the distributions of thermohydraulic and thermoelectric parameters. Various mesh sizes are applied to different regions within each computational domain to account for the complexities of VGs and TEG components. Due to the intricate

structure of VGs, a fine quad mesh is adopted for the fluid and plate regions, while an even finer quad mesh is used for the TEG domain, given its compact size and numerous contact points, as illustrated in Fig. 7.7.

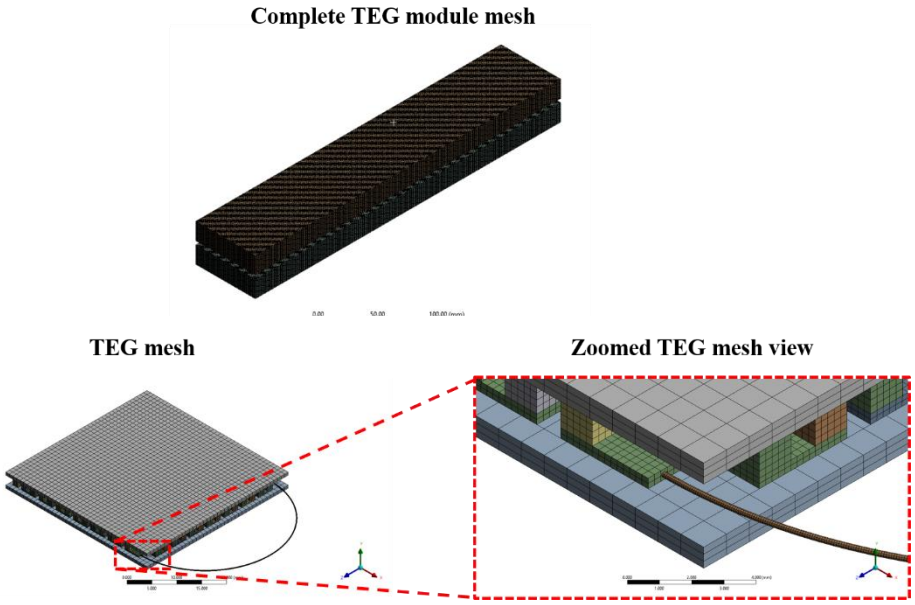

Fig. 7.7 TEG module meshing

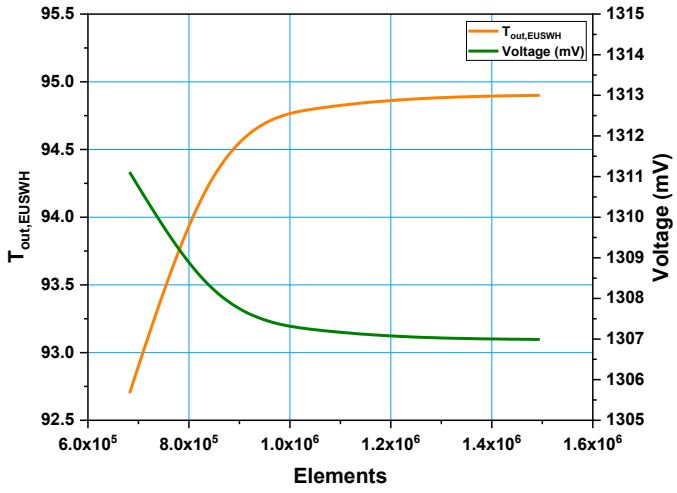

Fig. 7.8 Grid independency test

Four distinct grid configurations, ranging from 682,424 to 1,494,990 elements, were analyzed. Fig. 7.8 demonstrates that the grid configuration comprising 1,049,230

cells exhibits a relative variation of less than 1% in the outlet EUSWH temperature and TEG voltage compared to the configuration with the highest cell count (1,494,990). Consequently, for subsequent simulations, the grid configuration with 1,049,230 cells, or a closely similar setup, was chosen as the standard grid size, balancing computational efficiency and processing time.

7.2 Results and Discussion

The novel EUSWH-TEG hybrid system with the application of vortex generators in the system has been developed in the present study. This section comprises the analysis of performance metrics of the EUSWH, the TEG, and the EUSWH-TEG hybrid system. The performance metrics of the EUSWH studied include EUSWH's outlet temperature, useful solar energy, and EUSWH efficiency. Additionally, the TEG output parameters such as voltage, current, power, and TEG efficiency have been analyzed which also incorporates the impact of fishtail vortex generators (FVGs) employed in the hot water channel. Eventually, to scrutinize the hybrid system, its efficiency is evaluated. The study incorporates multi-dimensional input parameters for the comprehensive study of the hybrid system.

7.2.1 EUSWH performance

The EUSWH performance has been studied for the incident solar radiation (100-1000W/m^2), the mass flow rate of water (0.01-0.02kg/s), and EUSWH inlet temperature (303-313K). From Fig. 7.9 (a-c) it is observed that $T_{out,EUSWH}$ increases as the solar radiation and $T_{in,EUSWH}$ is raised. However, $T_{out,EUSWH}$ decreases as the mass flow rate input to the EUSWH is increased. The decrease in $T_{out,EUSWH}$ is more pronounced at higher values of solar radiation and low mass flow rate. It is also directly influenced by $T_{in,EUSWH}$. The reason behind this is simple to understand. Higher solar radiation means more energy

is available for heating the water. Solar radiation is the primary source of energy in the system. When solar radiation increases, the collector absorbs more energy, raising the temperature of the working fluid (water). The useful solar heat (Q_{EUSWH}) from the sun (Q_{SUN}) increases with solar radiation, leading to a higher outlet temperature (Kumar et al., 2021). The explanation is also supported by Eq. 7.8. A lower mass flow rate allows the water more time to absorb heat, increasing the outlet temperature. When the flow rate is reduced, the residence time of water in the collector increases. This longer duration allows the water to absorb more heat per unit mass. This is in good agreement with Eq. 7.8. A critical point to note here is that $T_{in,EUSWH}$ has a positive impact on $T_{out,EUSWH}$ than the mass flow rate at a particular incident solar radiation. For instance, at G=1000W/m^2, $T_{out,EUSWH}$ increases by 2.45% and 2.85% at mass flow rates of 0.01 and 0.02kg/s, respectively when the $T_{in,EUSWH}$ varies from 303-313K. However, it decreases by 4.57% and 4.2% at $T_{in,EUSWH}$ of 303 and 313K, respectively when mass flow rates are varied from 0.01-0.02kg/s.

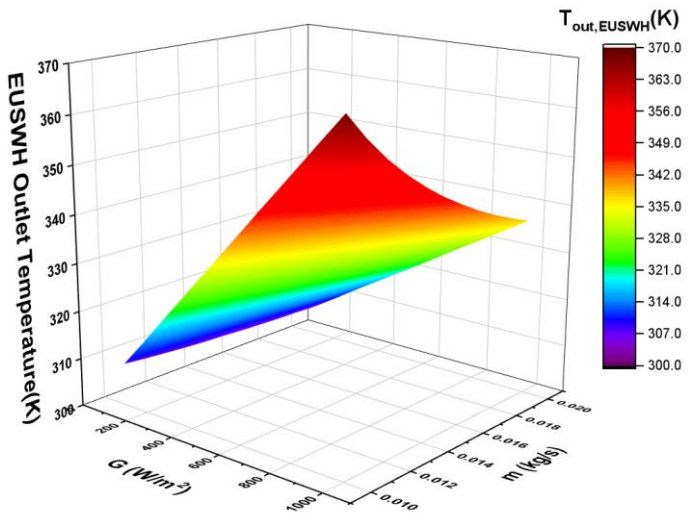

(a)

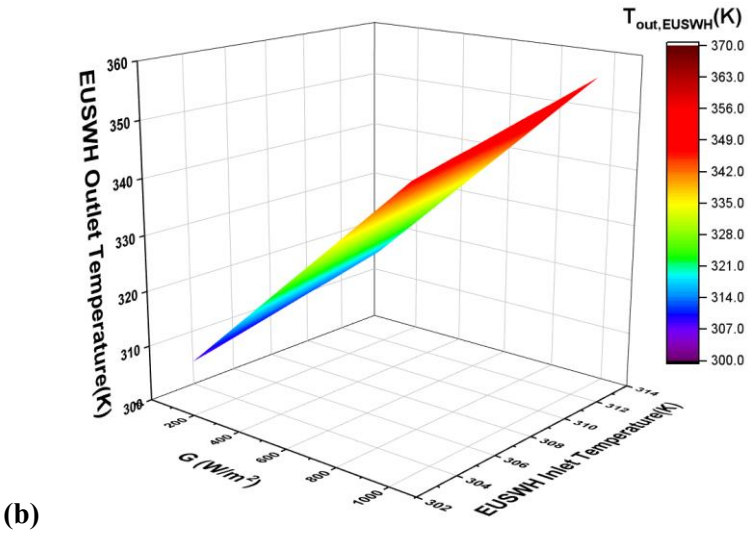

(b)

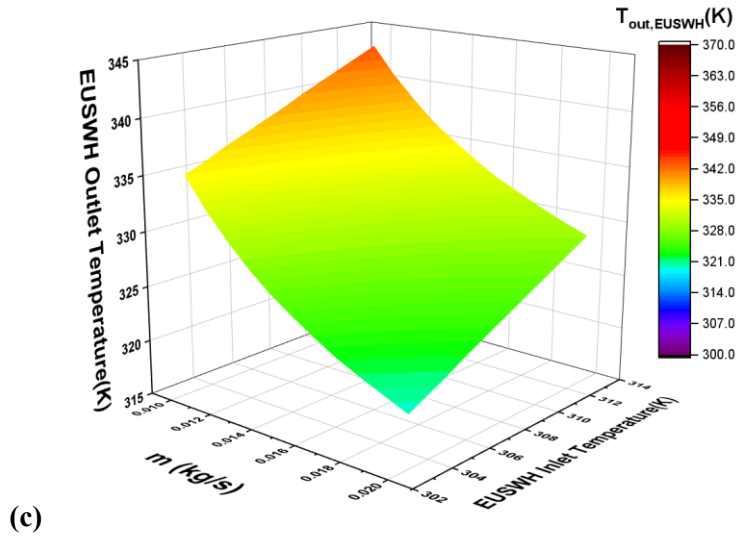

(c)

Fig. 7.9 (a-c) Effect of incident solar radiation, mass flow rate, and inlet EUSWH temperature on the outlet EUSWH temperature

The impact of incident solar radiation, water mass flow rate, and EUSWH inlet temperature on the useful solar energy or the solar energy absorbed by it can be seen in Fig. 7.10 (a-c). It is observed that Q_{EUSWH} increases with G. It is obvious that more incident radiation will upsurge the amount of solar energy being absorbed by the EUSWH. With the increase in the mass flow rate of water, a marginal increment in Q_{EUSWH} is observed. Q_{EUSWH} increases to some extent at high values of incident solar radiation, while at lower values of G, the increment is negligible, as the mass flow rate is varied. With the increase in $T_{in,EUSWH}$, the useful solar energy is decreased. This is because heat

transfer is a strong function of temperature difference. As inlet EUSWH temperature is increased, the heat transfer rate decreases due to decreased temperature difference. The highest achievable heat absorption rate is 1408 W at G=1000W/m^2, mass flow rate=0.02kg/s, and inlet EUSWH temperature=303K. At G=1000W/m^2, at the mass flow rate of 0.01kg/s, the Q_{EUSWH} decreases by 5.56%, while at 0.02kg/s, the decrement is 5.4% when $T_{in,EUSWH}$ is varied between 303 to 313K. However, at 303K and 313K, Q_{EUSWH} increases by 4.45% and 4.63%, respectively when the flow rate is varied from 0.01-0.02kg/s.

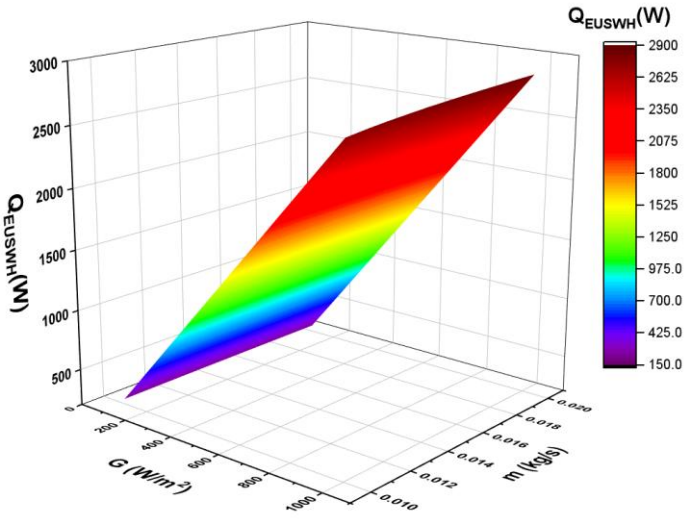

(a)

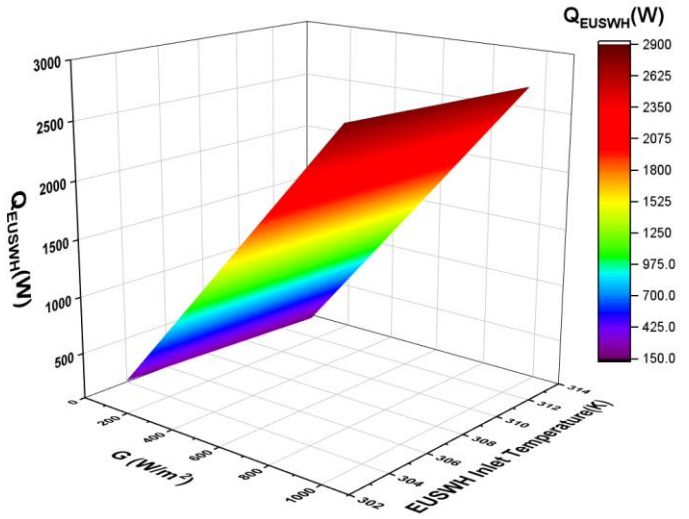

(b)

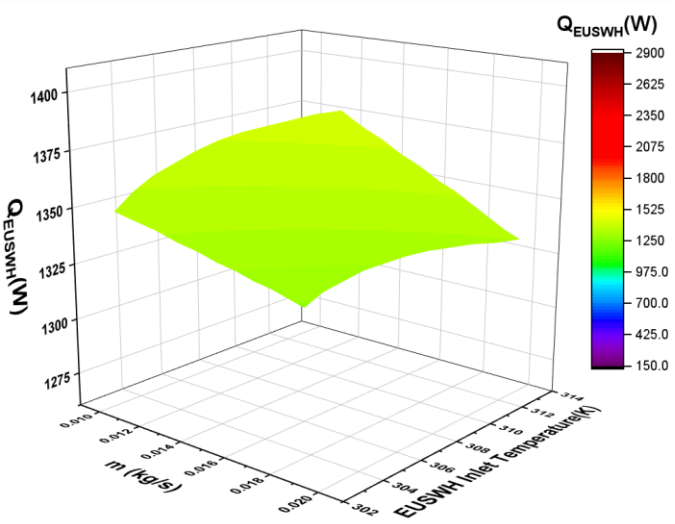

(c)

Fig. 7.10 (a-c) Effect of incident solar radiation, mass flow rate, and inlet EUSWH temperature on the useful solar energy

Fig. 7.11 (a-c) depicts the EUSWH efficiency variation with the incident solar radiation, water mass flow rate, and EUSWH inlet temperature. It can be easily observed that η_{EUSWH} increases with an increase in incident solar radiation, and mass flow rate, while it decreases with inlet EUSWH temperature. The solar radiation incident on the absorber tube directly supplies the energy for heating the water. When the incident solar radiation increases, the absorber tube absorbs more energy, leading to a higher temperature gradient between the tube and the water inside. This increases the rate of heat transfer to the water. Moreover, higher mass flow rates mean lower water outlet temperatures for a given incident energy, reducing thermal losses from the system to the surroundings. Hence the η_{EUSWH} increases with mass flow rate. When $T_{in,EUSWH}$ increases, the absorber loses more heat to the surroundings (thermal losses increase) because of the higher temperature difference between the absorber and the ambient air. The system's ability to extract energy from solar radiation diminishes, lowering its thermal efficiency. Another critical point to note here is that $T_{in,EUSWH}$ has a greater impact on η_{EUSWH} than the mass flow rate at a particular incident solar radiation. For instance, at G=1000W/m^2, η_{EUSWH} decreases by 5.55% and 4.92% at mass flow rates of 0.01 and 0.02kg/s,

respectively when the $T_{in,EUSWH}$ varies from 303-313K. However, it increases by 3.88% and 4.58% at $T_{in,EUSWH}$ of 303 and 313K, respectively when mass flow rates are varied from 0.01-0.02kg/s. Furthermore, the increment in η_{EUSWH} gradually decreases as G increases due to increased losses at higher solar radiation. Also, at low G, $T_{in,EUSWH}$ has a great influence on η_{EUSWH}.

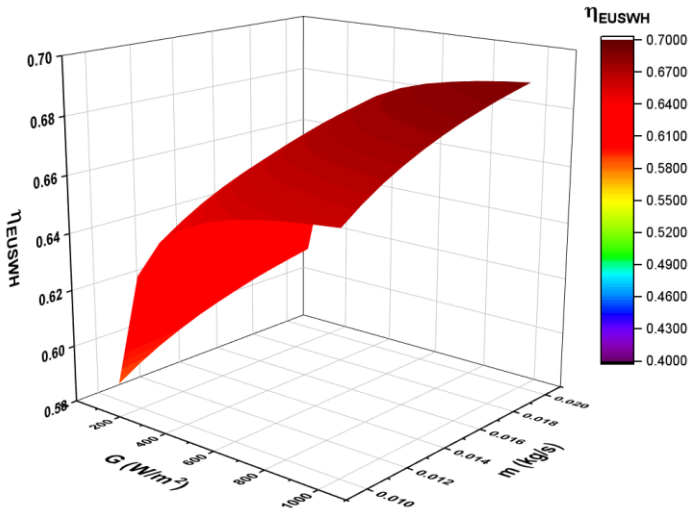

(a)

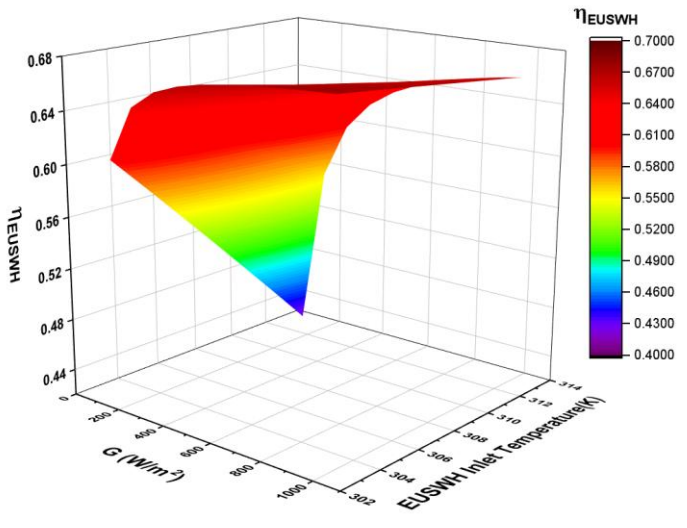

(b)

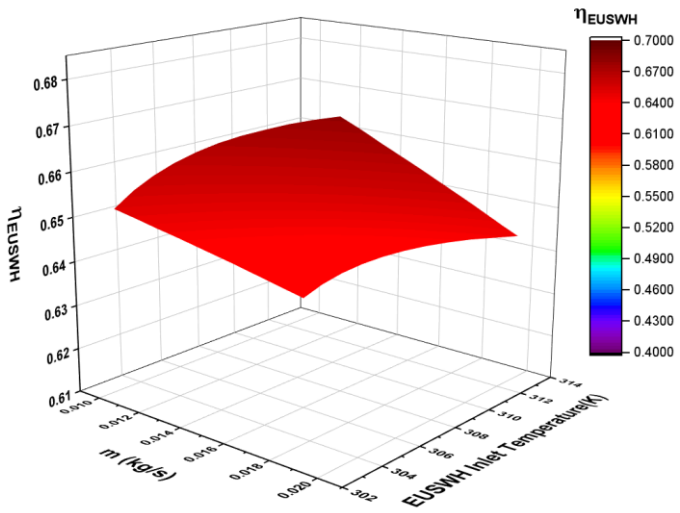

(c)

Fig. 7.11 (a-c) Effect of incident solar radiation, mass flow rate, and inlet EUSWH temperature on η_{EUSWH}

From the above analysis, it is observed that peak EUSWH performance is attained at the highest *G*. However, as the mass flow rate increases $T_{out,EUSWH}$ decreases while Q_{EUSWH} and η_{EUSWH} increase. The inlet EUSWH temperature shows the opposite trend and $T_{out,EUSWH}$ increases, Q_{EUSWH} and η_{EUSWH} decreases. So, it becomes important to study the further system at the minimum and maximum mass flow rates (0.01 and 0.02kg/s) and $T_{in,EUSWH}$ (303 and 313K) at the maximum incident solar radiation (1000W/m^2) to effectively investigate the TEG and hybrid system performance independently.

7.2.2 TEG performance

TEG performance parameters like voltage, current, power, and efficiency have been studied in this section inclusive of the fishtail vortex generator (FVG) impact on the TEG outputs. The performance of TEG for smooth and VG-employed channels for different mass flow rates at $T_{in,EUSWH}$ of 303K is shown in Fig. 7.12 (a-b). The application of VGs results in better TEG performance. The objective of employing VGs is achieved as they result in enhanced heat transfer and uniform temperature along the channel.

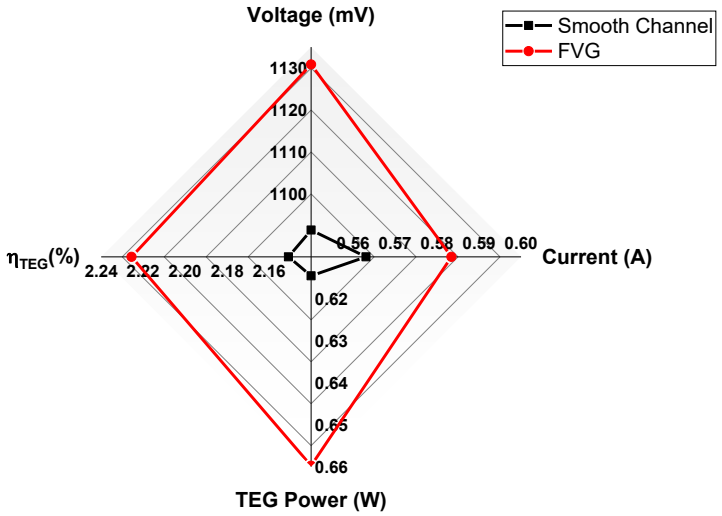

(a)

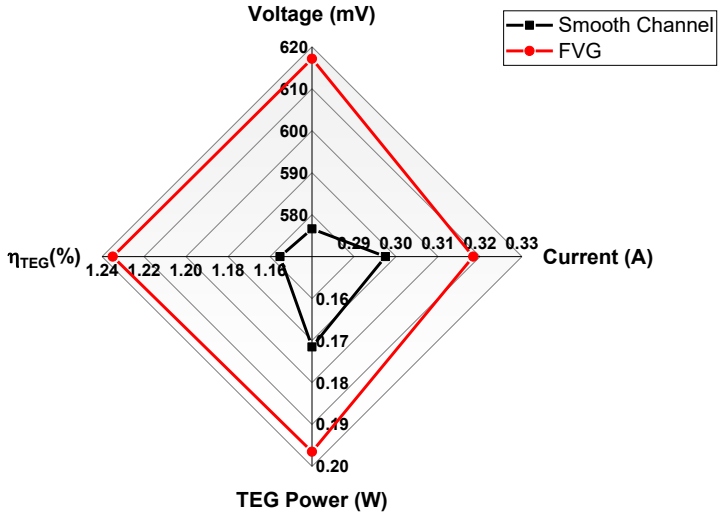

(b)

Fig. 7.12 TEG performance parameter at 303K, at (a) 0.01kg/s, and (b) 0.02kg/s

The mixing caused by vortices disrupts the laminar boundary layer and enhances convective heat transfer. This ensures that thermal energy is transported more efficiently from the working fluid to the channel walls and subsequently to the TEG modules. Furthermore, vortex generators disturb the thermal boundary layer, thinning it and making it more receptive to heat transfer. The continuous disruption ensures higher local heat transfer coefficients. Also, the generated vortices transition the flow towards turbulence or enhance the local turbulence intensity, which increases the convective heat transfer rate. For a mass flow rate of 0.01kg/s the voltage, current, power, and TEG efficiency

increase by 3.62%, 3.61%, 7.36%, and 3.47% respectively, when VGs are put to use. While at 0.02kg/s, the same parameters increased by 7.03%, 7.02%, 14.56%, and 5.13%. A similar trend can be seen in Fig. 7.13 (a-b). The vortex generator helps in achieving higher outputs. The vortex generators are simple structure and their presence negligibly increases the weight of the TEG module. FVGs introduce secondary flows in the form of streamwise and transverse vortices, which improve the mixing of hot and cold fluid layers. They minimize flow stagnation zones, where heat transfer would otherwise be less effective due to low fluid velocity. The improved heat transfer raises the temperature gradient across the TEG modules, directly increasing the output voltage and current. A higher thermal gradient translates into greater electrical power generation, enhancing the TEG's overall output. Efficient heat extraction and better utilization of thermal energy result in higher thermal-to-electric conversion efficiency. They provide additional benefits by reducing hot spots, and compact system design. The uniformity in heat transfer prevents localized overheating, improving the durability and performance consistency of the TEG. The higher heat transfer rates achieved with vortex generators allow for more compact system designs, reducing material costs and system weight. For a mass flow rate of 0.01kg/s and 313K; the voltage, current, power, and TEG efficiency increase by 3.73%, 3.72%, 7.61%, and 3.58% respectively, when VGs are used. While at 0.02kg/s, the same parameters increased by 7.26%, 7.16%, 15.04%, and 7.12%. Further analysis shows that the vortex generators are more efficient at lower $T_{in,EUSWH}$ in terms of the absolute values of the performance parameters. For instance, the TEG efficiency for channels with FVGs at 303 and 313K are 2.66% and 2.55% respectively. However, in terms of relative performance, higher sensitivity is observed in higher $T_{in,EUSWH}$. The result is consistent with Zhang et al. (2024), where at $T_{in,EUSWH}$ of 303 and 318K, η_{EUSWH} obtained are 1.94% and 2.77% respectively.

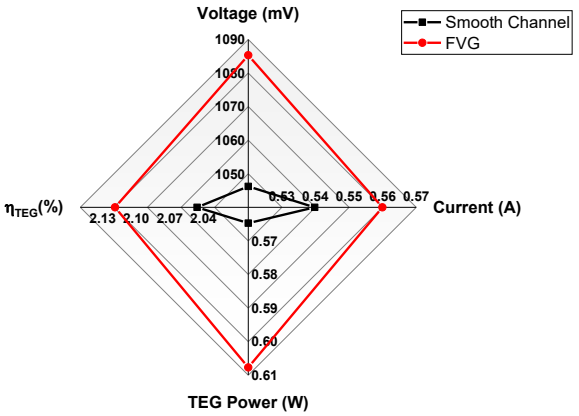

(a)

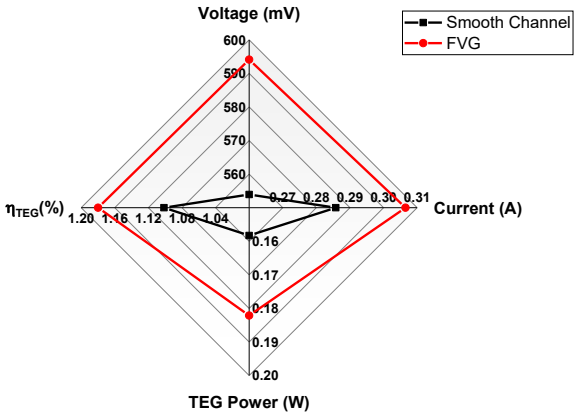

(b)

Fig. 7.13 TEG performance parameter at 313K, at (a) 0.01kg/s, and (b) 0.02kg/s

Table 7.3: Mass flow rate and inlet EUSWH temperature combination for Fig. 7.14

Channel configuration	Mass flow rate (kg/s)	$T_{in,EUSWH}$ (K)	Fig. caption
Smooth channel	0.2	313	Fig. 14 (a)
		303	Fig. 14 (b)
	0.1	313	Fig. 14 (c)
		303	Fig. 14 (d)
Channel with FVG	0.2	313	Fig. 14 (e)
		303	Fig. 14 (f)
	0.1	313	Fig. 14 (g)
		303	Fig. 14 (h)

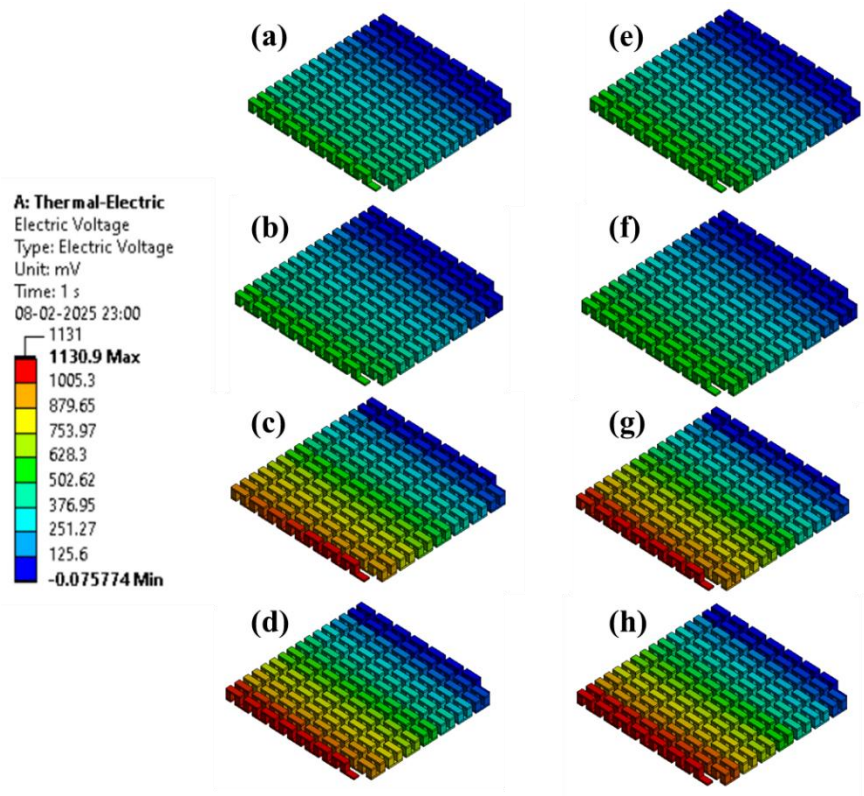

Fig. 7.14 Voltage nephograms of inner TEG for different inlet conditions as described in Table 7.3

Fig. 7.14 (a-h) shows the voltage contours of the inner TEG under different thermal and fluid flow inlet conditions. For the voltage analysis, one of the two terminals of the TEG is set as zero. This helps in the proper demonstration of the voltage distributions across the TEG. For the unambiguous Fig. notation of Fig. 7.14, the combination of inlet conditions of each contour has been described in Table 7.3. The output average voltage obtained for the smooth channel configuration (Fig. 7.14 (a-d)) with values of 553.92mV, 576.61mV, 1046.22mV, and 1091.39mV respectively. The output average voltages for channels equipped with FVGs (Fig. 7.14 (e-h)) are 594.12mV, 617.15mV, 1085.3mV, and 1130.85mV respectively.

7.2.3 Hybrid system performance

The cumulative effect of mass flow rates, $T_{in,EUSWH}$, and channel configuration on the hybrid system performance, i.e., hybrid system efficiency is shown in Fig. 7.15 (a-b). All these parameters govern the behavior of both EUSWH and TEG actions. The η_{HS} inculcates the combined efficacy of the EUSWH and TEG modules. It is defined as the ratio of TEG power output to the total incident solar radiation. Clearly, the η_{HS} is enhanced with the application of FVGs on the hot side of the TEG. The application of FVGs, results in more uniform temperature across the TEG's length. Due to vortex generators, the convective heat transfer coefficient increases, meaning heat is transferred away from the hot side more effectively. This leads to an increase in the hot side's effective temperature compared to its maximum potential, enhancing the thermoelectric efficiency. Also, at increased mass flow rates, the system may not allow sufficient time for the working fluid to heat up, lowering the temperature difference because TEGs operate optimally at a specific temperature difference. Increased flow rates also result in high heat dissipation to the surroundings. Hence the hybrid system efficiency deteriorates with increased mass flow rate. Furthermore, the temperature difference across the TEG is a critical parameter to the TEG output. As $T_{in,EUSWH}$ increases, $T_{out,EUSWH}$ also increases. But the increase in the latter is gradual and hence the TEG output decreases with increasing $T_{in,EUSWH}$. Fig. 7.15 (a) exhibits the η_{HS} at $T_{in,EUSWH}$=303K. The hybrid system efficiency increases by 7.39%, and 14.66% for 0.01 and 0.02kg/s mass flow rate, respectively, due to FVGs application. At $T_{in,EUSWH}$=313K (Fig. 7.15 (b)), η_{HS} increases by 7.62% and 15% for 0.01 and 0.02kg/s. Also, the highest and the lowest η_{HS} obtained are 0.0192% (at G=1000W/m^2, mass flow rate=0.01kg/s, and $T_{in,EUSWH}$=303K, FVG incorporated channel), and 0.0046% (at G=1000W/m^2, mass flow rate=0.02kg/s, and $T_{in,\ EUSWH}$=313K, smooth channel) respectively.

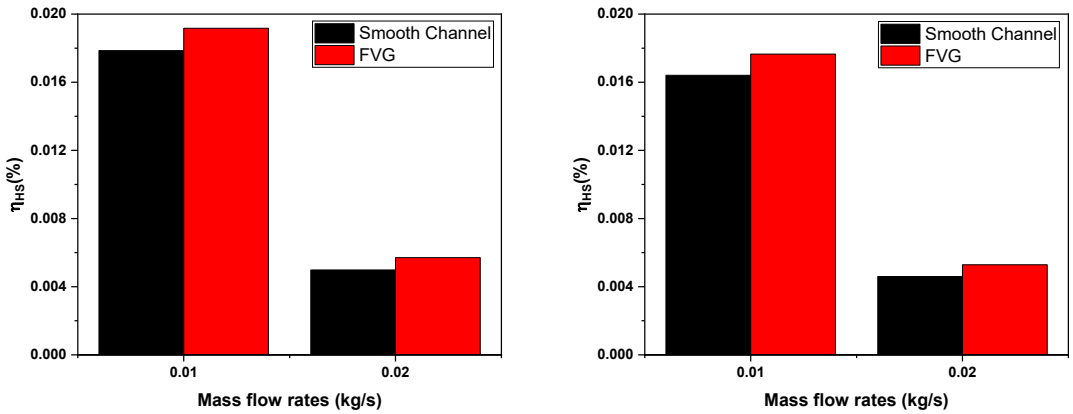

Fig. 7.15 Hybrid system efficiency of different channel configurations at (a) 303K, and (b) 313K of $T_{in,EUSWH}$

7.3 Highlights

- It is observed that η_{EUSWH} increases with an increase in incident solar radiation, and mass flow rate, while it decreases with inlet EUSWH temperature.
- At G=1000W/m^2, η_{EUSWH} decreases by 5.55% and 4.92% at mass flow rates of 0.01 and 0.02kg/s, respectively when the $T_{in,EUSWH}$ varies from 303-313K. However, it increases by 3.88% and 4.58% at $T_{in,EUSWH}$ of 303 and 313K, respectively when mass flow rates are varied from 0.01-0.02kg/s.
- The analysis shows that the vortex generators are more efficient at lower $T_{in,EUSWH}$ and low mass flow rates.
- The application of VGs results in better TEG performance. The objective of employing VGs is clearly achieved as they result in enhanced heat transfer and uniform temperature along the channel.
- The η_{HS} is enhanced with the application of FVGs on the hot side of the TEG. The hybrid system efficiency increases by 7.39 %, and 14.66% for 0.01 and 0.02kg/s

mass flow rate, respectively, due to FVGs application at 303K. At $T_{in,EUSWH}$ =313K, η_{HS} increases by 7.62% and 15% for 0.01 and 0.02kg/s.

Chapter 8

Concluding Remarks and Future Scope

8.1 Concluding remarks

The research focuses on enhancing waste heat recovery through thermoelectric generators (TEGs) by systematically investigating all three critical components: the hot side, the TEG module, and the cold side. The study further optimized the heat transfer enhancement technique on the hot side to identify the most efficient configuration. Finally, a solar-TEG hybrid system was developed, integrating the optimized vortex generator configuration, to comprehensively evaluate its performance. At each stage of the study, the main inferences can be summarized as follows:

- The maximum heat transfer coefficient improvements on the hot side for envelope, delta, and fishtail VGs were observed to be 45.16%, 51.85%, and 56.18% respectively, over the smooth channel. The maximum pressure drop increases by 1.3, 1.47, and 1.17 times for envelope, delta, and fishtail VGs respectively over the smooth channel.
- The value of TEF for all the VG configurations remains above 1, which showcases the thermohydraulic effectiveness of the VGs. The highest value of 1.32 is exhibited by FVG at D/H=4 and θ=30°. The power output of the TEG increases with the installment of VGs. The highest power output obtained is 1.62W at D/H=2, θ=60° for the fishtail vortex generator.
- The distance-to-height ratio and angle of inclination angle of the VGs for obtaining the highest thermohydraulic performance of the hot side of the TEG were D/H=2 and θ=60° for fishtail VG.

- Vortex generators (VGs) enhance heat transfer by creating longitudinal vortices that disrupt the thermal boundary layer and improve fluid mixing. This mechanism brings higher-temperature fluid into direct contact with heat exchange surfaces, leading to a more uniform temperature distribution. Consequently, VGs significantly improve the hot-side performance of a TEG, which can increase power output and enable the design of more compact waste heat recovery systems.
- Multistaging, novel materials, and variable cross-section give an improved performance with MVS-TEG-2 as the best-performing TEG. It produces the highest voltage (165.1V), power (31.1W), and conversion efficiency (18.75%).
- The highest second law efficiency is exhibited by MVS TEG-3 with a value of 24.49%. MVS TEG-2 exhibits the best-normalized performance when row numbers are considered, while MVS TEG-3 exhibits the best-normalized performance when exhaust inlet temperature and coolant flow rate are considered.
- The novel multi-variable strategy (MVS) TEG design demonstrated superior conversion efficiency. This performance enhancement is a direct result of implementing key modifications: multi-stage architecture, tapered leg geometry, and the use of dissimilar materials with advanced thermoelectric properties, which collectively optimize thermal impedance matching and energy conversion.
- Among the different coolants studied, the best thermal performance is exhibited by the cylindrical-brick (MWCNT-Fe_3O_4) blend, and the best exergetic performance by the blade-cylindrical (Al_2O_3-MWCNT) blend.
- The cylindrical-brick (MWCNT-Fe_3O_4) blend improves the heat transfer coefficient by 79.27% and the blade-cylindrical (Al_2O_3-MWCNT) blend exhibits the highest FOM value of 0.9841 at φ=0.001 and flow rate =7 x$10^{-6}$$m^3$/s.

- The highest TEG power and conversion efficiency is exhibited when a cylindrical-brick (MWCNT-Fe_3O_4) blend is used. The highest values obtained are 6.085W and 5.47% respectively.
- Hybrid nanofluids serve as advanced coolants with the potential to significantly improve heat extraction on the TEG's cold side due to their superior thermal properties. For practical implementation, future work must address inherent challenges such as increased pumping power demands, nanoparticle precipitation, and long-term stability to ensure viability.
- The highest values of heat transfer coefficient, pressure drop, and TEF obtained are 554.17W/m^2K at ambient h=5W/m^2K for FVG, 12.93Pa for DVG, and 2.258 for FVG at h=25W/m^2K.
- With 20 neurons in the hidden layer and 1 in the output layer, predicting fit quality (R^2) of 1, 0.99994, 0.99962, and 0.99991.
- Analyzing heat transfer performance under a wide range of ambient and operating conditions is critical for assessing real-world applicability. Furthermore, employing optimization algorithms and artificial neural networks is recommended to efficiently determine the statistically optimal configuration for a vortex generator-enhanced TEG system, moving beyond a parametric study to a definitive design solution.
- The TEG power is improved with the installment of the fishtail VGs in the EUSWH-TEG hybrid system. The maximum voltage, current, power, and conversion efficiency increase by 3.57%, 3.62%, 7.49%, and 3.25% respectively for channels equipped with fishtail VGs, at mass flow rate=0.01kg/s and inlet temperature=303K.

- The maximum improvement hybrid system efficiency obtained is 7.39% at mass flow rate=0.01kg/s and inlet temperature=303K with fishtail VG.
- The integration of a TEG with a solar water heater presents a viable co-generation system for the simultaneous production of electricity and domestic hot water. The overall efficiency of this hybrid system can be substantially increased by incorporating performance-enhancing structures like vortex generators on the thermal side, maximizing the utilization of captured solar energy.

Based on the studies conducted in this thesis, the overall performance of a thermoelectric generator (TEG)-based waste heat recovery system can be significantly enhanced. This improvement is not attributable to a single factor, but rather to the synergistic optimization of all major aspects associated with a TEG module. These include maximizing the temperature difference across the hot and cold sides, as well as optimizing TEG device specifications such as staging, leg geometry, and material properties. Furthermore, the findings indicate substantial potential for refining these TEG enhancements and integrating them with other energy systems to develop efficient co-generation applications.

This study provides insights into TEG system enhancement, but its findings should be considered in light of the following limitations:

- Modeling Assumptions and Simplifications: The use of a steady-state model does not capture real-world transient operations, such as varying exhaust flow. The assumption of constant thermophysical properties for all materials ignores their temperature-dependent nature, likely leading to conservative performance estimates.

- Scope of Design Parameters: The study was limited to a predefined set of vortex generator shapes and nanofluid combinations. Performance may be further improved by exploring geometries or materials beyond the selected scope.
- Economic and Practical Viability: The analysis focuses solely on technical performance, omitting economic considerations such as manufacturing costs, nanofluid premium pricing, and cost-per-watt analysis. This limits assessment of real-world feasibility.
- System-Level Integration Challenges: The hybrid system analysis remains theoretical. Practical integration challenges, including control complexity, maintenance, and performance under real weather conditions, were not explored.

8.2 Future scope

The conclusions of this thesis provide a clear foundation for several targeted research directions. Based on the limitations and opportunities identified in this work, the following future studies are recommended to build upon these findings and facilitate practical application:

- Optimization of Novel Vortex Generator Configurations: While this study demonstrated the superior performance of the fishtail vortex generator, future work should focus on its geometric optimization. Drawing from the conclusion that distance-to-height ratio (d/H) is a critical parameter, a multi-objective optimization study should be conducted to determine the ideal d/H, pitch, and angling for fishtail generators specifically, to maximize the trade-off between heat transfer enhancement and pressure drop. This would provide industry with a ready-to-implement optimal design.

- Development of Application-Specific TEG Modules: The models developed here assumed constant material properties. To directly leverage the finding that temperature gradient is the primary driver of power output, future research should involve prototyping and experimentally validating a staged TEG system. This system would use different materials (e.g., Skutterudites on the hot side, Bi_2Te_3 on the cold side) optimized for the specific temperature ranges encountered in automotive exhaust or solar thermal systems, moving from theoretical modeling to practical, high-efficiency module design.
- System-Level Integration and Hybrid Nanofluid Validation: Building on the promising thermohydraulic performance predicted for hybrid nanofluids, a critical next step is to address practical application barriers. Future work must experimentally investigate the long-term stability, dispersion homogeneity, and corrosion impact of these nanofluids on a TEG's cold-side heat exchanger. This is essential for industry adoption, as it assesses durability and real-world maintenance costs alongside performance gains.
- Transient and Real-World Condition Analysis: This study was conducted under steady-state assumptions. To apply this work to real industrial environments like automotive exhaust cycles, future research must develop a transient model. This model would simulate the system's performance under dynamic conditions—such as varying exhaust gas temperature, mass flow rates, and coolant flow—to predict actual energy recovery over a standard driving cycle and validate the system's robustness.

The findings of this thesis provide a foundation for both academic advancement and practical engineering application. The following recommendations are offered to improve upon the present work and to guide its potential implementation.

8.2.1 Recommendations for improving the present work

To enhance the accuracy and robustness of the current models, the following steps are recommended:

- Incorporate Temperature-Dependent Properties: The assumption of constant thermophysical and thermoelectric properties, while simplifying the model, is a source of error. It is recommended to refine the computational model by implementing temperature-dependent properties for exhaust gases, nanofluids, and TEG materials. This will provide a more accurate, quantitative prediction of absolute system performance, especially under high-temperature gradients.
- Develop and Validate a Transient Model: The steady-state assumption limits the model's applicability to real-world scenarios like automotive drive cycles. The immediate next step should be the development of a dynamic, transient model that can simulate performance under varying exhaust and coolant conditions. This model must be validated against experimental data from a laboratory-scale prototype to confirm its predictive reliability.
- Experimental Validation of Key Findings: The superior performance of the fishtail vortex generator and the specific hybrid nanofluids should be confirmed through rigorous experimentation. Building a prototype heat exchanger and TEG setup for bench testing is crucial to move these findings from theoretical promise to proven concept, thereby quantifying any discrepancies between simulation and reality.

8.2.2 Recommendations for application and implementation

The present work offers valuable insights for industry and system designers in the field of waste heat recovery:

- For Automotive Exhaust System Designers: The fishtail vortex generator, particularly at its optimal distance-to-height ratio (d/H) identified in this study, is recommended for integration into the design of new exhaust heat recovery systems. Its design offers a favorable balance between heat transfer enhancement and pressure drop, which is critical for minimizing engine backpressure.
- For TEG Module Manufacturers: This research demonstrates that significant gains can be achieved through system-level design rather than just material science. Manufacturers are recommended to explore the development of application-specific, staged TEG modules tailored to the temperature profiles of different heat sources (e.g., automotive exhaust vs. solar thermal systems), as the analysis shows temperature gradient is the primary driver of power output.
- For Thermal System Engineers: For applications requiring high heat flux dissipation on the cold side of a TEG, the use of the specific hybrid nanofluid combinations analyzed in this work is recommended. However, a parallel focus on solving practical challenges of nanofluid stability, corrosion prevention, and economic viability is essential for successful long-term deployment.
- For Hybrid System Integrators: The successful integration of TEG technology with an Evacuated U-tube Solar Water Heater presents a viable blueprint for developing co-generation systems. It is recommended that this concept be piloted in residential or commercial settings to provide both hot water and auxiliary electricity, thereby improving overall energy sustainability.

By following these recommendations, researchers can build upon the limitations of this work, and industry practitioners can leverage its key findings for practical, efficient energy harvesting systems.

REFERENCES

Ahmadi Atouei, S., Ranjbar, A. A., & Rezania, A. (2017). Experimental investigation of two-stage thermoelectric generator system integrated with phase change materials. *Applied Energy*, *208*, 332–343. https://doi.org/https://doi.org/10.1016/j.apenergy.2017.10.032

Ahmed, H. E., Yusoff, M. Z., Hawlader, M. N. A., Ahmed, M. I., Salman, B. H., & Kerbeet, A. Sh. (2017). Turbulent heat transfer and nanofluid flow in a triangular duct with vortex generators. *International Journal of Heat and Mass Transfer*, *105*, 495–504. https://doi.org/https://doi.org/10.1016/j.ijheatmasstransfer.2016.10.009

Aljaghtham, M. (2024). A comparative performance analysis of thermoelectric generators with a novel leg geometries. *Energy Reports*, *11*, 859–876. https://doi.org/https://doi.org/10.1016/j.egyr.2023.12.041

Alobaid, M., Maduabuchi, C., Albaker, A., Almalaq, A., Alanazi, M., & Alsuwian, T. (2023). Machine learning and numerical simulations for electrical, thermodynamic, and mechanical assessment of modified solar thermoelectric generators. *Applied Thermal Engineering*, *220*, 119706. https://doi.org/https://doi.org/10.1016/j.applthermaleng.2022.119706

Armstead, J. R., & Miers, S. A. (2013). Review of waste heat recovery mechanisms for internal combustion engines. *Journal of Thermal Science and Engineering Applications*, *6*(1). https://doi.org/10.1115/1.4024882

Arora, R., Kaushik, S. C., & Arora, R. (2015). Multi-objective and multi-parameter optimization of two-stage thermoelectric generator in electrically series and parallel configurations through NSGA-II. *Energy*, *91*, 242–254. https://doi.org/https://doi.org/10.1016/j.energy.2015.08.044

Arora, R., Kaushik, S. C., & Arora, R. (2016). Thermodynamic modeling and multi-objective optimization of two stage thermoelectric generator in electrically series and parallel configuration. *Applied Thermal Engineering*, *103*, 1312–1323. https://doi.org/https://doi.org/10.1016/j.applthermaleng.2016.05.009

Ataei, M., Sadegh Moghanlou, F., Noorzadeh, S., Vajdi, M., & Shahedi Asl, M. (2020). Heat transfer and flow characteristics of hybrid Al2O3/TiO2–water nanofluid in a minichannel heat sink. *Heat and Mass Transfer*, *56*(9), 2757–2767. https://doi.org/10.1007/s00231-020-02896-9

Bahiraei, M., Jamshidmofid, M., & Goodarzi, M. (2019). Efficacy of a hybrid nanofluid in a new microchannel heat sink equipped with both secondary channels and ribs. *Journal of Molecular Liquids*, *273*, 88–98. https://doi.org/10.1016/j.molliq.2018.10.003

Bejan, A. (1996). *Convection Heat Transfer*.

Bejan, A., Lorente, S., & Kang, D. H. (2014). Constructal design of thermoelectric power packages. *International Journal of Heat and Mass Transfer*, *79*, 291–299. https://doi.org/10.1016/j.ijheatmasstransfer.2014.08.008

Benkhedda, M., Boufendi, T., Tayebi, T., & Chamkha, A. J. (2020). Convective heat transfer performance of hybrid nanofluid in a horizontal pipe considering nanoparticles shapes effect. *Journal of Thermal Analysis and Calorimetry*, *140*(1), 411–425. https://doi.org/10.1007/s10973-019-08836-y

Bergman, T. L., Lavine, A. S., Incropera, F. P., & DeWitt, D. P. (2011). *Introduction to heat transfer* (6th ed.). John Wiley & Sons.

Caliskan, S. (2014). Experimental investigation of heat transfer in a channel with new winglet-type vortex generators. *International Journal of Heat and Mass Transfer*, *78*, 604–614. https://doi.org/https://doi.org/10.1016/j.ijheatmasstransfer.2014.07.043

Carpio, J., & Valencia, A. (2021). Heat transfer enhancement through longitudinal vortex generators in compact heat exchangers with flat tubes. *International Communications in Heat and Mass Transfer*, *120*, 105035. https://doi.org/https://doi.org/10.1016/j.icheatmasstransfer.2020.105035

Chen, J., Yuan, H., Zhu, Y. K., Zheng, K., Ge, Z. H., Tang, J., Zhou, D., Yang, L., & Chen, Z. G. (2021). Ternary Ag2Se1- xTex: A Near-Room-Temperature Thermoelectric Material with a Potentially High Figure of Merit. *Inorganic Chemistry*, *60*(18), 14165–14173. https://doi.org/10.1021/acs.inorgchem.1c01563

Chen, W.-H., & Chiou, Y.-B. (2020). Geometry design for maximizing output power of segmented skutterudite thermoelectric generator by evolutionary computation. *Applied Energy*, *274*, 115296. https://doi.org/https://doi.org/10.1016/j.apenergy.2020.115296

Chen, Y., He, M., Liu, B., Bazan, G. C., Zhou, J., & Liang, Z. (2017). Bendable n-Type Metallic Nanocomposites with Large Thermoelectric Power Factor. *Advanced Materials*, *29*(4). https://doi.org/10.1002/adma.201604752

Cheng, K., Qin, J., Jiang, Y., Zhang, S., & Bao, W. (2018). Performance comparison of single- and multi-stage onboard thermoelectric generators and stage number optimization at a large temperature difference. *Applied Thermal Engineering*, *141*, 456–466. https://doi.org/https://doi.org/10.1016/j.applthermaleng.2018.05.127

Chu, Y., Bashir, S., Ramzan, M., & Malik, M. Y. (2023). Model-based comparative study of magnetohydrodynamics unsteady hybrid nanofluid flow between two infinite parallel plates with particle shape effects. *Mathematical Methods in the Applied Sciences*, *46*(10), 11568–11582. https://doi.org/10.1002/mma.8234

Das, A. K., & Hiremath, S. S. (2023). Multi-objective optimization of a novel butterfly-wing vortex generator fabricated in a rectangular microchannel based on CFD and NSGA-II genetic algorithm. *Applied Thermal Engineering*, *234*, 121187. https://doi.org/https://doi.org/10.1016/j.applthermaleng.2023.121187

Degousée, T., Untilova, V., Vijayakumar, V., Xu, X., Sun, Y., Palma, M., Brinkmann, M., Biniek, L., & Fenwick, O. (2021). High thermal conductivity states and enhanced figure of merit in aligned polymer thermoelectric materials. *Journal of Materials Chemistry A*, *9*(29), 16065–16075. https://doi.org/10.1039/d1ta03377h

Demirag, H. Z., Dogan, M., & Igci, A. A. (2022). The numerical analysis of novel type conic vortex generator and comparison with known VGs for heat transfer enhancement. *Heat and Mass Transfer*, *58*(5), 735–762. https://doi.org/10.1007/s00231-021-03117-7

Deshmukh, P. W., Prabhu, S. V., & Vedula, R. P. (2016). Heat transfer enhancement for laminar flow in tubes using curved delta wing vortex generator inserts. *Applied Thermal Engineering*, *106*, 1415–1426. https://doi.org/10.1016/j.applthermaleng.2016.06.120

Ebrahimi, A., Rikhtegar, F., Sabaghan, A., & Roohi, E. (2016). Heat transfer and entropy generation in a microchannel with longitudinal vortex generators using nanofluids. *Energy*, *101*, 190–201. https://doi.org/https://doi.org/10.1016/j.energy.2016.01.102

Ebrahimi, A., Roohi, E., & Kheradmand, S. (2015). Numerical study of liquid flow and heat transfer in rectangular microchannel with longitudinal vortex generators. *Applied Thermal Engineering*, *78*, 576–583. https://doi.org/https://doi.org/10.1016/j.applthermaleng.2014.12.006

Elias, M. M., Shahrul, I. M., Mahbubul, I. M., Saidur, R., & Rahim, N. A. (2014). Effect of different nanoparticle shapes on shell and tube heat exchanger using different baffle angles and operated with nanofluid. *International Journal of Heat and Mass Transfer*, *70*, 289–297. https://doi.org/https://doi.org/10.1016/j.ijheatmasstransfer.2013.11.018

Ellahi, R., Hassan, M., & Zeeshan, A. (2015). Shape effects of nanosize particles in Cu–H2O nanofluid on entropy generation. *International Journal of Heat and Mass Transfer*, *81*, 449–456. https://doi.org/https://doi.org/10.1016/j.ijheatmasstransfer.2014.10.041

Erturun, U., Erermis, K., & Mossi, K. (2015). Influence of leg sizing and spacing on power generation and thermal stresses of thermoelectric devices. *Applied Energy*, *159*, 19–27. https://doi.org/https://doi.org/10.1016/j.apenergy.2015.08.112

Feng, Y., Xu, R., Cao, Y., Wu, X., Liang, C., & Zhang, L. (2023). Optimization of H-type finned tube heat exchangers with combinations of longitudinal vortex generator, dimples/protrusions and grooves by Taguchi method. *International Communications in Heat and Mass Transfer*, *143*, 106709. https://doi.org/https://doi.org/10.1016/j.icheatmasstransfer.2023.106709

Garud, K. S., Hwang, S.-G., Han, J.-W., & Lee, M.-Y. (2021). Review on Performance Enhancement of Photovoltaic/Thermal–Thermoelectric Generator Systems with Nanofluid Cooling. *Symmetry*, *14*(1), 36. https://doi.org/10.3390/sym14010036

Ge, Y., He, K., Xiao, L., Yuan, W., & Huang, S.-M. (2022). Geometric optimization for the thermoelectric generator with variable cross-section legs by coupling finite

element method and optimization algorithm. *Renewable Energy*, *183*, 294–303. https://doi.org/https://doi.org/10.1016/j.renene.2021.11.016

Gharzi, M., Kermani, A. M., & Tash Shamsabadi, H. (2023). Experimental investigation of a parabolic trough collector-thermoelectric generator (PTC-TEG) hybrid solar system with a pressurized heat transfer fluid. *Renewable Energy*, *202*, 270–279. https://doi.org/https://doi.org/10.1016/j.renene.2022.11.110

Harman, T. C., Taylor, P. J., Walsh, M. P., & LaForge, B. E. (2002). Quantum Dot Superlattice Thermoelectric Materials and Devices. *Science*, *297*(5590), 2229–2232. https://doi.org/10.1126/science.1072886

He, W., Su, Y., Wang, Y. Q., Riffat, S. B., & Ji, J. (2012). A study on incorporation of thermoelectric modules with evacuated-tube heat-pipe solar collectors. *Renewable Energy*, *37*(1), 142–149. https://doi.org/https://doi.org/10.1016/j.renene.2011.06.002

He, W., Wang, S., Zhang, X., Li, Y., & Lu, C. (2015). Optimization design method of thermoelectric generator based on exhaust gas parameters for recovery of engine waste heat. *Energy*, *91*, 1–9. https://doi.org/10.1016/j.energy.2015.08.022

Jaafreh, R., Yoo Seong, K., Kim, J. G., & Hamad, K. (2022). A deep learning perspective into the figure-of-merit of thermoelectric materials. *Materials Letters*, *319*. https://doi.org/10.1016/j.matlet.2022.132299

Jiang, K., Hong, S. H., Tung, S. H., & Liu, C. L. (2022). Effects of cation size on thermoelectricity of PEDOT:PSS/ionic liquid hybrid films for wearable thermoelectric generator application. *Journal of Materials Chemistry A*, *10*(36), 18792–18802. https://doi.org/10.1039/d2ta05134f

Jiansheng, W., Yu, J., & Xueling, L. (2019). Heat transfer and flow characteristics in a rectangular channel with small scale vortex generators. *International Journal of Heat and Mass Transfer*, *138*, 208–225. https://doi.org/https://doi.org/10.1016/j.ijheatmasstransfer.2019.03.138

Johnson, I., Choate, W. T., & Davidson, A. (2008). *Waste Heat Recovery: Technology and Opportunities in U.S. Industry*.

Karana, D. R., & Sahoo, R. R. (2018). Effect on TEG performance for waste heat recovery of automobiles using MgO and ZnO nanofluid coolants. *Case Studies in Thermal Engineering*, *12*, 358–364. https://doi.org/10.1016/j.csite.2018.05.006

Karana, D. R., & Sahoo, R. R. (2019a). Influence of geometric parameter on the performance of a new asymmetrical and segmented thermoelectric generator. *Energy*, *179*, 90–99. https://doi.org/10.1016/j.energy.2019.04.199

Karana, D. R., & Sahoo, R. R. (2019b). Performance effect on the TEG system for waste heat recovery in automobiles using ZnO and SiO2 nanofluid coolants. *Heat Transfer - Asian Research*, *48*(1), 216–232. https://doi.org/10.1002/htj.21379

Karana, D. R., & Sahoo, R. R. (2021). Heat Transfer and Pressure Drop Investigations of the Compact Exhaust Heat Exchanger With Twisted Tape Inserts for Automotive

Waste Heat Utilization. *Journal of Thermal Science and Engineering Applications*, *13*(4). https://doi.org/10.1115/1.4048672

Khalil, A., Elhassnaoui, A., Yadir, S., Abdellatif, O., Errami, Y., & Sahnoun, S. (2023). Study of Diverse Leg Geometry Effect on the Performance of Segmented Thermoelectric Generator with the Same Leg Volume. *Trends in Sciences*, *20*(10), 6099. https://doi.org/10.48048/tis.2023.6099

Khalil, H., & Hassan, H. (2020). Enhancement of waste heat recovery from vertical chimney via thermoelectric generators by heat spreader. *Process Safety and Environmental Protection*, *140*, 314–329. https://doi.org/https://doi.org/10.1016/j.psep.2020.05.023

Khan, U., Adnan, Ahmed, N., & Mohyud-Din, S. T. (2017). Influence of the shape factor on the flow and heat transfer of a water-based nanofluid in a rotating system. *The European Physical Journal Plus*, *132*(4), 166. https://doi.org/10.1140/epjp/i2017-11410-4

Khatirzad, H., & Sheikholeslami, M. (2025). Numerical investigation of hybrid nanofluid flow in a finned heat sink integrated with a concentrated solar system and thermoelectric generator. *Renewable Energy*, *245*, 122783. https://doi.org/10.1016/j.renene.2025.122783

Kim, G.-H., Shao, L., Zhang, K., & Pipe, K. P. (2013). Engineered doping of organic semiconductors for enhanced thermoelectric efficiency. *Nature Materials*, *12*(8), 719–723. https://doi.org/10.1038/nmat3635

Krishna Kumar, T. S., Anil Kumar, S., Kodanda Ram, K., Raj Goli, K., & Siva Prasad, V. (2021). Analysis of thermo electric generators in automobile applications. *Materials Today: Proceedings*, *45*, 5835–5839. https://doi.org/10.1016/j.matpr.2020.08.081

Kumar, A., Said, Z., & Bellos, E. (2021). An up-to-date review on evacuated tube solar collectors. *Journal of Thermal Analysis and Calorimetry*, *145*(6), 2873–2889. https://doi.org/10.1007/s10973-020-09953-9

Kumar, V., & Sahoo, R. R. (2019). Viscosity and thermal conductivity comparative study for hybrid nanofluid in binary base fluids. *Heat Transfer - Asian Research*, *48*(7), 3144–3161. https://doi.org/10.1002/htj.21535

Kumar, V., & Sahoo, R. R. (2021). Exergy and energy performance for wavy fin radiator with a new coolant of various shape nanoparticle-based hybrid nanofluids. *Journal of Thermal Analysis and Calorimetry*, *143*(6), 3911–3922. https://doi.org/10.1007/s10973-020-09361-z

Kumar, V., & Sarkar, J. (2019). Numerical and experimental investigations on heat transfer and pressure drop characteristics of Al 2 O 3 -TiO 2 hybrid nanofluid in minichannel heat sink with different mixture ratio. *Powder Technology*, *345*, 717–727. https://doi.org/10.1016/j.powtec.2019.01.061

Kumar, V., & Sarkar, J. (2020a). Experimental hydrothermal behavior of hybrid nanofluid for various particle ratios and comparison with other fluids in minichannel heat sink.

International Communications in Heat and Mass Transfer, *110*. https://doi.org/10.1016/j.icheatmasstransfer.2019.104397

Kumar, V., & Sarkar, J. (2020b). Experimental hydrothermal characteristics of minichannel heat sink using various types of hybrid nanofluids. *Advanced Powder Technology*, *31*(2), 621–631. https://doi.org/10.1016/j.apt.2019.11.017

Lamba, R., & Kaushik, S. C. (2017). Thermodynamic analysis of thermoelectric generator including influence of Thomson effect and leg geometry configuration. *Energy Conversion and Management*, *144*, 388–398. https://doi.org/https://doi.org/10.1016/j.enconman.2017.04.069

Lavine, A. S., Incropera, F. P., Dewitt, D. P., & Bergman, T. L. (2013). *Principle of Heat and Mass Transfer*.

Lee, M.-Y., Seo, J.-H., Lee, H.-S., & Garud, K. S. (2020). Power Generation, Efficiency and Thermal Stress of Thermoelectric Module with Leg Geometry, Material, Segmentation and Two-Stage Arrangement. *Symmetry*, *12*(5), 786. https://doi.org/10.3390/sym12050786

Li, Z., Feng, Z., Zhang, Q., Zhou, J., Zhang, J., & Guo, F. (2023). Thermal-hydraulic performance and multi-objective optimization using ANN and GA in microchannels with double delta-winglet vortex generators. *International Journal of Thermal Sciences*, *193*, 108489. https://doi.org/10.1016/j.ijthermalsci.2023.108489

Liang, X., Kumar, N. B., Mansir, I. B., Kumar Singh, P., Abed, A. M., Dahari, M., Nasr, S., Albalawi, H., Cherif, A., & Wae-hayee, M. (2023). Management of heat transfer and hydraulic characteristics of a micro-channel heat sink with various arrangements of rectangular vortex generators utilizing artificial neural network and response surface methodology. *Case Studies in Thermal Engineering*, *44*, 102850. https://doi.org/10.1016/j.csite.2023.102850

Liu, F., Cai, Y., Wang, L., & Zhao, J. (2018). Effects of nanoparticle shapes on laminar forced convective heat transfer in curved ducts using two-phase model. *International Journal of Heat and Mass Transfer*, *116*, 292–305. https://doi.org/https://doi.org/10.1016/j.ijheatmasstransfer.2017.08.097

Liu, L., Sun, Y., Li, W., Zhang, J., Huang, X., Chen, Z., Sun, Y., Di, C., Xu, W., & Zhu, D. (2017). Flexible unipolar thermoelectric devices based on patterned poly[K_x (Ni-ethylenetetrathiolate)] thin films. *Materials Chemistry Frontiers*, *1*(10), 2111–2116. https://doi.org/10.1039/C7QM00223H

Liu, X., Shi, X.-L., Zhang, L., Liu, W.-D., Yang, Y., & Chen, Z.-G. (2023). One-step post-treatment boosts thermoelectric properties of PEDOT:PSS flexible thin films. *Journal of Materials Science & Technology*, *132*, 81–89. https://doi.org/https://doi.org/10.1016/j.jmst.2022.05.047

Liu, X., Toghraie, D., Hekmatifar, M., Akbari, O. A., Karimipour, A., & Afrand, M. (2020). Numerical investigation of nanofluid laminar forced convection heat transfer between two horizontal concentric cylinders in the presence of porous medium.

Journal of Thermal Analysis and Calorimetry, *141*(5), 2095–2108. https://doi.org/10.1007/s10973-020-09406-3

Ma, T., Lu, X., Pandit, J., Ekkad, S. V, Huxtable, S. T., Deshpande, S., & Wang, Q. (2017). Numerical study on thermoelectric–hydraulic performance of a thermoelectric power generator with a plate-fin heat exchanger with longitudinal vortex generators. *Applied Energy*, *185*, 1343–1354. https://doi.org/https://doi.org/10.1016/j.apenergy.2016.01.078

Ma, T., Pandit, J., Ekkad, S. V, Huxtable, S. T., & Wang, Q. (2015). Simulation of thermoelectric-hydraulic performance of a thermoelectric power generator with longitudinal vortex generators. *Energy*, *84*, 695–703. https://doi.org/https://doi.org/10.1016/j.energy.2015.03.033

Maduabuchi, C., & Alobaid, M. (2022). Geometry and stage number optimization of a concentrating solar multistage segmented thermoelectric generator by exploiting different optimization schemes. *International Journal of Energy Research*. https://doi.org/10.1002/er.8595

Maduabuchi, C. C., Eke, M. N., & Mgbemene, C. A. (2021). Solar power generation using a two-stage X-leg thermoelectric generator with high-temperature materials. *International Journal of Energy Research*, *45*(9), 13163–13181. https://doi.org/10.1002/er.6644

Majumdar, A. (2004). Thermoelectricity in Semiconductor Nanostructures. *Science*, *303*(5659), 777–778. https://doi.org/10.1126/science.1093164

Manghwar, R., Selvaraj, J., Abd Rahim, N., Kumar, L., & Khoharo, H. (2024). Global advancements of solar thermoelectric generators application, limitations, and prospects: A comprehensive review. *Applied Thermal Engineering*, *257*, 124231. https://doi.org/10.1016/j.applthermaleng.2024.124231

Manivannan, S. P., Gunasekaran, D. L., Jaganathan, G., Natesan, S., Muthusamy, S. M., Kim, S. C., Kumar, B., Poongavanam, G. K., & Duraisamy, S. (2022). Energy and environmental analysis of a solar evacuated tube heat pipe integrated thermoelectric generator using IoT. *Environmental Science and Pollution Research*, *29*(38), 57835–57850. https://doi.org/10.1007/s11356-022-19857-w

Massetti, M., Jiao, F., Ferguson, A. J., Zhao, D., Wijeratne, K., Würger, A., Blackburn, J. L., Crispin, X., & Fabiano, S. (2021a). Unconventional Thermoelectric Materials for Energy Harvesting and Sensing Applications. In *Chemical Reviews* (Vol. 121, Issue 20, pp. 12465–12547). American Chemical Society. https://doi.org/10.1021/acs.chemrev.1c00218

Massetti, M., Jiao, F., Ferguson, A. J., Zhao, D., Wijeratne, K., Würger, A., Blackburn, J. L., Crispin, X., & Fabiano, S. (2021b). Unconventional Thermoelectric Materials for Energy Harvesting and Sensing Applications. *Chemical Reviews*, *121*(20), 12465–12547. https://doi.org/10.1021/acs.chemrev.1c00218

Menon, A. K., & Yee, S. K. (2015, November 13). Design of a High Performance Polymer Thermoelectric Generator Using Radial Architecture. *Volume 6A: Energy*. https://doi.org/10.1115/IMECE2015-51107

Miao, L., Zhu, S., Liu, C., Gao, J., Zhang, Z., Peng, Y., Chen, J.-L., Gao, Y., Liang, J., & Mori, T. (2024). Comfortable wearable thermoelectric generator with high output power. *Nature Communications*, *15*(1), 8516. https://doi.org/10.1038/s41467-024-52841-1

Moffat, R. J. (1988). *Describing the Uncertainties in Experimental Results*.

Montero, F. J., Lamba, R., Ortega, A., Jahn, W., Chen, W.-H., & Guzmán, A. M. (2023). A bidirectional solar thermoelectric generator combining heat storage for daytime and nighttime power generation. *Applied Thermal Engineering*, *224*, 119997. https://doi.org/https://doi.org/10.1016/j.applthermaleng.2023.119997

Niu, Z., Diao, H., Yu, S., Jiao, K., Du, Q., & Shu, G. (2014). Investigation and design optimization of exhaust-based thermoelectric generator system for internal combustion engine. *Energy Conversion and Management*, *85*, 85–101. https://doi.org/https://doi.org/10.1016/j.enconman.2014.05.061

Pal, A., Bandyopadhyay, D., Biswas, G., & Eswaran, V. (2012). Enhancement of Heat Transfer Using Delta-Winglet Type Vortex Generators with a Common-Flow-up Arrangement. *Numerical Heat Transfer, Part A: Applications*, *61*(12), 912–928. https://doi.org/10.1080/10407782.2012.677322

Peng, H., Guo, W., Feng, S., & Shen, Y. (2022). A novel thermoelectric energy harvester using gallium as phase change material for spacecraft power application. *Applied Energy*, *322*, 119548. https://doi.org/10.1016/j.apenergy.2022.119548

Qi, C., Du, Y., Chen, L., Yin, Y., & Ge, Y. (2023). Modeling and thermodynamic optimization of a solar-driven two-stage multi-element thermoelectric generator. *Journal of Cleaner Production*, *418*, 138147. https://doi.org/https://doi.org/10.1016/j.jclepro.2023.138147

Ramos-Castañeda, C. F., Olivares-Robles, M. A., & Méndez-Méndez, J. V. (2021). Analysis of the performance of a solar thermoelectric generator for variable leg geometry with nanofluid cooling. *Processes*, *9*(8). https://doi.org/10.3390/pr9081352

Ramzan, M., Shahmir, N., Ghazwani, H. A. S., Nisar, K. S., Alharbi, F. M., & Yahia, I. S. (2022). Hydrodynamic and heat transfer analysis of dissimilar shaped nanoparticles-based hybrid nanofluids in a rotating frame with convective boundary condition. *Scientific Reports*, *12*(1). https://doi.org/10.1038/s41598-021-04173-z

Rathi, V., Singh, K., Parmar, K. P. S., Brajpuriya, R. K., & Kumar, A. (2024). Improved thermoelectric performance of PEDOT:PSS/Bi $_2$ Te $_3$ /reduced graphene oxide ternary composite films for energy harvesting applications. *RSC Advances*, *14*(47), 34883–34892. https://doi.org/10.1039/D4RA06184E

Sahoo, R. R., & Karana, D. R. (2020). Effect of design shape factor on exergonic performance of a new modified extended-tapering segmented thermoelectric generator system. *Energy*, *200*. https://doi.org/10.1016/j.energy.2020.117561

Samadifar, M., & Toghraie, D. (2018). Numerical simulation of heat transfer enhancement in a plate-fin heat exchanger using a new type of vortex generators. *Applied Thermal Engineering*, *133*, 671–681. https://doi.org/https://doi.org/10.1016/j.applthermaleng.2018.01.062

Sameer Mahmoud, N., Mohammad Jaffal, H., & Abdulnabi Imran, A. (2021a). Performance evaluation of serpentine and multi-channel heat sinks based on energy and exergy analyses. *Applied Thermal Engineering*, *186*, 116475. https://doi.org/https://doi.org/10.1016/j.applthermaleng.2020.116475

Sameer Mahmoud, N., Mohammad Jaffal, H., & Abdulnabi Imran, A. (2021b). Performance evaluation of serpentine and multi-channel heat sinks based on energy and exergy analyses. *Applied Thermal Engineering*, *186*. https://doi.org/10.1016/j.applthermaleng.2020.116475

Selimefendigil, F., Okulu, D., & Mamur, H. (2021). Numerical analysis for performance enhancement of thermoelectric generator modules by using CNT–water and hybrid Ag/MgO–water nanofluids. *Journal of Thermal Analysis and Calorimetry*, *143*(2), 1611–1621. https://doi.org/10.1007/s10973-020-09983-3

Shamsuddin, H. S., Estellé, P., Navas, J., Mohd-Ghazali, N., & Mohamad, M. (2021). Effects of surfactant and nanofluid on the performance and optimization of a microchannel heat sink. *International Journal of Heat and Mass Transfer*, *175*. https://doi.org/10.1016/j.ijheatmasstransfer.2021.121336

Sharma, A., Masoumi, S., Gedefaw, D., O'Shaughnessy, S., Baran, D., & Pakdel, A. (2022). Flexible solar and thermal energy conversion devices: Organic photovoltaics (OPVs), organic thermoelectric generators (OTEGs) and hybrid PV-TEG systems. *Applied Materials Today*, *29*, 101614. https://doi.org/10.1016/j.apmt.2022.101614

Shen, Z.-G., Wu, S.-Y., Xiao, L., & Yin, G. (2016). Theoretical modeling of thermoelectric generator with particular emphasis on the effect of side surface heat transfer. *Energy*, *95*, 367–379. https://doi.org/https://doi.org/10.1016/j.energy.2015.12.005

Sudarsana Reddy, P., & Chamkha, A. J. (2016). Influence of size, shape, type of nanoparticles, type and temperature of the base fluid on natural convection MHD of nanofluids. *Alexandria Engineering Journal*, *55*(1), 331–341. https://doi.org/https://doi.org/10.1016/j.aej.2016.01.027

Sun, H., Ge, Y., Liu, W., & Liu, Z. (2019). Geometric optimization of two-stage thermoelectric generator using genetic algorithms and thermodynamic analysis. *Energy*, *171*, 37–48. https://doi.org/https://doi.org/10.1016/j.energy.2019.01.003

Sun, X., Liang, X., Shu, G., Tian, H., Wei, H., & Wang, X. (2014). Comparison of the two-stage and traditional single-stage thermoelectric generator in recovering the

waste heat of the high temperature exhaust gas of internal combustion engine. *Energy*, *77*, 489–498. https://doi.org/10.1016/j.energy.2014.09.032

Sun, Y., Qiu, L., Tang, L., Geng, H., Wang, H., Zhang, F., Huang, D., Xu, W., Yue, P., Guan, Y., Jiao, F., Sun, Y., Tang, D., Di, C., Yi, Y., & Zhu, D. (2016a). Flexible n-Type High-Performance Thermoelectric Thin Films of Poly(nickel-ethylenetetrathiolate) Prepared by an Electrochemical Method. *Advanced Materials*, *28*(17), 3351–3358. https://doi.org/10.1002/adma.201505922

Sun, Y., Qiu, L., Tang, L., Geng, H., Wang, H., Zhang, F., Huang, D., Xu, W., Yue, P., Guan, Y., Jiao, F., Sun, Y., Tang, D., Di, C., Yi, Y., & Zhu, D. (2016b). Flexible n-Type High-Performance Thermoelectric Thin Films of Poly(nickel-ethylenetetrathiolate) Prepared by an Electrochemical Method. *Advanced Materials*, *28*(17), 3351–3358. https://doi.org/10.1002/adma.201505922

Sun, Y., Sheng, P., Di, C., Jiao, F., Xu, W., Qiu, D., & Zhu, D. (2012). Organic Thermoelectric Materials and Devices Based on *p* - and *n* -Type Poly(metal 1,1,2,2-ethenetetrathiolate)s. *Advanced Materials*, *24*(7), 932–937. https://doi.org/10.1002/adma.201104305

Tian, M.-W., Khorasani, S., Moria, H., Pourhedayat, S., & Dizaji, H. S. (2020). Profit and efficiency boost of triangular vortex-generators by novel techniques. *International Journal of Heat and Mass Transfer*, *156*, 119842. https://doi.org/10.1016/j.ijheatmasstransfer.2020.119842

Tuckerman, D. B., & Pease, R. F. W. (1981). High-Performance Heat Sinking for VLSI. In *IEEE ELECTRON DEVICE LETTERS* (Issue 5).

Venkatasubramanian, R., Siivola, E., Colpitts, T., & O'Quinn, B. (2001). Thin-film thermoelectric devices with high room-temperature figures of merit. *Nature*, *413*(6856), 597–602. https://doi.org/10.1038/35098012

Wang, L., Zhang, Z., Liu, Y., Wang, B., Fang, L., Qiu, J., Zhang, K., & Wang, S. (2018). Exceptional thermoelectric properties of flexible organic−inorganic hybrids with monodispersed and periodic nanophase. *Nature Communications*, *9*(1), 3817. https://doi.org/10.1038/s41467-018-06251-9

Wang, Y., Li, S., Zhang, Y., Yang, X., Deng, Y., & Su, C. (2016). The influence of inner topology of exhaust heat exchanger and thermoelectric module distribution on the performance of automotive thermoelectric generator. *Energy Conversion and Management*, *126*, 266–277. https://doi.org/10.1016/j.enconman.2016.08.009

Wilcox, D. C. (1998). *Turbulence Modeling for CFD* (Vol. 2). CA: DCW industries.

Wu, X., Fu, T., Wang, J., Zeng, L., & Zhang, F. (2024). A comparative study of fluid flow and heat transfer in the tube with multi-V-winglets vortex generators. *Applied Thermal Engineering*, *236*, 121448. https://doi.org/https://doi.org/10.1016/j.applthermaleng.2023.121448

Xia, B., Shi, X.-L., Zhang, L., Luo, J., Chen, W.-Y., Hu, B., Cao, T., Wu, T., Liu, W.-D., Yang, Y., Liu, Q., & Chen, Z.-G. (2024). Vertically designed high-performance and flexible thermoelectric generator based on optimized PEDOT:PSS/SWCNTs

composite films. *Chemical Engineering Journal*, *486*, 150305. https://doi.org/https://doi.org/10.1016/j.cej.2024.150305

Xie, C., Yan, G., Ma, Q., Elmasry, Y., Singh, P. K., Algelany, A. M., & Wae-hayee, M. (2022). Flow and heat transfer optimization of a fin-tube heat exchanger with vortex generators using Response Surface Methodology and Artificial Neural Network. *Case Studies in Thermal Engineering*, *39*, 102445. https://doi.org/10.1016/j.csite.2022.102445

Xie, H., Gao, T., Long, X., Sun, L., Wang, J., Xia, E., Li, S., Li, B., Li, C., Gao, M., & Mo, Z. (2023). Design and performance of a modular 1 kilowatt-level thermoelectric generator for geothermal application at medium-low temperature. *Energy Conversion and Management*, *298*, 117782. https://doi.org/10.1016/j.enconman.2023.117782

Yahyaee, A. (2024). Influence of nanoparticle shapes in nanofluid film boiling on vertical cylinders: A numerical study. *International Journal of Thermofluids*, *22*, 100631. https://doi.org/https://doi.org/10.1016/j.ijft.2024.100631

Yang, W., Jin, C., Zhu, W., Xie, C., Huang, L., Li, Y., & Xiong, B. (2024). Innovative design for thermoelectric power generation: Two-stage thermoelectric generator with variable twist ratio twisted tapes optimizing maximum output. *Applied Energy*, *363*, 123047. https://doi.org/https://doi.org/10.1016/j.apenergy.2024.123047

Yang, X. H., Tan, S. C., Ding, Y. J., & Liu, J. (2017). Flow and thermal modeling and optimization of micro/mini-channel heat sink. *Applied Thermal Engineering*, *117*, 289–296. https://doi.org/10.1016/j.applthermaleng.2016.12.089

Yin, L. C., Liu, W. Di, Shi, X. L., Gao, H., Li, M., Wang, D. Z., Wu, H., Kou, L., Guo, H., Wang, Y., Liu, Q., & Chen, Z. G. (2022). High near-room temperature figure of merit of n-type Bi2GeTe4-based thermoelectric materials via a stepwise optimization of carrier concentration. *Chemical Engineering Journal*, *433*. https://doi.org/10.1016/j.cej.2021.133775

Yin, T., Li, W. T., Li, K., & He, Z. Z. (2021). Multi-parameter optimization and uncertainty analysis of multi-stage thermoelectric generator with temperature-dependent materials. *Energy Reports*, *7*, 7212–7223. https://doi.org/10.1016/j.egyr.2021.10.079

Zeng, M., Tang, L. H., Lin, M., & Wang, Q. W. (2010). Optimization of heat exchangers with vortex-generator fin by Taguchi method. *Applied Thermal Engineering*, *30*(13), 1775–1783. https://doi.org/10.1016/j.applthermaleng.2010.04.009

Zhang, A. B., Wang, B. L., Pang, D. D., Chen, J. B., Wang, J., & Du, J. K. (2018). Influence of leg geometry configuration and contact resistance on the performance of annular thermoelectric generators. *Energy Conversion and Management*, *166*, 337–342. https://doi.org/https://doi.org/10.1016/j.enconman.2018.04.042

Zhang, J.-F., Jia, L., Yang, W.-W., Taler, J., & Oclon, P. (2019). Numerical analysis and parametric optimization on flow and heat transfer of a microchannel with

longitudinal vortex generators. *International Journal of Thermal Sciences*, *141*, 211–221. https://doi.org/10.1016/j.ijthermalsci.2019.03.036

Zhang, K., Sun, Z., Zheng, N., & Chen, Q. (2020). Effects of the configuration of winglet vortex generators on turbulent heat transfer enhancement in circular tubes. *International Journal of Heat and Mass Transfer*, *157*, 119928. https://doi.org/https://doi.org/10.1016/j.ijheatmasstransfer.2020.119928

Zhang, M., Miao, L., Kang, Y. P., Tanemura, S., Fisher, C. A. J., Xu, G., Li, C. X., & Fan, G. Z. (2013). Efficient, low-cost solar thermoelectric cogenerators comprising evacuated tubular solar collectors and thermoelectric modules. *Applied Energy*, *109*, 51–59. https://doi.org/https://doi.org/10.1016/j.apenergy.2013.03.008

Zhang, Y., Liu, H., Zhou, X., Hu, Z., Wang, H., Kuang, M., Li, J., & Zhang, H. (2024). A novel photo-thermal-electric hybrid system comprising evacuated U-tube solar collector and inhomogeneous thermoelectric generator toward efficient and stable operation. *Energy*, *292*, 130616. https://doi.org/https://doi.org/10.1016/j.energy.2024.130616

Zhao, L.-D., He, J., Berardan, D., Lin, Y., Li, J.-F., Nan, C.-W., & Dragoe, N. (2014). BiCuSeO oxyselenides: new promising thermoelectric materials. *Energy Environ. Sci.*, *7*(9), 2900–2924. https://doi.org/10.1039/C4EE00997E

Zhao, Q., Zhang, H., Hu, Z., & Hou, S. (2020). Achieving a broad-spectrum photovoltaic system by hybridizing a two-stage thermoelectric generator. *Energy Conversion and Management*, *211*, 112778. https://doi.org/https://doi.org/10.1016/j.enconman.2020.112778

LIST OF PUBLICATIONS

Journals

1. Srivastava K, Sahoo RR. Taguchi and ANN model optimization for uni-array vortex generator incorporated rectangular channel for high thermo-hydraulic performance. International Journal of Thermal Sciences. 2025;210:109634. https://doi.org/10.1016/j.ijthermalsci.2024.109634.
2. Srivastava K, Sahoo RR. Experimental and numerical study on thermal performance of new envelope and triangular vortex generators with different pitch and angle of attack. Thermal Science and Engineering Progress. 2024;49:102459. https://doi.org/10.1016/j.tsep.2024.102459
3. Srivastava K, Sahoo RR. Impact of a new envelope winglet vortex generator on engine power and thermoelectric waste heat recovery. Journal of Thermal Analysis and Calorimetry. 2023;148(24):14319-36. https://doi.org/10.1007/s10973-023-12582-7.
4. Srivastava K, Sahoo RR. Effect of pitch and angle of attack on thermal performance of new envelope and delta vortex generators for TEG: An experimental and numerical approach. International Journal of Thermal Sciences. 2024;195:108671. https://doi.org/10.1016/j.ijthermalsci.2023.108671.
5. Sahoo, RR, Srivastava K. Thermo-hydraulic effect of a convergent-divergent cold channel using MXene nanofluid for thermoelectric-based waste heat recovery system. Heat and Mass Transfer. 2023;59, 2117–2129. https://doi.org/10.1007/s00231-023-03382-8.
6. Srivastava K, Sahoo RR. 2E's (energy and exergy) analysis of a multi-stage variable leg-shaped TEG with CNT and graphene-based MXene ternary hybrid nanofluids as new coolant. Journal of Thermal Analysis and Calorimetry. 2023;148(24):14305-18. https://doi.org/10.1007/s10973-023-12614-2.
7. Srivastava K, Sahoo RR. Experimental study on thermo-hydraulic performance of a novel envelope winglet vortex generator in a TEG hot-side engine exhaust heat exchanger. Journal of Thermal Analysis and Calorimetry. 2023;148(18):9723-37. https://doi.org/10.1007/s10973-023-12325-8.
8. Srivastava K, Sahoo RR. Effects of Performance and Normalized Parameters on various materials based Multistage Thermoelectric Generator. Journal of Thermal Science and Engineering Applications. 2023:1-21. https://doi.org/10.1115/1.4062999.
9. Srivastava K, Sahoo RR. Thermal, exergetic, and performance analysis of dissimilar-shaped nanoparticles hybrid nanofluid for flow across minichannel heat sink. Journal of Thermal Analysis and Calorimetry. 2023;148(14):7501-18. https://doi.org/10.1007/s10973-023-12191-4.

Conferences

1. Thermoelectric Generators for Waste Heat Utilization: Means to reduce Fossil Fuel Consumption and Produce Electricity, VII International Conference on "Sustainable Energy and Environmental Challenges" (VII SEEC).
2. Preparation, Characterization, and Hydrothermal Performance of Carbon Quantum Dots-based Nanofluid for Coolant Application, 9th National and 30th All India Manufacturing Technology, Design and Research Conference.
3. Performance enhancement of Thermoelectric Generator using Dissimilar Material employing multistage configuration, 27th National and 5th International ISHMT-ASTFE Heat and Mass Transfer Conference.